Effect of Material Properties on Light-Induced Degradation of Amorphous Silicon Solar Cells

May 1993

Masao ISOMURA

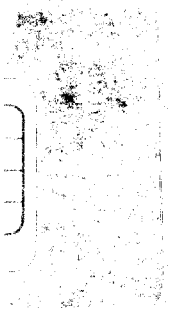

Effect of Material Properties on Light-Induced Degradation of Amorphous Silicon Solar Cells

May 1993

Masao ISOMURA

Abstract

Light-induced degradation is a serious obstacle to high efficiency in hydrogenated amorphous silicon (a-Si:H) solar cells, and this problem must be solved in order to apply them to large-scale energy sources. A solution to the problem is sought by investigating light-induced degradation from the viewpoint of its effects on materials, and by considering the relation between material effects and device degradation.

The light-induced effect of the i-layer is studied with respect to the origin of the light-induced defects. The light-induced defect density in a-Si:H can be brought to saturation with only a few hours of intense illumination. The saturation value is correlated with the growth rate of the defect density and can be a robust criterion for predicting the "usable life" of a-Si:H materials and of solar cells. The behavior of the saturation value can be explained within the defect pool model by the limited number of defect sites in the tail states coupled with the concept of defect equilibrium. The saturation value is not correlated with the characteristic energy of the Urbach slope. The hydrogen content is more important for limiting the number of defects than the tail states.

The light-induced effect of the window p-layer is studied focusing on the degradation of the open-circuit voltage. Significant degradation in V_{oc} occurs with low-doped p-layers. The light-induced defects in the low-doped p-layer are not negligible compared with the initial defects in the low-doped p-layer and thus more carrier recombination occurs. Besides, some of the acceptors are compensated by the light-induced defects. On the other hand, the high-doped p-layer does not cause much V_{oc} degradation because the light-induced defects are negligible compared with the large number of doping-induced defects and acceptors. The midgap defects induced by doping or light-soaking near the p/i interface cause the V_{oc} limitation.

The kinetic processes of the light-induced defects are also investigated. The rate of light-induced defect creation shows larger temperature dependence under higher intensity light. This increased temperature dependence suggests that a temperature-activated process controls the rates of creation more when the defect creation rate is high, and can be explained by the carrier-driven

process coupled with hydrogen motion. The rate of annealing under illumination is accelerated by illumination, and depends on the light intensity. This behavior of light-induced annealing can be explained by the diffusion of hydrogen, enhanced by illumination.

The SiH_2 configuration is newly taken into account in a model based on the hydrogen-motion model. A bond-breaking process followed by hydrogen motion is assumed. The hydrogen motion is accompanied by structural relaxation, which stabilizes the dangling bond states, due to the two-fold SiH_2 configuration. The phenomena observed in this thesis can be illustrated with the new model.

Contents

1 Introduction

1.1 Progress in the research of amorphous silicon solar cells

Before hydrogenated amorphous silicon (a-Si:H) was reported, amorphous silicon without hydrogen prepared by sputtering or thermal evaporation was investigated. The unhydrogenated material has a high defect density which prevents to have desirable characteristics of a useful semiconductor. A-Si:H was first reported in the UK in 1969, using a glow discharge with silane gas (SiH_4) [1]. It was confirmed that a-Si:H has good electrical properties with a high carrier mobility [2] and high photosensitivity with a low defect density [3] compared with the unhydrogenated material. The essential role of the hydrogen in a-Si:H was recognized in 1974 by incorporating hydrogen into the sputtered materials [4]. The incorporated hydrogen eliminates the defects in the sputtered materials and improves the properties, as seen in glow discharge a-Si:H. After this report it was shortly confirmed that the glow discharge materials also contain hydrogen [5]. The significant progress in the development of a-Si:H technologies was made in 1975 by Spear and LeComber. They first succeeded in the substitutional p-type or n-type doping of a-Si:H by adding diborane (B_2H_6) or phosphine (PH_3), respectively, to the deposition gas [6]. Since these reports, a-Si:H has received considerable attention as an electronic material and has been investigated intensively in several laboratories.

The device research of a-Si:H was started by Carlson and Wronski in 1976 at RCA Laboratories with the development of pin photovoltaic devices [7]. The initial conversion efficiency of their a-Si:H solar cells was 2-3%. In 1980 SANYO put the first a-Si:H solar cells onto the market as a power source for hand-held calculators [8]. The integrated-type a-Si:H solar cell structure gave us high output voltage [9]. In addition, the spectral response of a-Si:H solar cells is well suited to fluorescent light, so these calculators work well in an office environment. The a-Si:H solar cells offer a great advantage as a low-cost energy source compared with crystalline materials, due to the following features.

(1) Less energy is required in the fabrication process.

(2) The fabrication process is more simple.

(3) Much larger sizes can be produced.

(4) The amount of materials required for solar cells is much less.

(5) Structural flexibility widens the range of application.

Subsequent research has enabled development of several technologies, such as an a-SiC:H window layer [10], a reduction in incorporated impurities [11], and a laser patterning method [12] as shown in Fig. 1-1. The conversion efficiency has also been improved year by year, and has now reached 12% for the size of 100 cm^2 [13]. Further improvement in this efficiency can be expected in the future by adopting a multi-bandgap structure and other technologies.

1.2 Light-induced degradation of amorphous silicon solar cells

In 1977, Staebler and Wronski discovered a light-induced metastable effect in the dark conductivity and photoconductivity of a-Si:H, commonly called the Staebler-Wronski (S-W) effect [14]. Both conductivities decrease after the illumination of band-gap light and recover their original values by subsequent thermal annealing at around 150°C. After light-soaking, the increase in subgap absorption can be observed by optical absorption measurements such as the photothermal deflection spectroscopy (PDS) [15] or the constant photocurrent method (CPM) [16], and the electron spin resonance (ESR) measurement also shows that the neutral dangling bond density increases with prolonged light-soaking [17]. Therefore, the increase in the defect states of Si-dangling bonds in the midgap is directly related to the S-W effect. These defects create a recombination center for excess carriers and shorten the lifetime of photogenerated carriers. Hence, the material quality for electronic devices is adversely influenced. The excess carriers are thought to play a more important role than the light itself in creating the light-induced effect because carrier injection to a-Si:H films also creates similar defects [18]. It is well established that the recombination or trapping of the excess carriers creates the defects. Nonradiative tail-to-tail recombination of the photoinduced carriers is assumed to be a defect-creation step in a model

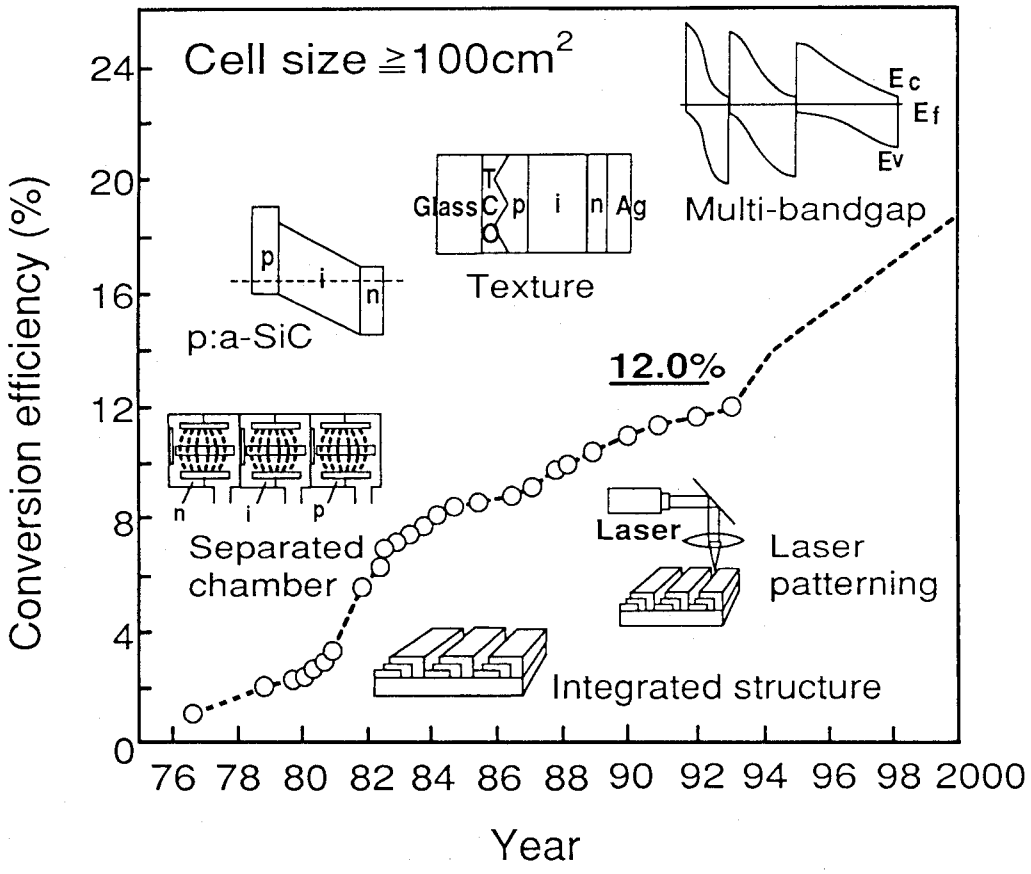

Figure 1-1 Progress in conversion efficiency of amorphous silicon solar cells.

proposed by Stutzmann et al. [19], which is widely accepted. It is, however, not clear which mechanism is the dominant driving force.

The light-induced effect of the material is a serious obstacle to high efficiency in a-Si:H solar cells, and this problem must be solved in order to apply them to a large scale energy source. Figure 1-2 shows an example of the typical degradation properties of a-Si:H solar cells in long-term operation [20]. In particular, the fill factor (FF) is reduced more than the other parameters of V_{oc} and I_{sc}. This is a main cause of the efficiency degradation, and the efficiency drops about 20% after long-term operation (~3 years). The midgap defects caused by light-soaking in the intrinsic layer (i-layer) prevent the transport of photogenerated carriers. As shown in Fig. 1-3, the electric field in the intrinsic layer is uniformly spread with the built-in potential in the pin junction at the initial state, and most photogenerated electrons and holes are immediately separated to the n and p-layers, respectively. After light-soaking, however, the electric field in the middle of the i-layer is weakened by the charged defects near the p/i and i/n interfaces [21]. In this region, photogenerated carriers do not move quickly, and some of them recombine through the defects. This is the reason why the FF decreases after light-soaking.

1.3 Purpose of the present study

In this thesis, a solution to this problem is sought by investigating the light-induced degradation from the viewpoint of its effects on materials, and by considering the relation between the material effects and the device degradation.

A block diagram of the organization is illustrated in Fig. 1-4. In Chapter 2 the light-induced effect of the i-layer is studied with respect to the origin of the light-induced defects, in Chapter 3 the light-induced effect of the window p-layer is studied focusing on the degradation of the open-circuit voltage, and more details on the kinetics of the light-induced defects and the change in the microscopic structure are discussed in Chapter 4. The results are summarized in Chapter 5.

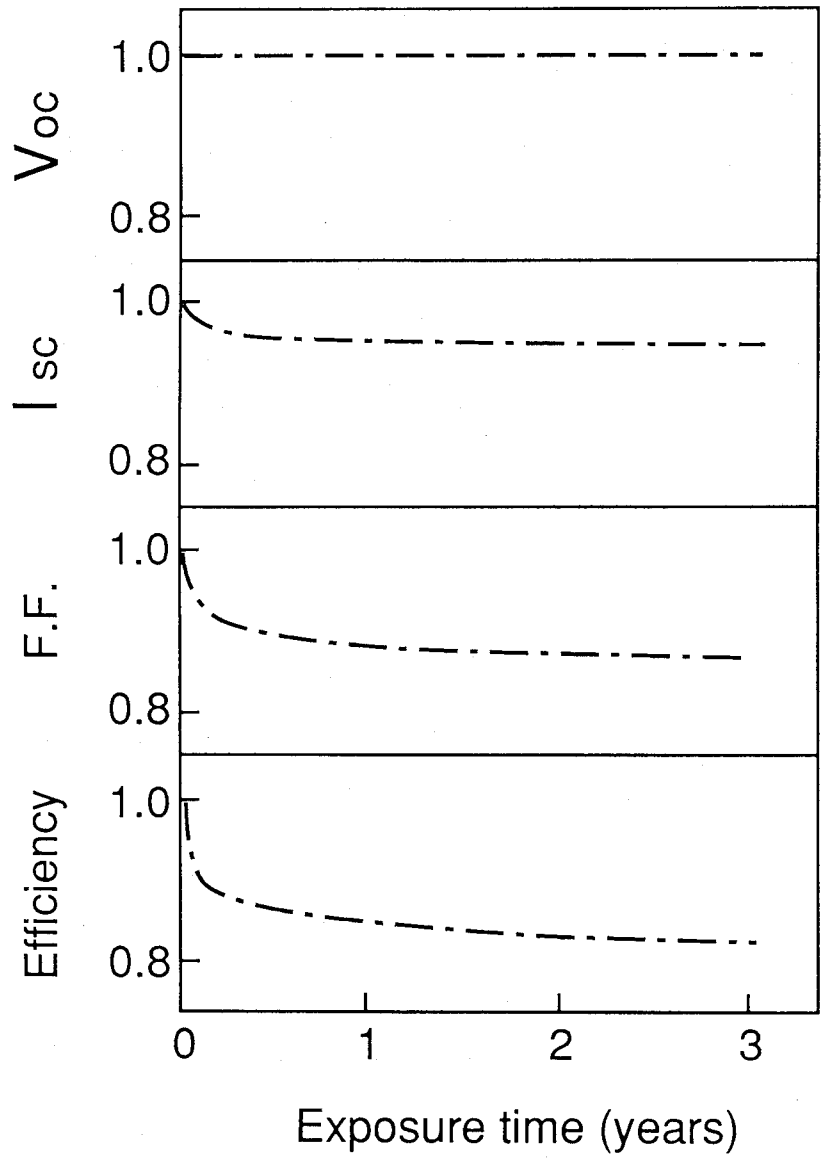

Figure 1-2 Long-term light-induced degradation of typical amorphous silicon solar cells.

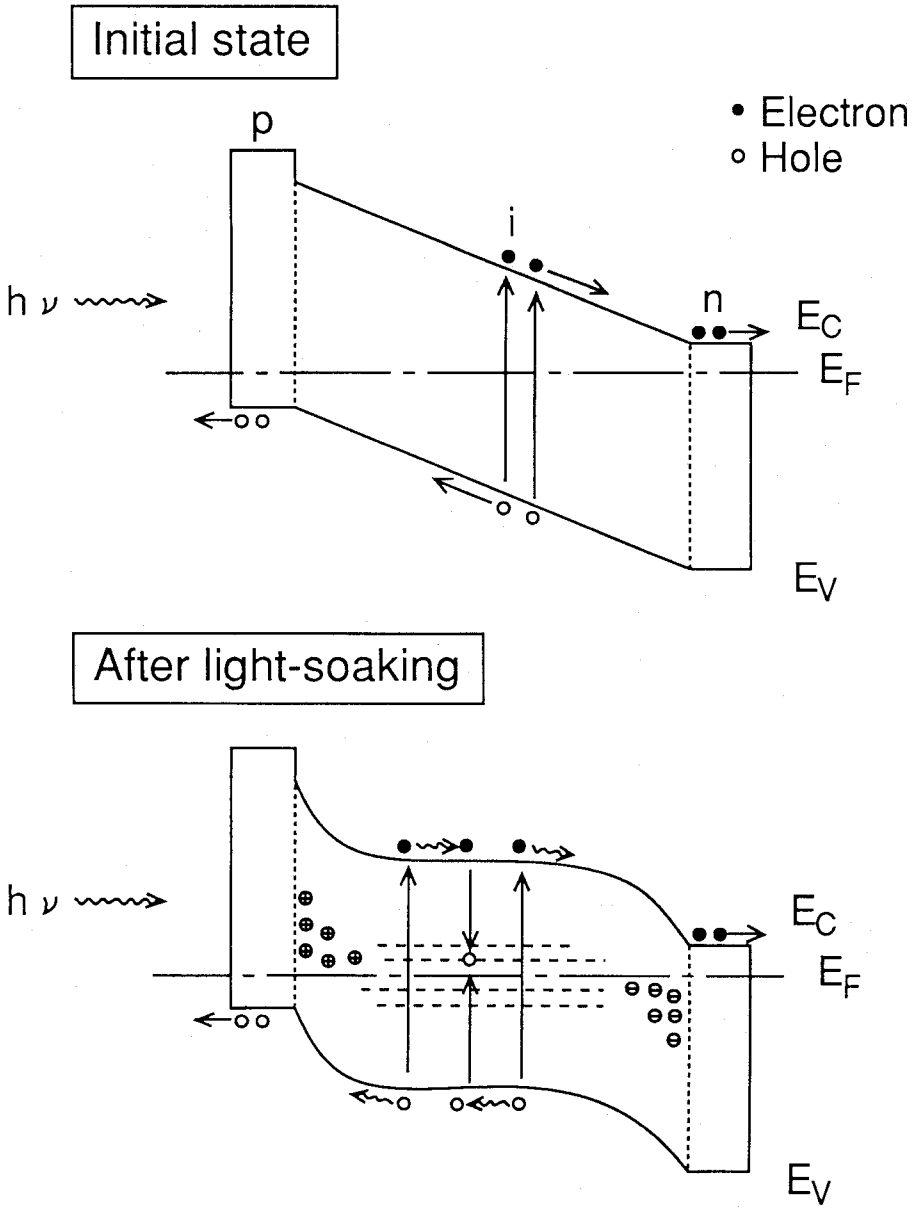

Figure 1-3 Band-profiles of amorphous silicon solar cells at initial condition and after light-soaking.

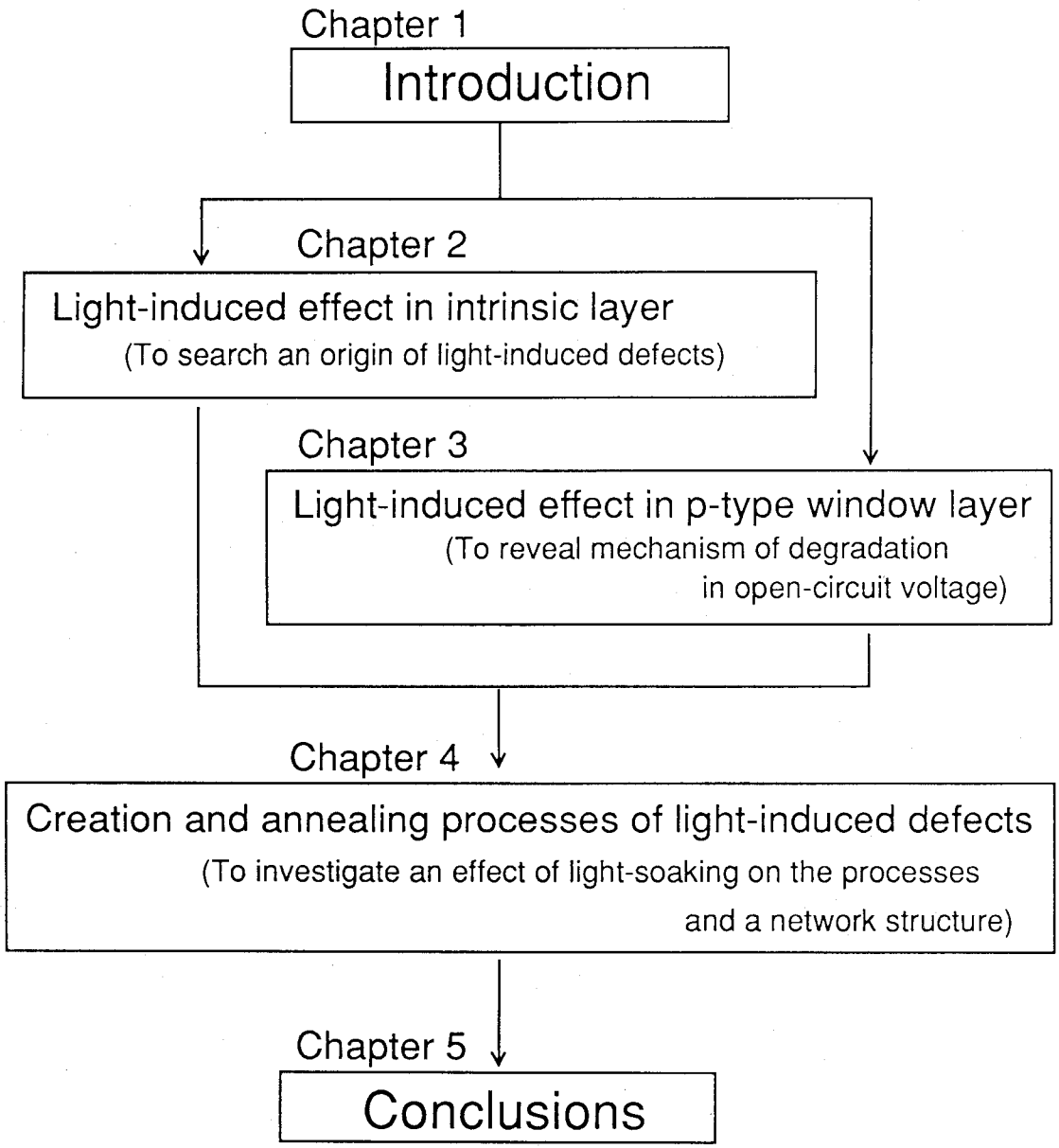

Fugure 1-4 Block diagram of the organization of this thesis.

References

1. R.C. Chittick, J.H. Alexander and H.F. Sterling: J. Electrochemical Soc. **116** (1969) 77.
2. P.G. LeComber and W.E. Spear: Phys. Rev. Lett. **25** (1970) 509.
3. W.E. Spear, R.J. Loveland and A. Al-Sharbaty: J. Non-Cryst. Solids **15** (1974) 410.
4. A.J. Lewis, G.A.N. Connell, W. Paul, J. Pawlik and R. Temkin: AIP Conf. Proc. **20** (1974) 27.
5. H. Fritzsche: *Proc. 7th Int. Conf. on Amorphous and Liquid Semiconductors*, (CICL, Edinborgh, 1977), p.3.
6. W.E. Spear and P.G. LeComber: Solid State Commun. **17** (1975) 1193.
7. D.E. Carlson and C.R. Wronski: Appl. Phys. Lett. **28** (1976) 671.
8. Y. Kuwano and M. Ohnishi: *Proc. 19th Int. Conf. on Amorphous and Liquid Semiconductors*, (Les Editions de Physique, Paris, 1981) p1151.
9. Y. Kuwano, S. Tsuda, M. Ohnishi, H. Nishiwaki, H. Shibuya, S. Nakano and T. Imai: Jpn. J. Appl. Phys. **20**, Suppl. 20-2 (1981) 213.
10. Y. Tawada, M. Kondo, H. Okamoto and Y. Hamakawa: Sol. Energy Mater. **6** (1982) 299.
11. S. Tsuda, T. Takahama, M. Isomura, H. Tarui, Y. Nakashima, Y. Hishikawa, N. Nakamura, T. Matsuoka, H. Nishiwaki, S. Nakano, M. Ohnishi and Y. Kuwano: Jpn. J. Appl. Phys. **26** (1987) 33.
12. S. Nakano, T. Matsuoka, S. Kiyama, H. Kawata, N. Nakamura, Y. Nakashima, S. Tsuda, H. Nishiwaki, M. Ohnishi, I. Nagaoka and K. Kuwano: Jpn. J. Appl. Phys. **25** (1986) 1936.
13. Y. Hishikawa, M. Sasaki, S. Tsuge, S. Okamoto and S. Tsuda: *Proc. Material Research Society 1993 Spring Meeting*, to be published.
14. D.L. Staebler and C.R. Wronski: Appl. Phys. Lett. **31** (1977) 292.
15. 15. W.B. Jackson, N.M. Amer, A.V. Boccara and D. Fournier: Appl. Opt. **38** (1981) 1333.
16. M. Vanecek, J. Kocka, J. Stuchlik, Z. Kosicek, O. Stika and A. Triska: Sol. Energy Mater. **8** (1983) 411.
17. H. Dersch, J. Stuke and J. Beichler: Appl. Phys. Lett. **38** (1980) 456.

18. W. Kruhler, H. Pfleiderer, R. Plattner and W. Stetter: *AIP Conf. Proc.* **120** (1984) 311.

19. M. Stutzmann, W.B. Jackson and C.C. Tsai: Phys. Rev. B **32** (1985) 23.

20. S. Tsuda, N. Nakamura, K. Watanabe, M. Nishikuni, M. Ohnishi, S. Nakano, Y. Kishi, H. Shibuya and Y. Kuwano: *Tech. Dig. 1st International PVSEC*, Kobe, Japan, 1984, p.213.

21. S. Yamanaka, M. Konagai and K. Takahashi: Jpn. J. Appl. Phys. **28** (1989) 1178.

2 Light-induced degradation of the intrinsic layer

2.1 Background and motivation

The light-induced degradation in the intrinsic layer is a serious obstacle to high efficiency in a-Si:H solar cells because an increasing density of defects in the intrinsic layer causes the fill factor to decrease [1]. This is the most important cause of degradation. Much attention has been drawn to this effect and many researchers are working on this phenomenon, but we have neither a clear understanding of its mechanism nor an unequivocal method for its evaluation. Therefore, it is quite important to acquire precise quantitative information about the effect. However, the rate of build-up of the defect density depends very much on the conditions of the light-soaking, which makes precise kinetic data difficult to obtain. Furthermore, the defect density grows slowly under solar illumination, which makes obtaining information about stability a time consuming task. The time for producing defects can be shortened by raising the light intensity. This approach has been taken by several groups for both materials and devices [2-7]. A new method for reaching saturation of the light-induced defect density (N_{sat}) is introduced here. N_{sat} can be obtained in typical a-Si:H within a few hours by soaking with extremely high-intensity light. As a consequence of saturation the measured defect density (N_{sat}) becomes independent of spatial or temporal variations of the light intensity. Therefore, N_{sat} is possibly a criterion for the stability of a-Si:H that is more reliable than measurements of the degradation process which are taken before saturation is reached. This Chapter focuses on N_{sat} to reveal the origin of the light-induced defects and to evaluate the stability of the intrinsic material. The experimental techniques and characteristics of the saturated light-induced defect density are described in Section 2.2, the mechanism and origin of the saturation are discussed in Section 2.3, and the life time of solar cells is predicted with the saturated light-induced defect density in Section 2.4.

2.2 Saturated light-induced defect density

2.2.1 Experimental techniques

The samples were deposited from silane gas on Corning 7059 glass or quartz substrates from a DC excited glow discharge (GD) or from a RF (13.56 MHz or 70 MHz) excited GD. One group was made by reactive sputtering in a DC magnetron sputtering system. The special features of some samples included the use of fluorinated source gases or an ultra-high vacuum system [8]. Details are given in Table 2-1. The defect density (N_S) was measured with the constant photocurrent method (CPM) [9] by converting the integrated subgap absorption intensity to N_S using the calibration factor of 1.9×10^{16} $cm^{-2} \cdot eV^{-1}$ between CPM and ESR measurements [10]. When a series of experiments was done on the same sample, *relative* values of N_S were determined by overlaying the CPM spectra. The accuracy of such relative N_S-data is estimated to be $\log(N_S) \pm 0.05$, or $N_S \pm 15\%$. The scatter in the absolute values of N_S, as used for comparing results from different samples, is $N_S \pm 30\%$ if the same operator evaluates the CPM spectra [11,12].

Table 2-1 Deposition conditions and properties of the samples.

Deposition technique	Source gases	T_{sub}[b] (°C)	c_H[c] (at.%)	d[d] (μm)
DC triode GD[a]	SiF_4+H_2	200-300	8-18	1.0-2.0
DC triode GD	SiH_4	300	<10	1.2-2.0
RF GD (13.6MHz)	SiH_4	100-350	7-16	1.9-4.5
UHV RF GD (13.6MHz)	SiH_4	160-300	11-22	0.5-1.7
RF GD (70MHz)	SiH_4	100-250	10-18	1.7-2.9
DC magnetron reactive sputtering	x-Si,Ar,H_2	200-300	11-31	0.8-2.0

(a) Fluorine content 0.1-8 atomic percent from IR absorption between 830 and 1015 cm^{-1}.
(b) Substrate temperature.
(c) Hydrogen content from IR absorption at 630 cm^{-1}.
(d) Thickness.

The hydrogen content was evaluated by integrating the wagging mode of the IR absorption [13]. The photoconductivity was measured with bandpass-filtered light from a tungsten-halogen lamp (λ=650±20 nm) at G=5x10^{19} $cm^{-3}s^{-1}$. The samples for the temperature-dependence measurement of N_{sat} were deposited on thin quartz substrates whose thickness was 0.3 mm. This allowed better control of the temperature due to the high thermal conductance of this substrate.

For light-soaking, the samples were mounted in one of two different configurations, which are shown in Fig. 2-1, and illuminated with light produced by spreading a Kr-ion laser beam of wavelength 647.1 nm. Most experiments were done on free-standing samples whose edges were clamped in a holder (Fig. 2-1 (a)). The samples were cooled from the back side with a flow of nitrogen (N_2) gas which had been passed through liquid N_2, thus keeping the temperature of the samples below 35°C during Kr^+ laser soaking. The sample temperature was determined by the calibrated transmittance of a low intensity He-Ne laser beam (λ=632.8nm). When it was necessary to control the sample temperature, the samples were mounted on a thermoelectric element whose reference-temperature side was attached to a fan-cooled aluminum heat sink, as shown in Fig. 2-1 (b). The sample temperature was monitored by the calibrated reflectance of a low intensity He-Ne laser beam from the surface of the a-Si:H films during Kr^+ laser soaking. The reflection of the He-Ne laser beam was measured with and without illumination from the Kr-ion laser at several temperature settings of the thermoelectric element. Figure 2-2 shows the reflectance of the sample with and without illumination from the Kr-ion laser as a function of the temperature of the thermoelectric element. The U-shaped reflectance plot is shifted to the left by Kr-ion laser illumination, and this shift reflects the raising of the sample temperature by the laser power. The temperature of the a-Si:H film is estimated to rise by 10°C to 15°C above that set by the thermoelectric element.

2.2.2 *Saturation of the light-induced defects*

The results of light-soaking experiments on two samples prepared by a RF excited GD are shown in Fig. 2-3. In long term light-soaking experiments under the low-intensity condition, the carrier generation rate (G) is 5x10^{20} $cm^{-3}s^{-1}$, and the defect density begins to

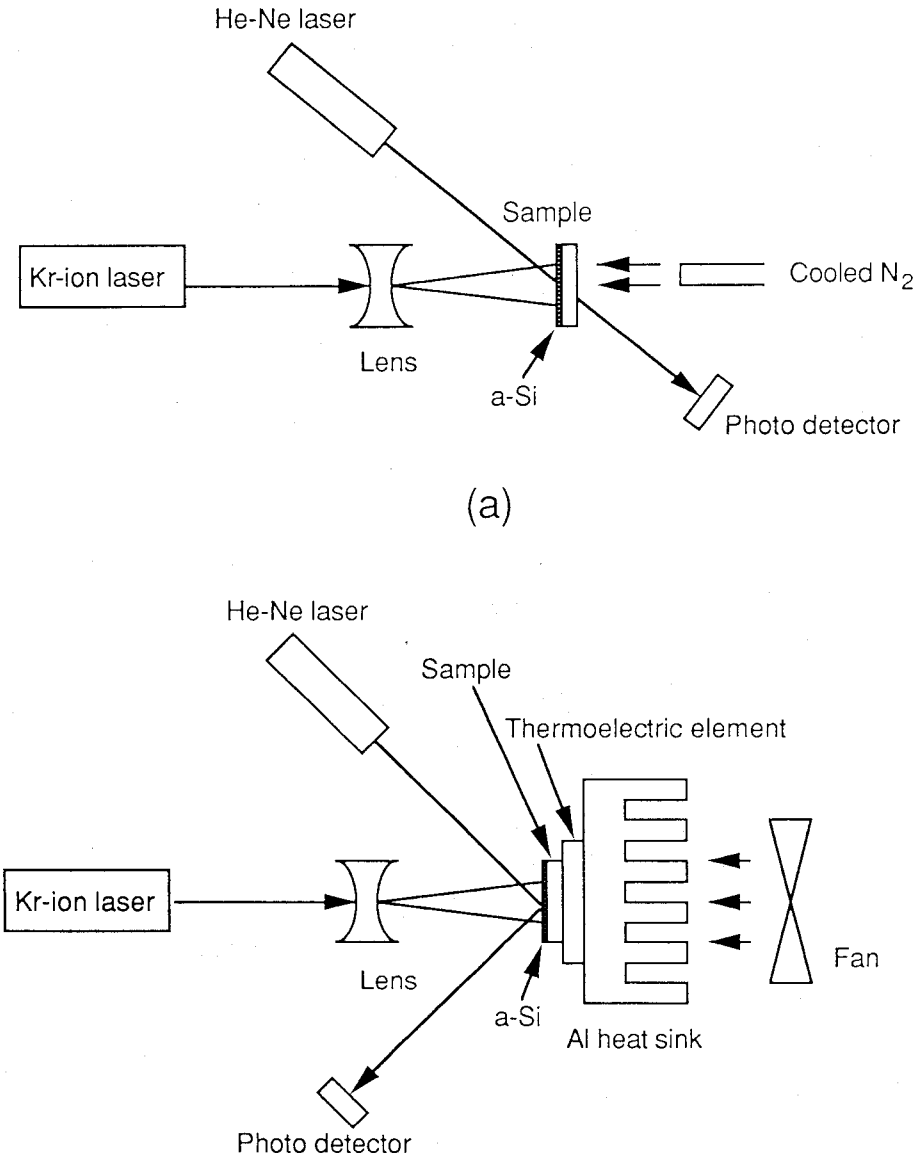

Fig. 2-1 Schematic diagram of the sample configuration for Kr^+ laser-soaking. (a) Standard configuration; (b) Configuration for experiments with controlled sample temperature.

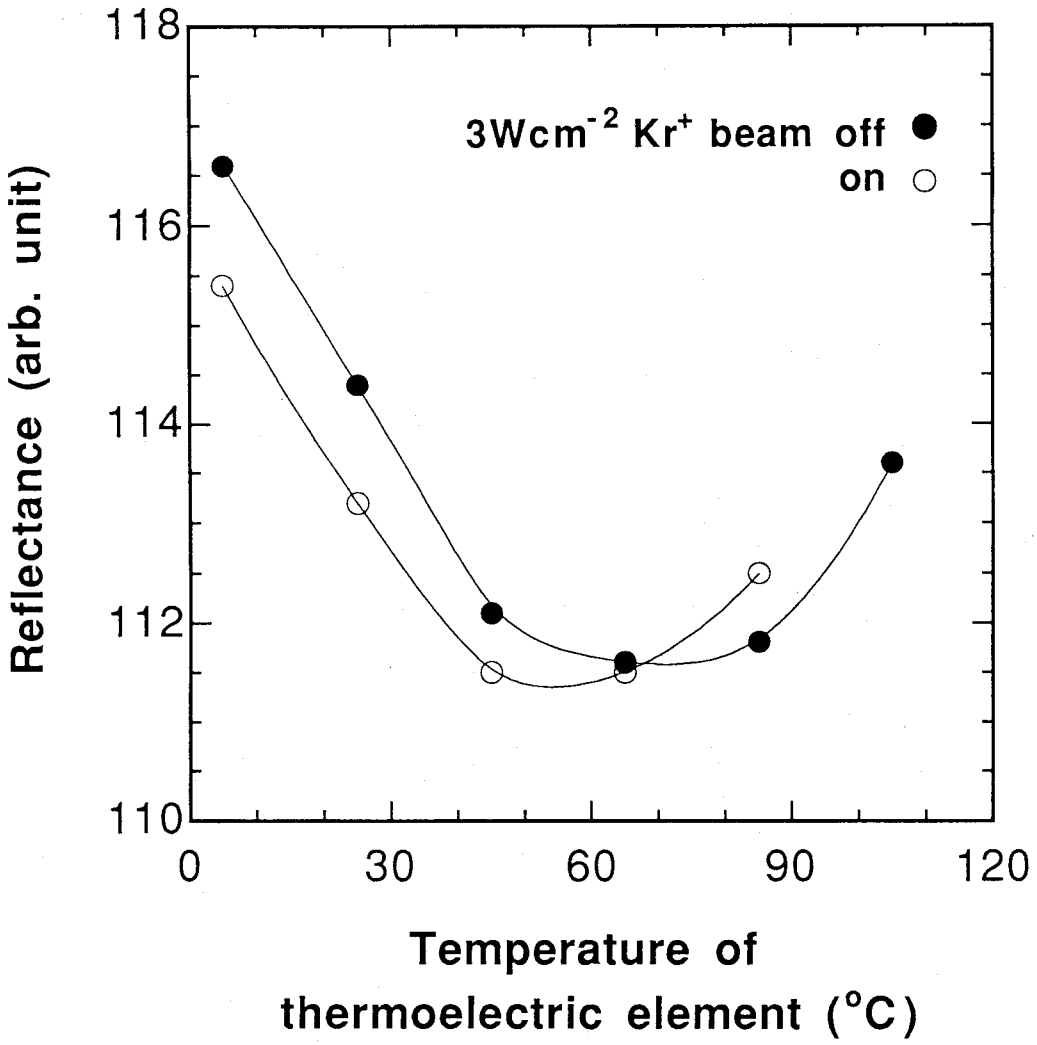

Fig. 2-2 Reflectance of a He-Ne laser beam off an a-Si:H sample as a function of the temperature of the thermoelectric element (Fig.1 (b)) when the Kr^{+} laser is on (○) or off (●).

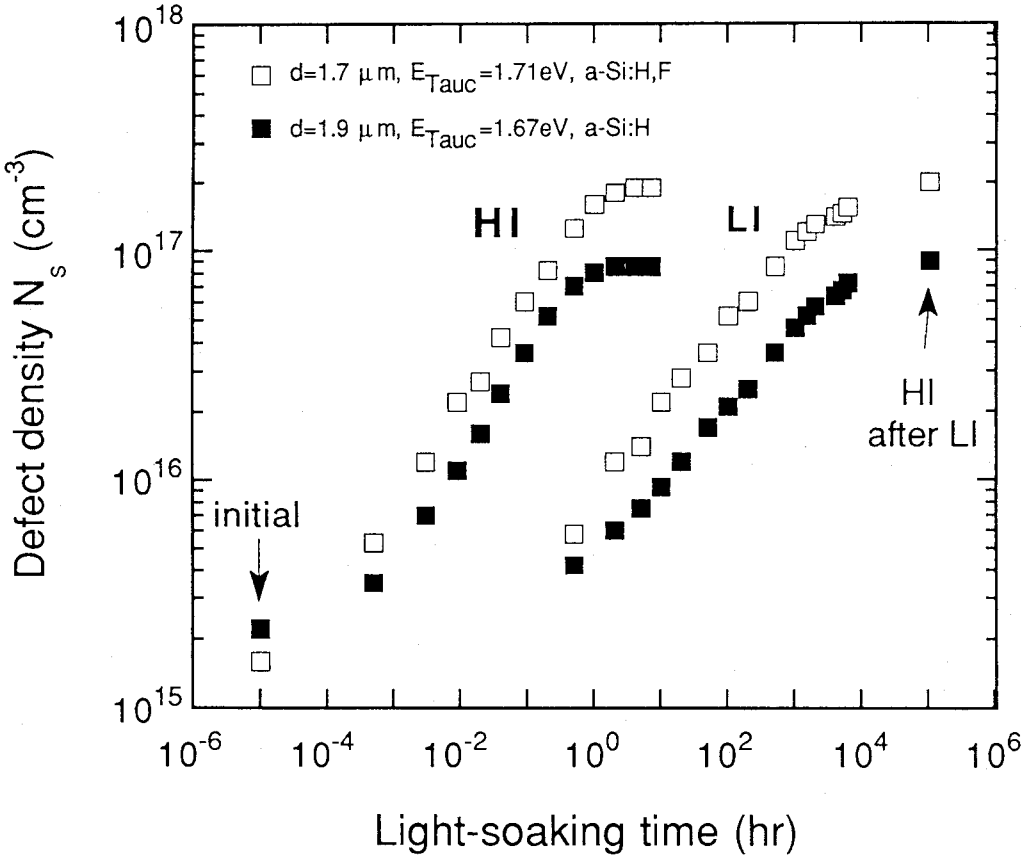

Fig. 2-3 Exsamples of defect buildup with light-soaking. Right: Defect build-up at low intensity ($G=5\times10^{20}$ $cm^{-3}s^{-1}$) light-soaking followed by high intensity (3×10^{22} $cm^{-3}s^{-1}$) soaking. Left: High intensity throughout.

saturate between 1,000 and 10,000 hours. With Kr^+ laser-soaking, G is $3x10^{22}$ $cm^{-3}s^{-1}$, and the entire defect build-up to saturation can be traced out within a few hours. The data of Fig. 2-3 show several interesting features. One is that the saturation values N_{sat} do not depend on light intensity. The time to reach saturation, however, is shortened substantially by raising the intensity. The data show that the rate of defect growth is accelerated by a factor which is approximately proportional to G^2; after raising G from $5x10^{20}$ $cm^{-3}s^{-1}$ to $3x10^{22}$ $cm^{-3}s^{-1}$ (by a factor of 60) saturation is reached 1,000 to 10,000 times faster. Another observation is that the overall shape of the curve that describes defect growth does not depend on light intensity. This means that the kinetics of defect build-up do not vary substantially over the range of intensities in this experiment.

The independence of N_{sat} from G makes the saturation procedure precise and reproducible because N_{sat} will not change with small variations of the generation rate in the sample. This feature stands in strong contrast to the sensitivity of the intermediate values of defect density (N_S) to small variations of G, which is evident from Fig. 2-3. In order to determine precise N_{sat} values, ensuring a sufficiently high generation rate or soaking for a sufficiently long time remains important. The optical gaps of a-Si:H films vary approximately from 1.6 to 1.85 eV. Because of inadequate light penetration, most of the thickness of a low-gap or thick film may become saturated except for a layer at its bottom. Care must be taken to ensure that the stated G is reached throughout the sample.

2.2.3 Relation of the defect growth rate to the saturation value

For solar cells a rapid stability test is more desirable than a rapid measurement of N_{sat} because solar cells may no longer be useful by the time the defect density in the intrinsic layer has reached N_{sat}. The useful life of a solar cell ends at some intermediate value of N_S. After studying data such as those presented in Fig. 2-3, it has been concluded that a close correlation exists between N_{sat} and the rate of defect growth, particularly for a-Si:H of solar cell quality. This correlation permits us to trace out the entire defect history of light-soaked samples just from a measurement of N_{sat}.

The investigation of the correlation between the growth rate of the defect density under light-soaking, dN_S/dt, and the saturated value N_{sat} benefitted greatly from the availability of quantitative models for the defect build-up. Two important models exist. These are the stretched exponential model of Redfield and Bube [14] and the recombination model of Stutzmann, Jackson and Tsai [15]. While these models rely on different approaches to the physics of defect production and provide different rate laws, both models fit the observations reasonably well over a wide range of conditions.

A key feature of the stretched-exponential model is the assumption that the defect density saturates. The defect density N_S is given by

$$N_S=N_{sat}-(N_{sat}-N_O)\exp(-Kt^{\beta}), \qquad (2\text{-}1)$$

$$K=(1/\beta)(C_1+C_2)GP^{(1-\beta)}. \qquad (2\text{-}2)$$

N_O is the defect density of the sample in its initial state. K is a rate constant which includes constants describing the effectiveness of the optical generation C_1 and optical annealing C_2 of defects, the carrier generation rate G, a quantity with the dimensions of a vibrational period P and a parameter describing the dispersive process, $\beta=T(K)/605$. In this model the intermediate defect density N_S explicitly depends on N_{sat}. It is therefore no surprise to find a correlation between N_S and N_{sat}.

The recombination model predicts the saturation of N_S only under conditions where the defects are annealed thermally during illumination. In many cases this model offers a good explanation of the defect creation rate at intermediate N_S values. Therefore, it is interesting to investigate the correlation of dN_S/dt with N_{sat} using this model. In the recombination model, the rate of defect growth is determined by a rate constant C_{sw} and the carrier generation rate G:

$$dN_S/dt=C_{sw}(G/N_S)^2. \qquad (2\text{-}3)$$

Integration to time t gives

$$N_S^3 - N_O^3 = 3C_{sw}G^2t \,. \qquad (2\text{-}4)$$

Once Ns has risen sufficiently above N_O, Eq. 2-4 can be simplified to

$$Ns \sim (3C_{sw})^{1/3}G^{2/3}t^{1/3}. \qquad (2\text{-}5)$$

The data for defect build-up during light-soaking are conventionally plotted in a form suggested by Eq. 2-5, i.e., on a double-logarithmic scale of N_S vs. t. Plotted in this form, $\log(N_S)$ rises with illumination time with a slope of 1/3.

The fits to these two rate laws with two sets of data are illustrated. Figure 2-4 shows three sets of data from measurements on material prepared in the same deposition run (by a RF excited GD) and light-soaked at *three different intensities*. The data set of Fig. 2-5 shows defect growth at low-intensity (LI) soaking of *three different samples*. The carrier generation rates were $G=3\times10^{22}$ $cm^{-3}s^{-1}$, 2×10^{21} $cm^{-3}s^{-1}$ and 5×10^{20} $cm^{-3}s^{-1}$ for the intensities HI, MI and LI, respectively. The sample temperatures were 50°C to 70°C for HI, 20°C to 30°C for MI and 35°C for LI light-soaking conditions. The solid curves in Figs. 2-4 and 2-5 are fits to the stretched-exponential model of Eq. 2-1. The dashed lines, with slope of 1/3, illustrate fits to the recombination model as formulated in Eq. 2-4.

The temperatures used for fitting the stretched-exponential model were 70°C for HI, 25°C for MI and 35°C for LI soaking conditions. The rate constant K of Eq. 2-2 under LI conditions is nearly constant at $\sim4\times10^{-4}s^{-1}$. Thus, with prior knowledge of N_o, N_{sat}, t and G, and using this value of K, we can calculate the entire Ns(t) curve. It should be noted that the stretched-exponential model does fit most of the experimental data well.

At intermediate defect densities the recombination model also fits most of the data, with the exception of the HI curve in Fig. 2-4. This exception may result from a temperature dependence of C_{sw}. Because of the very brief light-soaking times used for the first several data points, the temperature of the film may not have been stabilized. The data of Fig. 2-5 suggest a correlation between C_{sw} and N_{sat} because a slower build-up of defects (A65<A57<A29) corresponds to a lower N_{sat}. It can be seen shortly that such a correlation indeed does exist. To

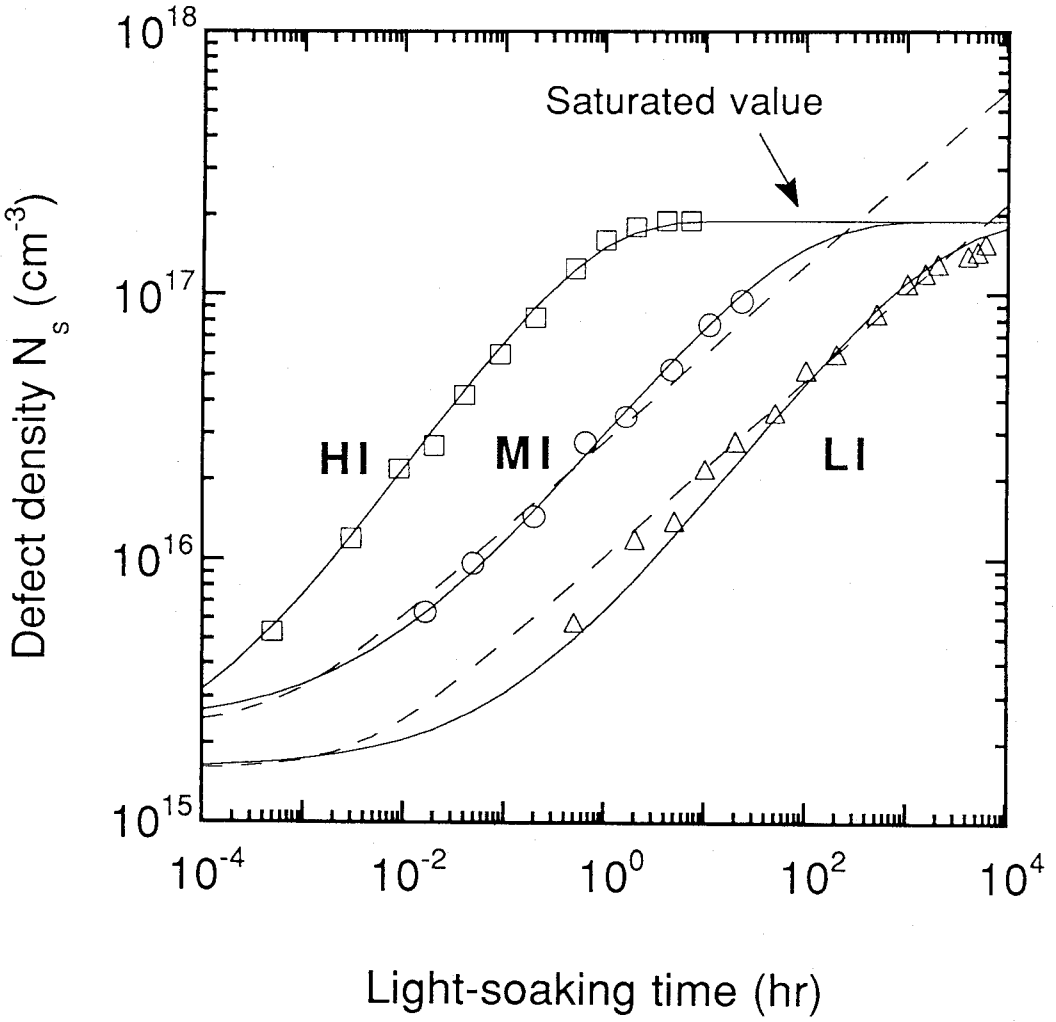

Fig. 2-4 Defect density N_S as a function of light-soaking time of sample under LI($G=5\times10^{20}$ $cm^{-3}s^{-1}$), MI(2×10^{21} $cm^{-3}s^{-1}$) and HI(3×10^{22} $cm^{-3}s^{-1}$). The solid and dashed lines are fits to the stretched exponential model and the recombination model, respectively.

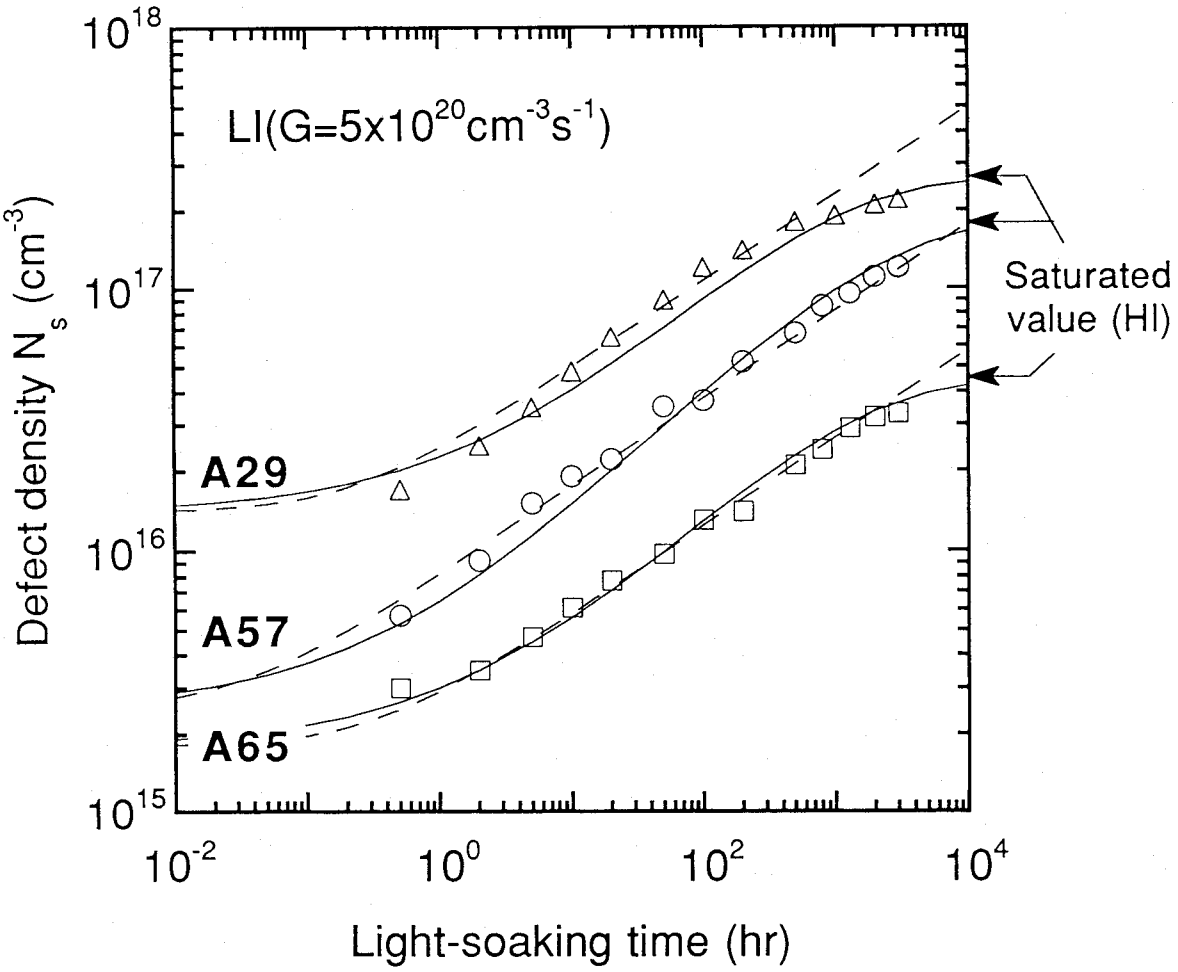

Fig. 2-5 Defect density N_S as a function of light soaking time for samples A29, A57 and A65 under LI conditions. The solid and dashed lines show fits to the stretched exponential model and the recombination model, respectively.

determine this correlation more precisely and quantitatively, C_{sw} is computed using Eq. 2-4 from pairs of values of $N_S(t)$ obtained by the soaking of five samples under LI conditions. The result is shown in Fig. 2-6 where the saturation regime at a very long time has not been included. C_{sw} remains constant over a long period in comparatively stable samples like A65 or A62, but not in less stable samples such as A44 or A29. Because the LI conditions are similar to typical sunlight intensity, Fig. 2-6 suggests that we may use C_{sw} as a stability criterion especially for comparatively stable a-Si:H. To see that C_{sw} under LI conditions is correlated with N_{sat}, the C_{sw} values given by the horizontal lines of Fig. 2-6 are plotted against N_{sat} determined under HI conditions in Fig. 2-7. Clearly, C_{sw} for LI conditions can be predicted from N_{sat}.

For the practical purpose of predicting dN_S/dt from N_{sat} at intermediate N_S, the two models agree under LI conditions. Therefore, N_{sat} is a robust criterion for predicting the "usable life" of a-Si:H materials and of solar cells.

2.2.4 Correlation between the saturation value and the properties of the materials

Measurements were proceeded to identify any correlations of N_{sat} with key structural, optical and chemical properties. Such correlations help to optimize deposition conditions for more stable i-layer material. In addition, they may serve to identify the microscopic mechanism of light-induced defect generation.

The annealed-state and saturated defect densities, N_o and N_{sat}, respectively, of several groups of samples prepared by different methods are plotted vs. their Urbach energies E_u in Fig. 2-8. N_o rises with E_u as is expected from models in which dangling bonds are produced by the breaking of weak Si-Si bonds [16]. N_{sat}, on the other hand, shows no clear dependence on E_u for these groups of samples. Rather, N_{sat} is correlated with the optical gap and the hydrogen concentration. Fig. 2-9 shows N_{sat} as a function of the Tauc gap of the samples. The solid line is the current estimate of the lower limit for N_{sat} as a function of E_{Tauc}. The correlation is less tight but persists when N_{sat} is plotted as a function of E_{04} (photon energy at absorption coefficient of 10^4 cm^{-1}) in Fig. 2-10. N_{sat} is plotted against the total hydrogen content c_H of the samples in Fig. 2-11, which again suggests a correlation. E_{Tauc} increases with

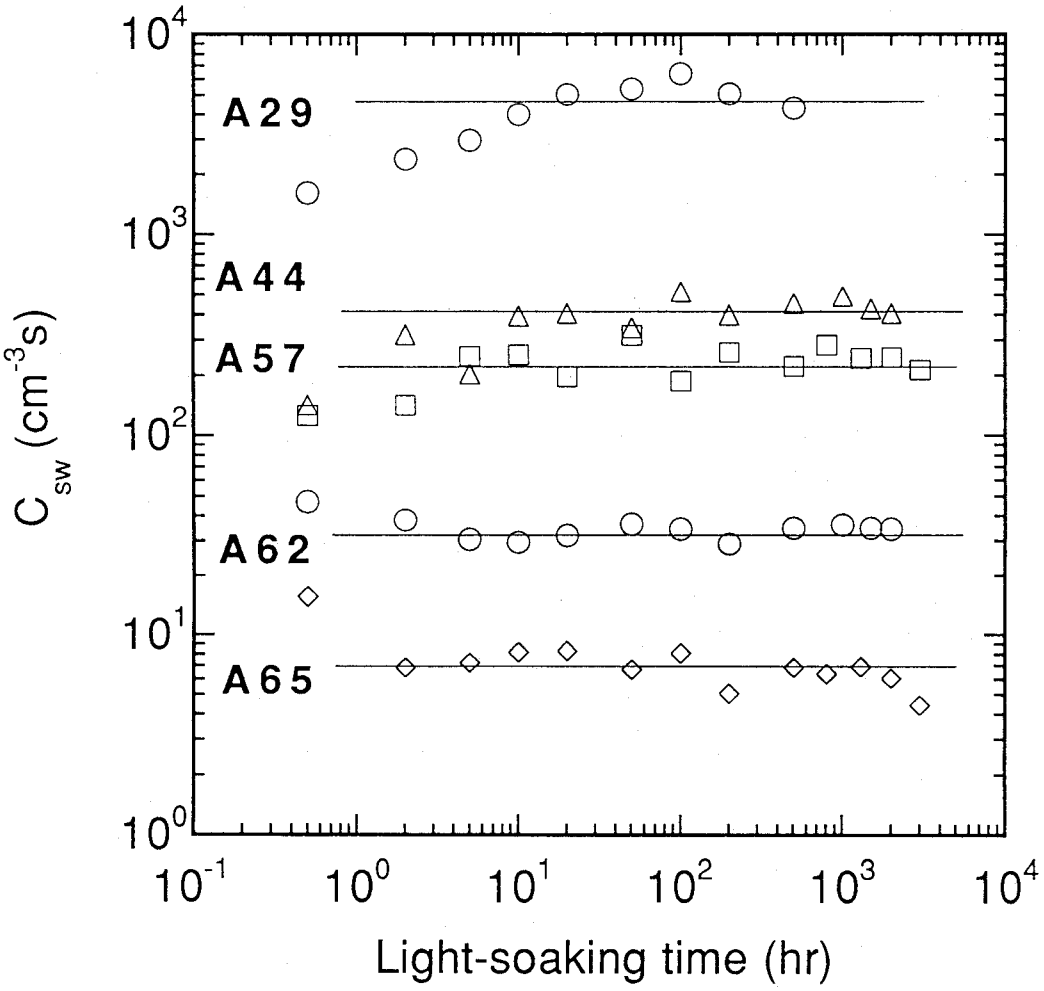

Fig. 2-6 The rate constant C_{sw} as a function of light-soaking time for five samples. Horizontal lines are fits of C_{sw}.

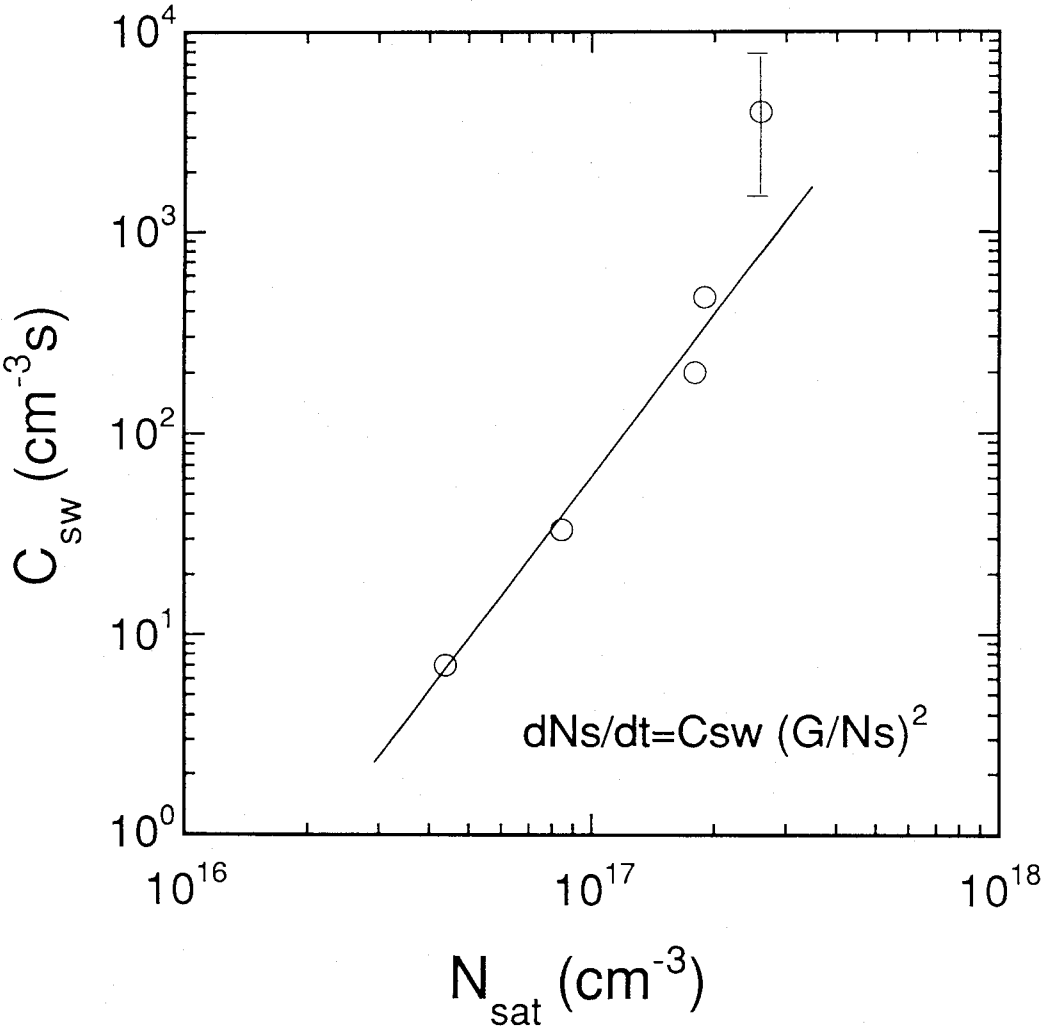

Fig. 2-7 The rate constant C_{sw} under LI conditions as a function of the saturated defect density N_{sat} obtained under HI conditions.

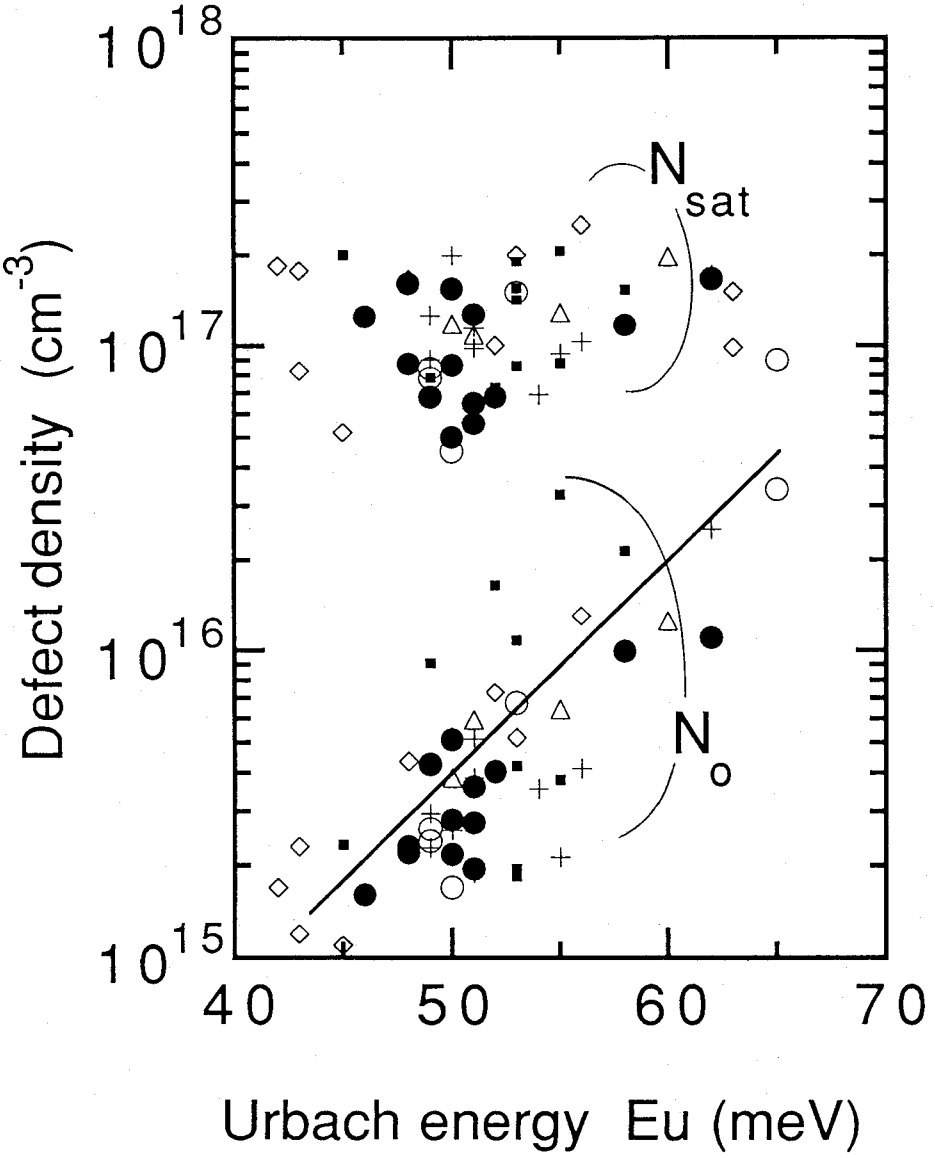

Fig. 2-8 Initial (N_o) and saturated (N_{sat}) defect densities, plotted vs. Urbach energy (E_u) for samples deposited by six techniques. (+) UHV RF(13.56MHz) GD, (●) RF(13.56MHz) GD, (△) RF(70MHz) GD, (■) DC magnetron reactive sputtering, (○) triode DC GD and (◇) triode DC GD with fluorine sorce gases.

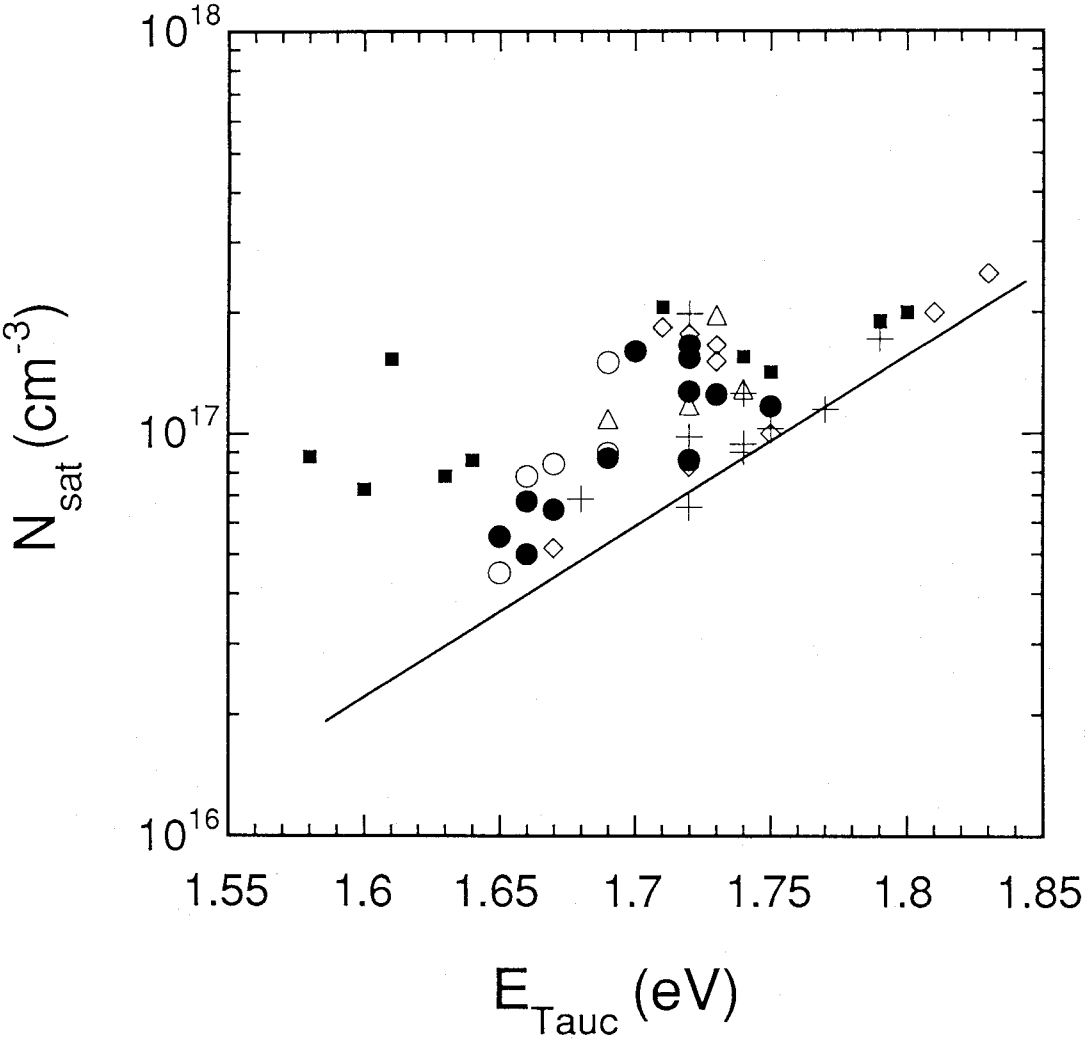

Fig. 2-9 Saturated defect density N_{sat} as a function of E_{Tauc}. The solid line is an estimated minimum of N_{sat}. Symbols as in Fig. 2-8.

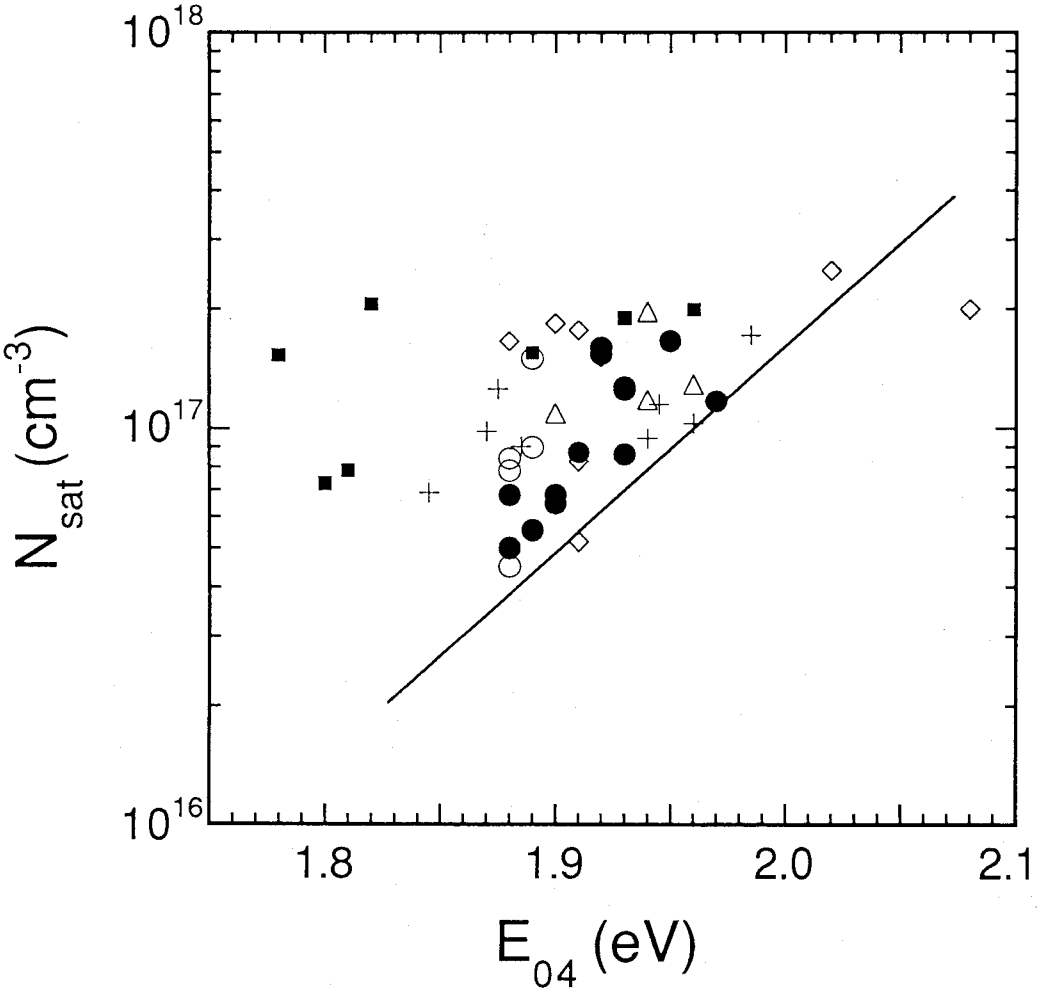

Fig. 2-10 Saturated defect density N_{sat} as a function of E_{04}. Symbols as in Fig. 2-8.

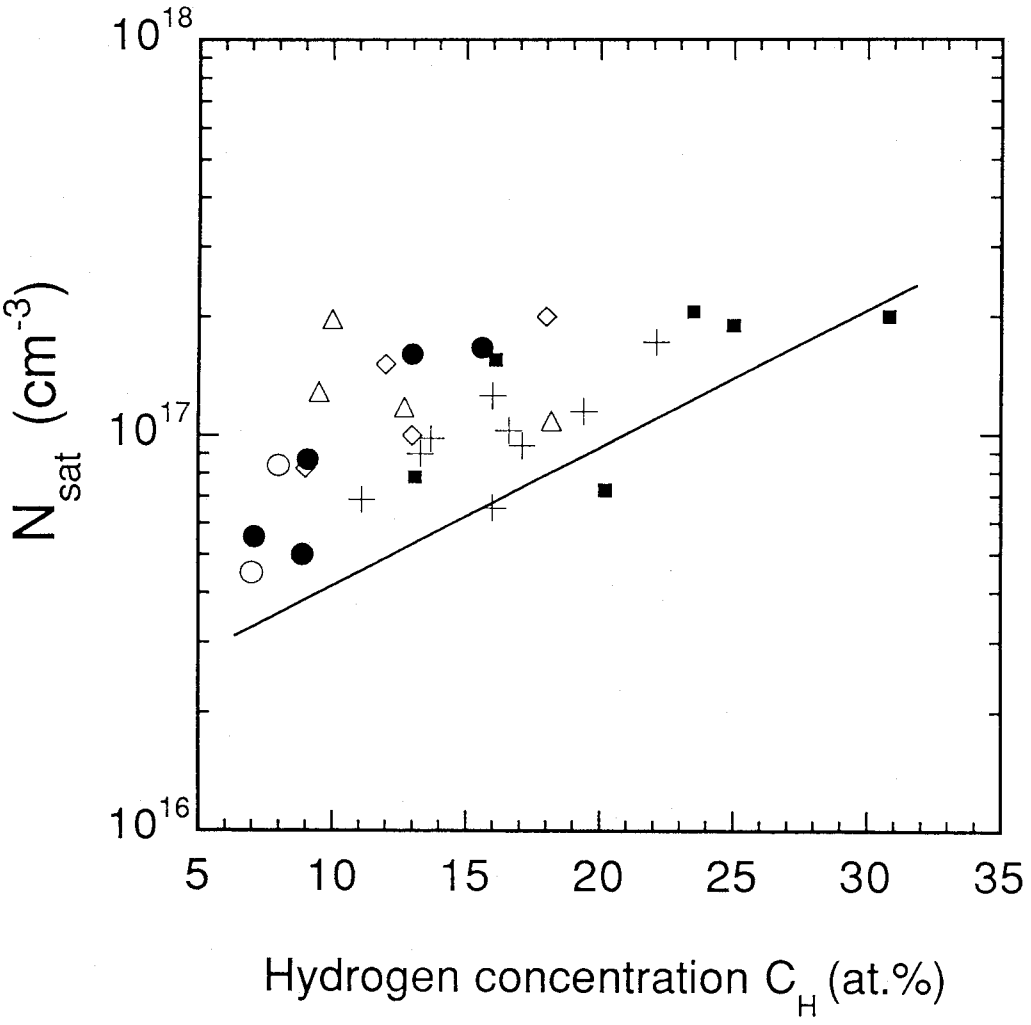

Fig. 2-11 Saturated defect density N_{sat} as a function of hydrogen concentration c_H. Symbols as in Fig. 2-8.

increasing c_H, therefore it is not surprising to find the correlations of Figs. 2-9 and 2-10 together with that of Fig. 2-11. Hydrogen in the SiH_2 configuration has often been associated with the occurrence of metastable defects [17]. The correlation between Nsat and c_{SiH2} illustrated in Fig. 2-12 supports this claim. The photoconductivities σ_{ph} of the samples whose N_S values have saturated appear to agree with the correlations evident from Figs. 2-9 and 2-10. The σ_{ph} values are plotted vs. E_{Tauc} in Fig. 2-13. Data grouped by deposition technique, which are denoted by different symbols, show that the overall trends identified here also apply to individual groups. Noticeable differences between these groups may allow the sorting of deposition techniques or combinations of source gases by their ability to produce stable a-Si:H.

The key correlations found between N_{sat} and the other properties of a-Si:H are those that relate N_{sat} to c_H. To identify the cause of defect build-up one must identify the primary cause of the variation of N_{sat}, which may be a chemico-structural effect reflected by c_H. Clearly this identification is of fundamental importance. In a more practical way, the correlations which have been identified already are helpful in guiding the design of a-Si:H materials.

2.3 What determines the maximum defect density

2.3.1 Temperature and light-intensity dependence of the saturation value

The saturated light-induced defect density can be affected by the temperature during light-soaking [2,15]. Observation of the temperature dependence of N_{sat} underscores the question of the mechanism for defect saturation. This mechanism could be the exhaustion of sites which are convertible to defects or the attainment of a steady state between annealing and the generation of defects. To answer this question, the temperature and light-intensity dependences of N_{sat} were measured while precisely controlling the temperature of the a-Si:H films during light-soaking. The sample temperature was controlled as shown in Fig. 2-1 (b).

The measurements of the temperature dependence of N_{sat} were conducted with a-Si:H films held at temperatures between 25°C and 130°C. The *same* sample was used for the measurement of N_{sat} to avoid the variation introduced by using different pieces. The sample was light-soaked at sequentially decreasing temperatures. As shown in Fig. 2-14, following saturation at 105°C the sample was saturated to a higher N_{sat} value at 85°C by additional

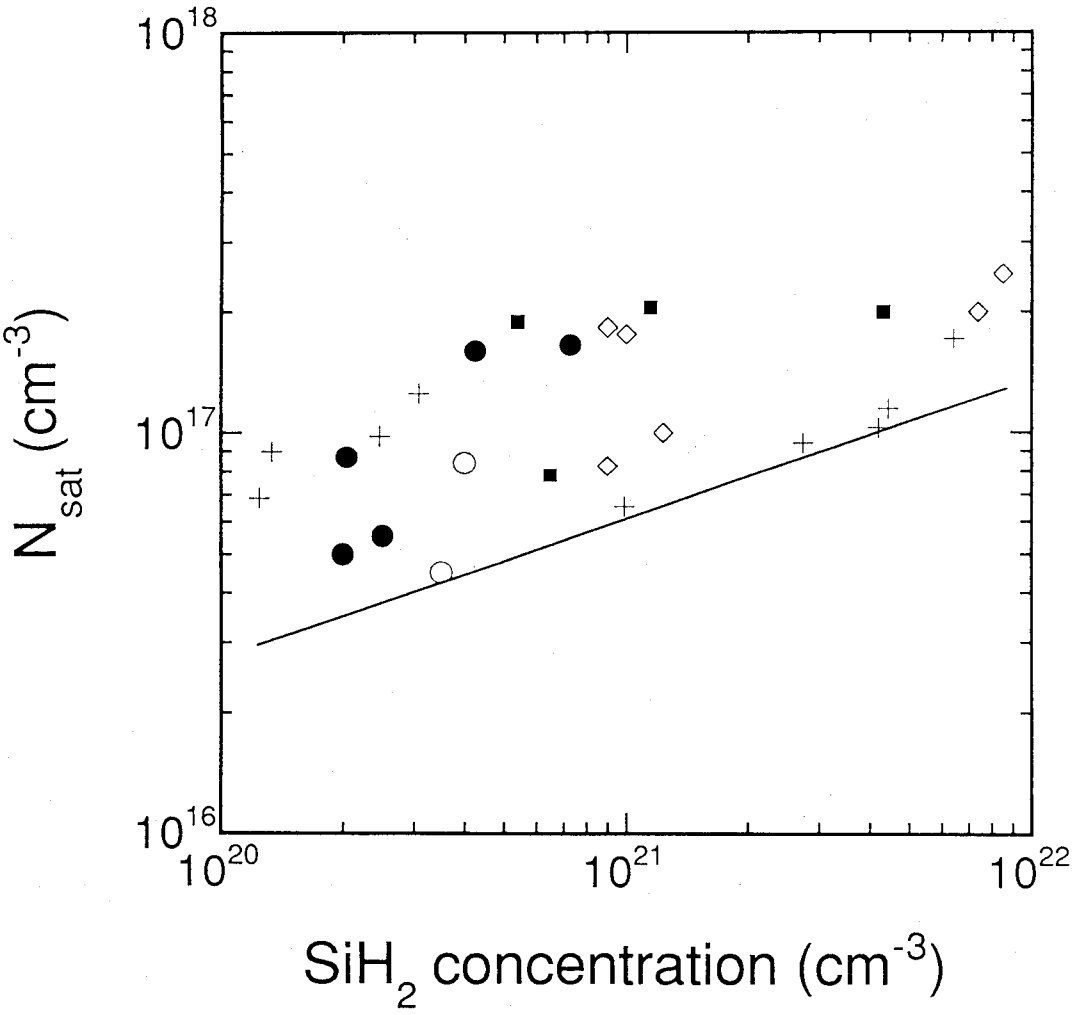

Fig. 2-12 Saturated defect density N_{sat} as a function of SiH_2 density. Symbols as in Fig. 2-8.

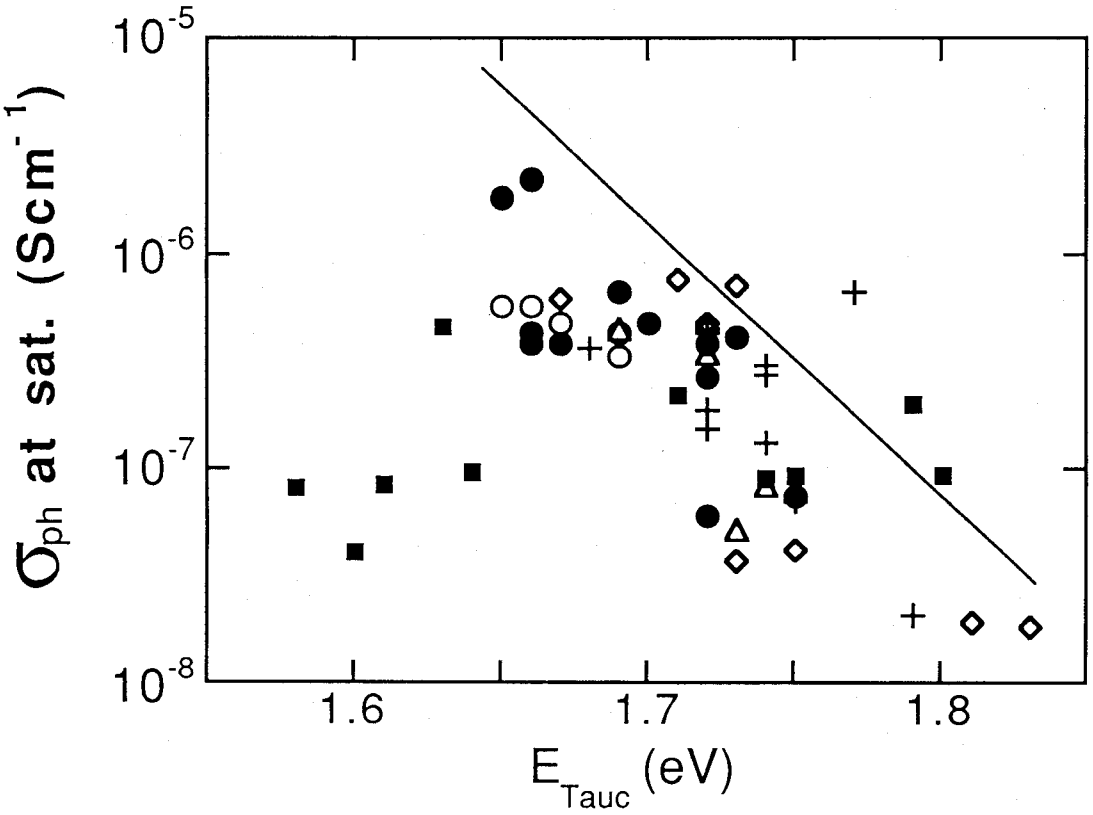

Fig. 2-13 Photoconductivity σ_{ph} at N_{sat} as a function of E_{Tauc}. Symbols as in Fig. 2-8.

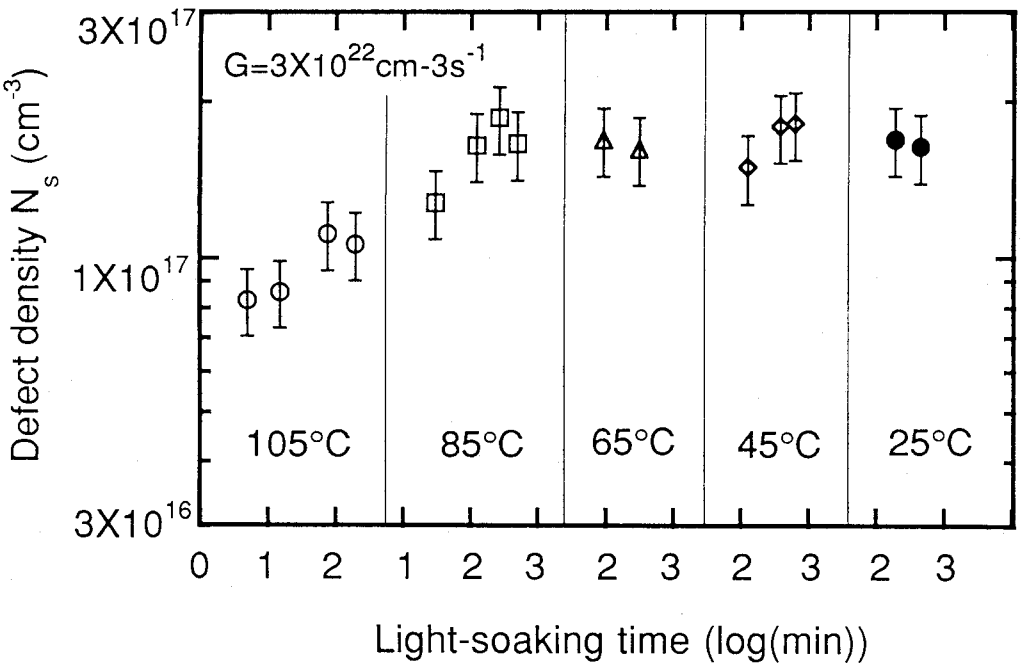

Fig. 2-14 Defect growth by sequential light soaking of one piece of sample at decreasing temperature. The light-soaking sequence proceeded from left to right. 105°C (○), 85°C (□), 65°C (△), 45°C (◇) and 25°C (●). Bars show estimated accuracy of ±15%.

illumination. Subsequent exposure at 65°C, 45°C and 25°C did not raise N_{sat} further. The result means that N_{sat} is not affected by temperature between 25°C and 85°C and that the N_{sat} value reached at 105°C is less than the values reached at the lower temperatures because of thermal annealing. In other words, thermal annealing does not affect N_{sat} below 85°C under the high-intensity light used in this experiment, so that N_{sat} must be limited by the exhaustion of defect sites. In Fig. 2-15 the saturation data of Fig. 2-14 are plotted together with all other saturation data of samples taken from the same substrate, as a function of illumination temperature. Each symbol in Fig. 2-15 represents a different piece of the sample. The data plots scatter within about ±30% because of piece-to-piece variations and CPM inaccuracy, but still show that N_{sat} is insensitive to temperatures below 90°C and that it drops at higher temperatures. The data for each individual piece show this tendency more clearly. It is concluded that N_{sat} is independent of temperatures below 90°C at the light intensity.

For the measurements of intensity dependence, two sample pieces were taken from the same substrate for the experiment on temperature dependence. Each piece was studied at 90°C and at 130°C, in a test of the effect of the light-intensity. Figures 2-16 and 2-17 show the result of sequential light soaking at increasing light intensity (carrier generation rate) at 90°C and 130°C. In Fig. 2-18, N_{sat} is plotted versus carrier generation rate. At both temperatures N_{sat} rises slowly with intensity. It can be seen in Fig. 2-15 that thermal annealing starts to affect the saturation at $G=3\times10^{22}$ $cm^{-3}\cdot s^{-1}$ above 90°C. Therefore, N_{sat} at the lower carrier generation rates G of 4×10^{21} to 2×10^{22} $cm^{-3}\cdot s^{-1}$ is expected to be reduced by thermal annealing at 90°C. The N_{sat} at 130°C is already in a steady state at $G=3\times10^{22} cm^{-3}\cdot s^{-1}$; here the intensity dependence at 130°C is naturally observed at lower generation rates.

2.3.2 Fitting with the defect pool model

The data show that N_{sat} is independent of temperature in the low-temperature region. This behavior of N_{sat} cannot be explained merely by a steady state between defect creation and thermal annealing. Another limiting factor which is independent of temperature is needed to explain this behavior of N_{sat}. Here the limited defect pool concept as illustrated in Fig. 2-19 [18-20] is used to model the behavior of N_{sat}. The concept of defect equilibrium originally

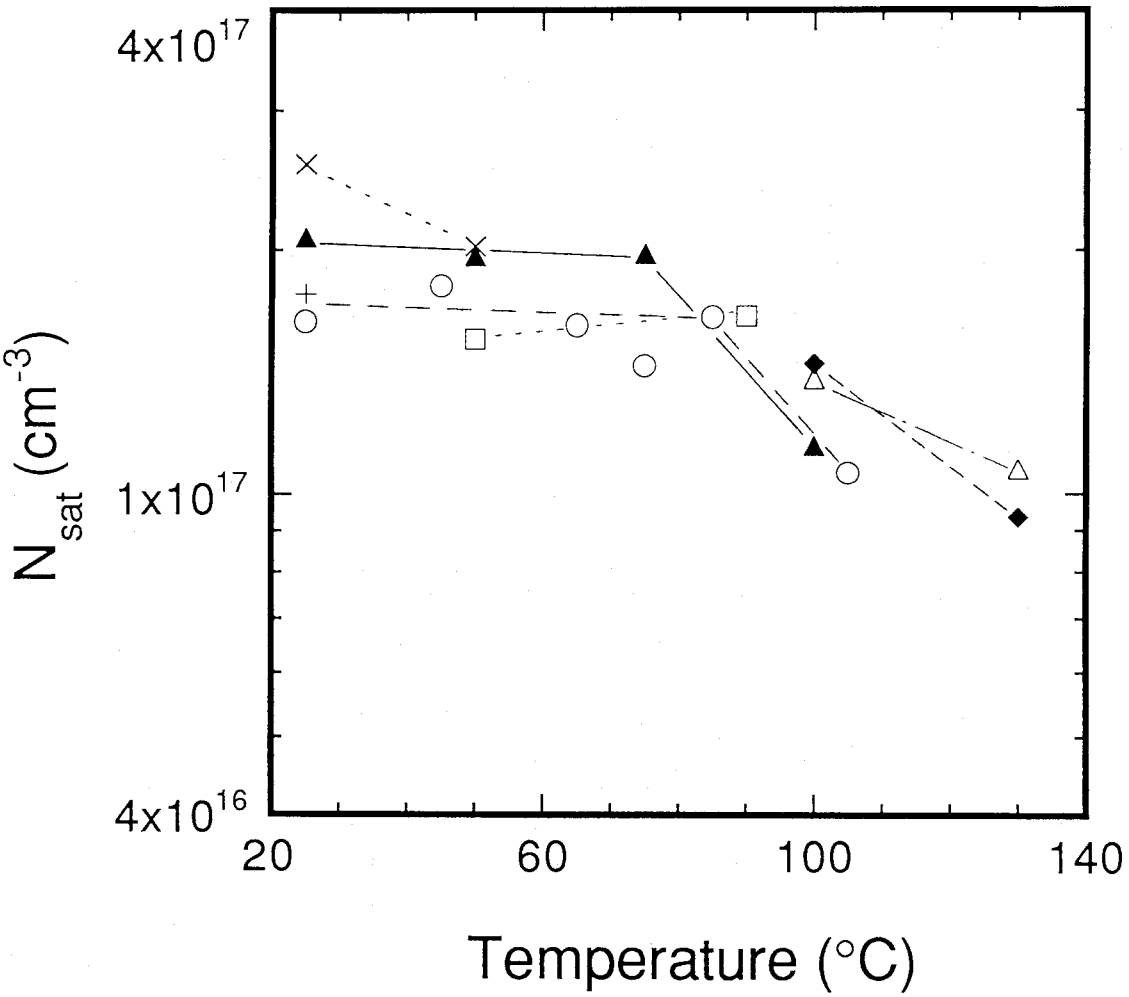

Fig. 2-15 Saturated defect density N_{sat} as a function of illumination temperature. All data were taken on pieces from the same substrate. Each symbol represents a different piece of sample.

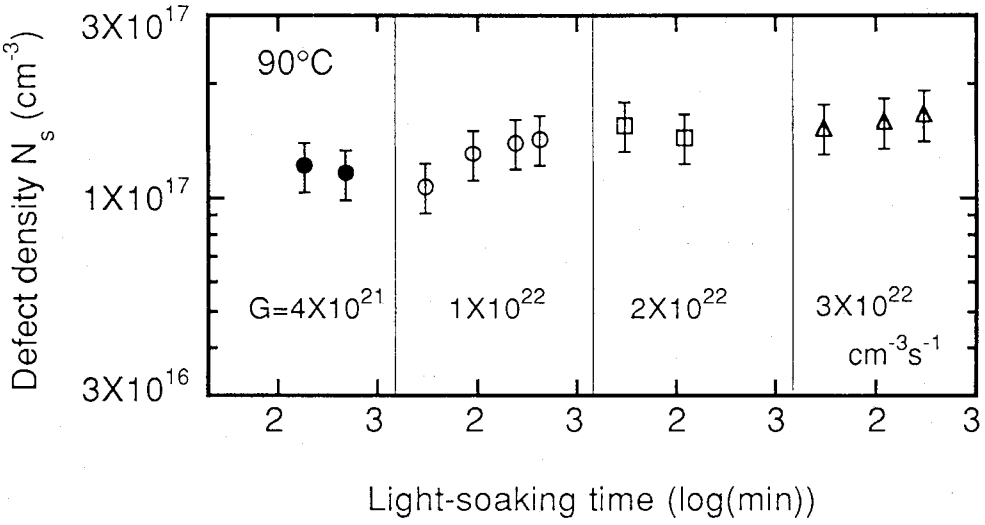

Fig. 2-16 Defect densities after light soaking at four carrier generation rates at 90°C. $4x10^{21}$ (●), $1x10^{22}$ (○), $2x10^{22}$ (□) and $3x10^{22}$ $cm^{-3}s^{-1}$ (△).

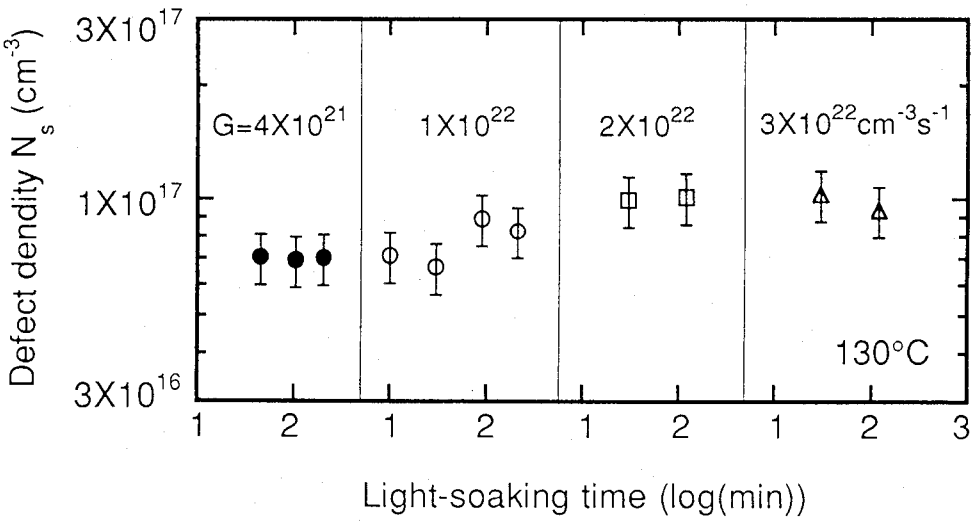

Fig. 2-17 Defect densities after light soaking at four carrier generation rates at 130°C. $4x10^{21}$ (●), $1x10^{22}$ (○), $2x10^{22}$ (□) and $3x10^{22}$ $cm^{-3}s^{-1}$ (△).

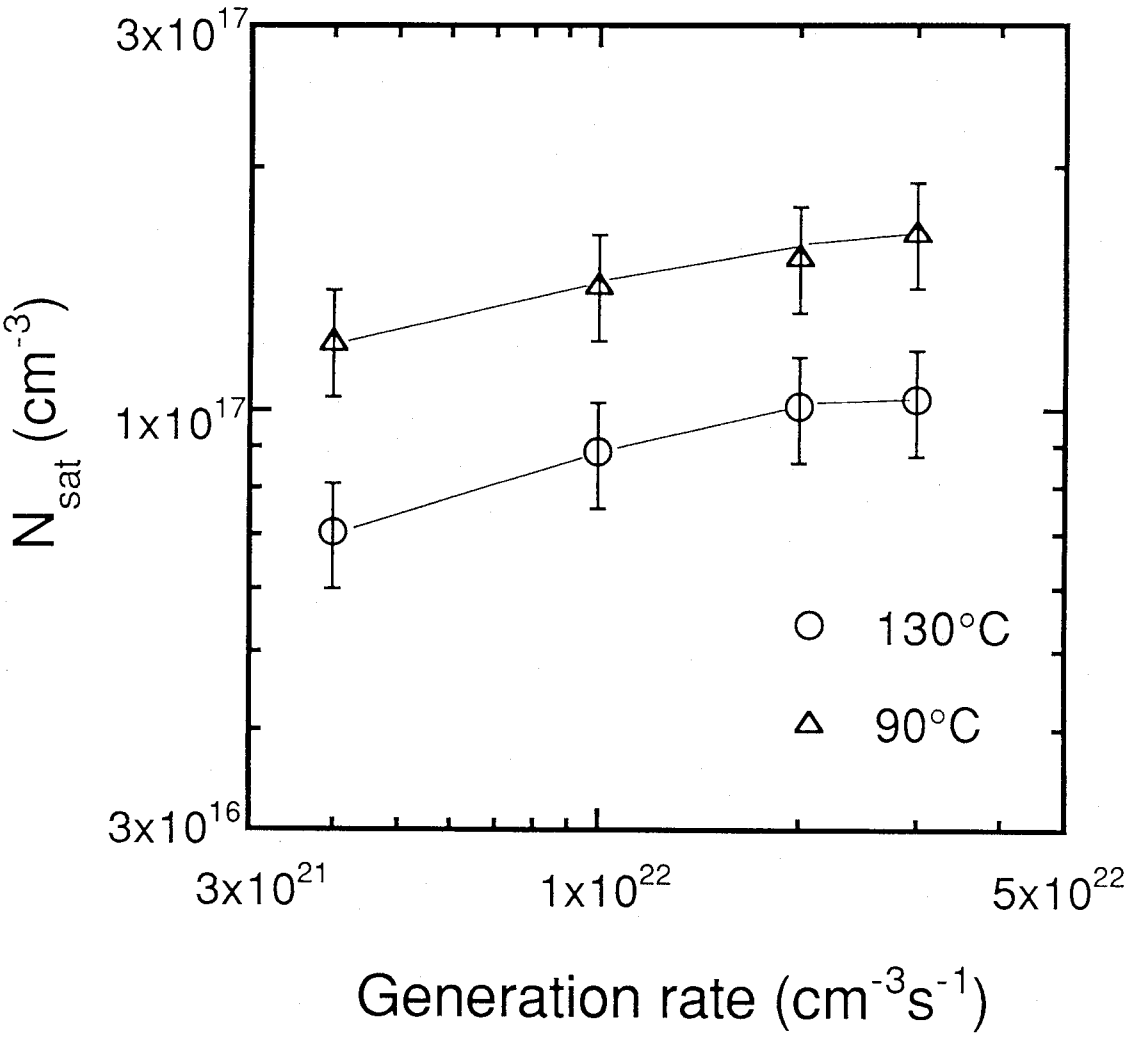

Fig. 2-18 Defect densities after light soaking at four carrier generation rates, at 90°C and 130°C.

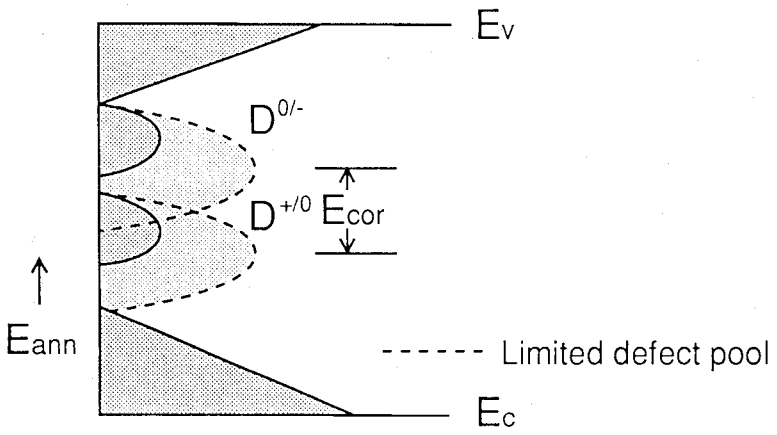

(a)

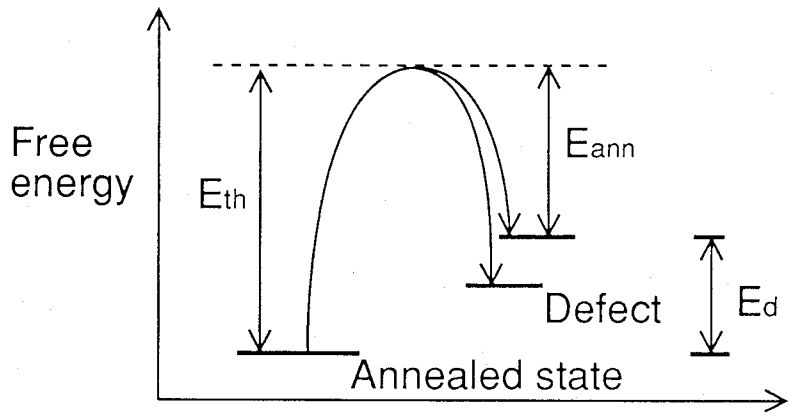

(b)

Fig. 2-19 The concept of the limitted defect pool model. (a) Schematic density of states distribution. (b) Free energy of electronic states.

introduced for thermally generated defects [21-24] is combined with the quasi-Fermi level to account for the rise in the Gibbs free energy of electrons and holes under steady-state carrier injection [4,20,25]. The gain in defect formation energy resulting from the shift of the quasi-Fermi energy levels is given by the energy differences between the electron Fermi energy (E_{Fn}) and $D^{0/-}$, and between $D^{+/0}$ and the hole Fermi energy (E_{Fp}), both of which should be added together after being multiplied by the occupancies of the charged defect states. Then the decrease of the defect formation energy is given as

$$\Delta E=f_n(E_{Fn}-E-E_{cor})+f_P(E-E_{Fp}), \qquad (2\text{-}6)$$

where f_n and f_p are the fraction of negatively and of positively charged defects, E is the defect energy counted from the valence band edge, and E_{cor} is the correlation energy of the defect states. Here, f_n and f_p are set by the ratio of electron and hole capture rates. Three coupled equations are solved to obtain the equilibrium defect density for a given carrier generation rate and temperature. One equation gives the defect density distribution N(E) as a function of temperature and formation energy E_d:

$$N(E;T,E_d)=P(E)/[1+\exp(E_d/kT)]. \qquad (2\text{-}7)$$

P(E) is the defect pool function, which is defined as the density of all defect states that can be produced; P(E) is assumed to have a Gaussian shape. E_d is given by

$$E_d=E_{th}-E-E_{cor}-\Delta E. \qquad (2\text{-}8)$$

Here, E_{th} is the activation energy for the thermal creation of defects. The second equation is the charge neutrality condition.

$$n+n_t+N^-=p+p_t+N^+, \qquad (2\text{-}9)$$

where n, n_t, N^-, p, p_t and N^+ are the densities of free electrons, trapped electrons, negatively charged defect states, free holes, trapped holes and positively charged defect states, respectively. Third is the non equilibrium steady-state statistics equations developed by Simmons and Taylor [26].

$$e_n = k_n N_c \, e^{-(E_c - E)/kT}, \qquad (2\text{-}10)$$

$$e_p = k_p N_v \, e^{-(E - E_v)/kT}, \qquad (2\text{-}11)$$

$$f_-/f_o = (k_n n + e_p)/(e_n + k_n n + k_p p + e_p), \qquad (2\text{-}12)$$

$$f_+/f_o = (k_p p + e_n)/(e_n + k_n n + k_p p + e_p), \qquad (2\text{-}13)$$

and

$$f_+ + f_o + f_- = 1, \qquad (2\text{-}14)$$

where e_n and e_p are the electron and hole emission rates, k_n and k_p the capture rate constant, N_c and N_v the effective densities of states at the conduction and valence band edges, and E_c and E_v the energies of the band edges. The values of the parameters used in the calculation are listed in Table 2-2.

Table 2-2 Parameters used in the numerical solution of the limited defect pool model.

Saturated defect density, N_{sat}	2.2×10^{17}	cm^{-3}
Defect formation energy, E_{th}	1.38	eV
Correlation energy of defect states, E_{cor}	0.4	eV
Capture rate constant for electrons, k_n	5×10^{-15}	cm^3s^{-1}
Capture rate constant for holes, k_p	5×10^{-15}	cm^3s^{-1}
Effective densities of states at the conduction band, N_c	2×10^{21}	cm^{-3}
Effective densities of states at the valence band, N_v	2×10^{21}	cm^{-3}
Mobility gap, E_c-E_v	1.9	eV

The temperature dependence of N_{sat} calculated by this quasi-equilibrium model is shown in Fig. 2-20 plotted against reciprocal temperature. The solid lines are N_{sat} values from the model calculation and the dashed line shows the thermal equilibrium value. Points are experimental data. By covering the temperature range from 0 to 500°C, and a G from 10^{18} to 10^{24} $cm^{-3}\cdot s^{-1}$, we produced all three regimes: (1) the maximum of N_{sat} is reached at high G and low T; (2) the extensive regime where N_{sat} depends strongly on G and T; and (3) the thermal equilibrium regime reached at high T and low G. A set of experimental N_{sat} values measured in function of T at $G=3x10^{22}$ $cm^{-3}\cdot s^{-1}$ follows the modelled temperature dependence. The G-dependence for sets of experimental data is modelled in Fig. 2-21. The data points depict experimental values of N_{sat} measured at four different light intensities, and at 90°C and 130°C. The curves, which by assumption reach the maximum N_{sat} of $2.2x10^{17}$ cm^{-3} are calculated with the model; a curve for 50°C is added to represent a typical solar cell operating temperature. These two calculation results agree with the experimental data well and suggest that the assumption in which the convertible defect sites are limited is reasonable. Models based on the limitless defect supply from the whole valence band tail states are difficult to explain the N_{sat} data which are independent of temperature.

The stretched exponential model by Redfield predicted the saturation behavior of N_{sat} by assuming a limited supply of the convertible sites [14] and also made good fittings of experimental data [27,28]. Their model explains that the smaller temperature dependence of N_{sat} in the lower-temperature region, in which the thermal-recovery rate is relatively low, is due to the limitation of the convertible sites.

Recent work by Schumm and Bauer [25] showed that the experimentally observed weak temperature dependence could also be reproduced with their assumptions on defect pool based on the limitless defect supply, but the validity of their assumptions requires careful examination because deviation from experimental data of N_{sat} is still large in the higher-temperature region, in which the data show rapid decrease with increasing temperature.

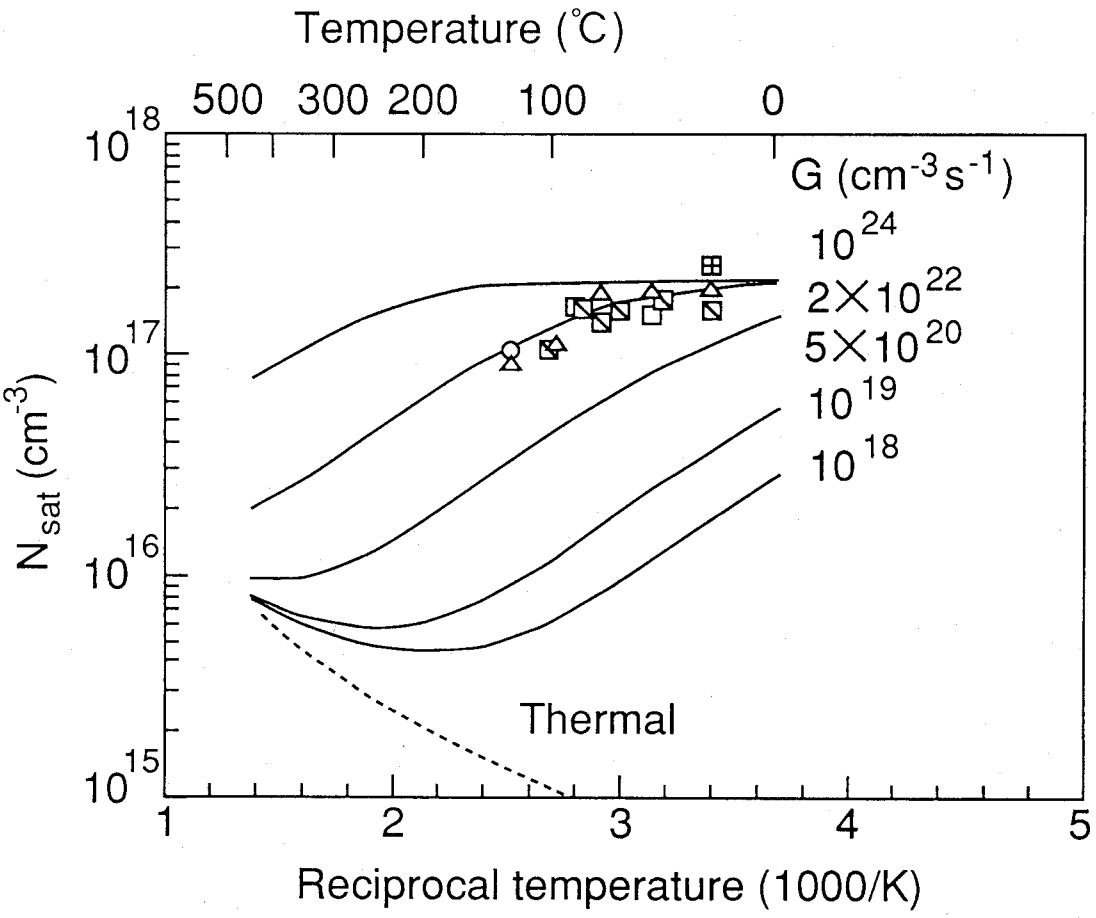

Fig. 2-20 Saturated defect density (N_{sat}) plotted against reciprocal temperature. The solid lines are results from the limited-pool defect source model and the dashed line shows the thermal equilibrium value. Points are experimental data.

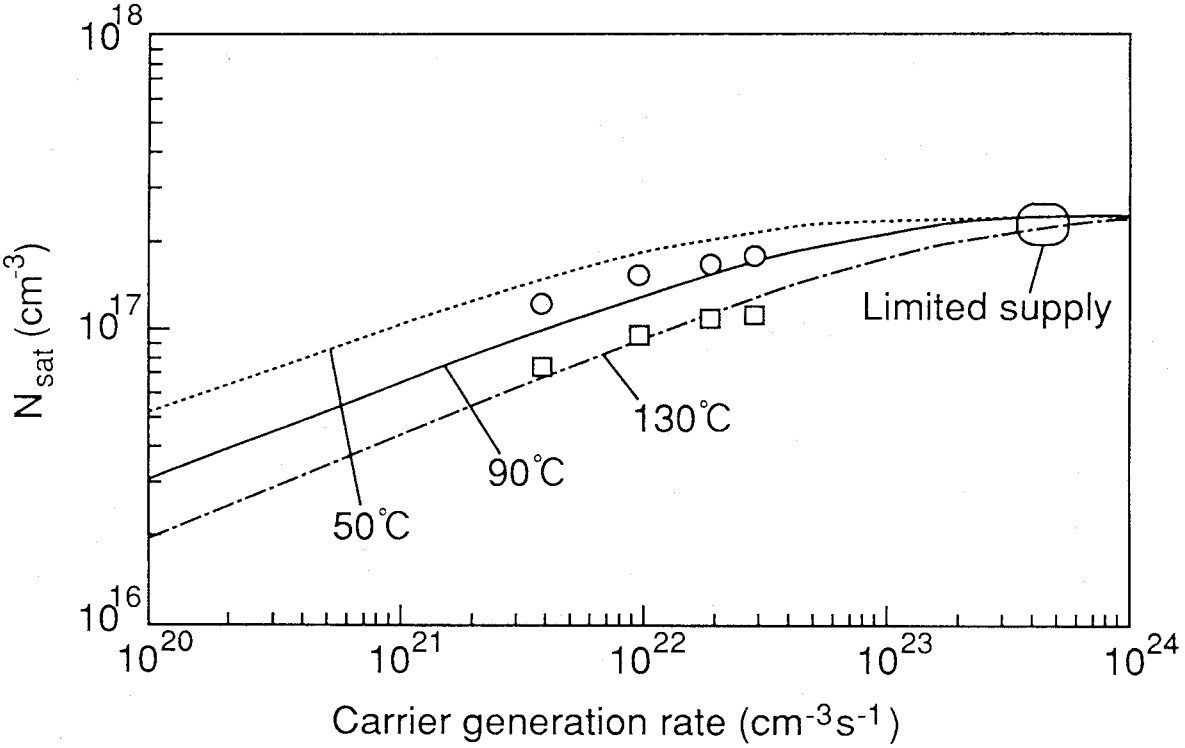

Fig. 2-21 Dependence of saturated defect density (N_{sat}) on the electron-hole pair generation rate G. Curves for 50, 90 and 130°C are the result of the model drawing on a limited supply of defects. Points are experimental data for four values of G at 90°C and 130°C.

2.3.3 Effect of change in the tail state on the saturation value

The Urbach energy E_u is considered to be a measure of strain in the a-Si:H material [16]. As E_u increases, more Si-Si bonds are broken. Thus the defect density in annealed a-Si:H is found to rise with increasing E_u. It is natural to expect the Urbach energy to affect N_{sat}, too, but we have not found a correlation in device-quality samples (E_u<60meV) made with various deposition methods from several laboratories, as shown in Fig. 2-8. This null result is surprising but it suggests that not all band tail states can be changed to defects, and that other limiting factors exist. To pursue this question further, samples taken from the same substrate were annealed at several temperatures between 160°C and 310°C for 14 to 24 hours in nitrogen gas. The samples were prepared with RF excited GD (glow discharge) on quartz substrates at 180°C. The annealings raise E_u, and reduce optical bandgap E_{Tauc} as shown in Figs. 2-22 and 2-23. The defect density in the annealed state, N_O, rises with E_u in agreement with many earlier observations as shown in Fig. 2-24. N_{sat}, on the other hand, remains unchanged up to E_u=55meV, and decreases at the point of 57meV for the sample annealed at 310°C. Here it was found again that E_u is not directly related to N_{sat}. It was already found that N_{sat} is correlated with E_{Tauc} and with the hydrogen concentration c_H in Subsection 2.2.4. It is possible that the drop of N_{sat} at 57meV in Fig. 2-24 goes hand in hand with the reduction of E_{Tauc} from 1.76eV to 1.70eV as shown in Fig. 2-23, due to the loss of hydrogen. The lower temperature anneals do not significantly reduce E_{Tauc}, so the N_{sat} of the 310°C sample may have been reduced through the loss of hydrogen.

Through this section, both the experimental data and the model calculations show that the tail states do not directly affect N_{sat} in device-quality a-Si:H and c_H is more important for limiting the number of defects than the tail states.

2.4 Prediction of the life time of the solar cells

The goal of stability work is improving the stability of solar cells. Applying the saturation technique to solar cells would be a more germane way for empirical sorting than the study of a-Si:H materials alone. To understand the light-soaking behavior of solar cells, the instability of the i-layer alone must be understood if other sources of instability in complete cells

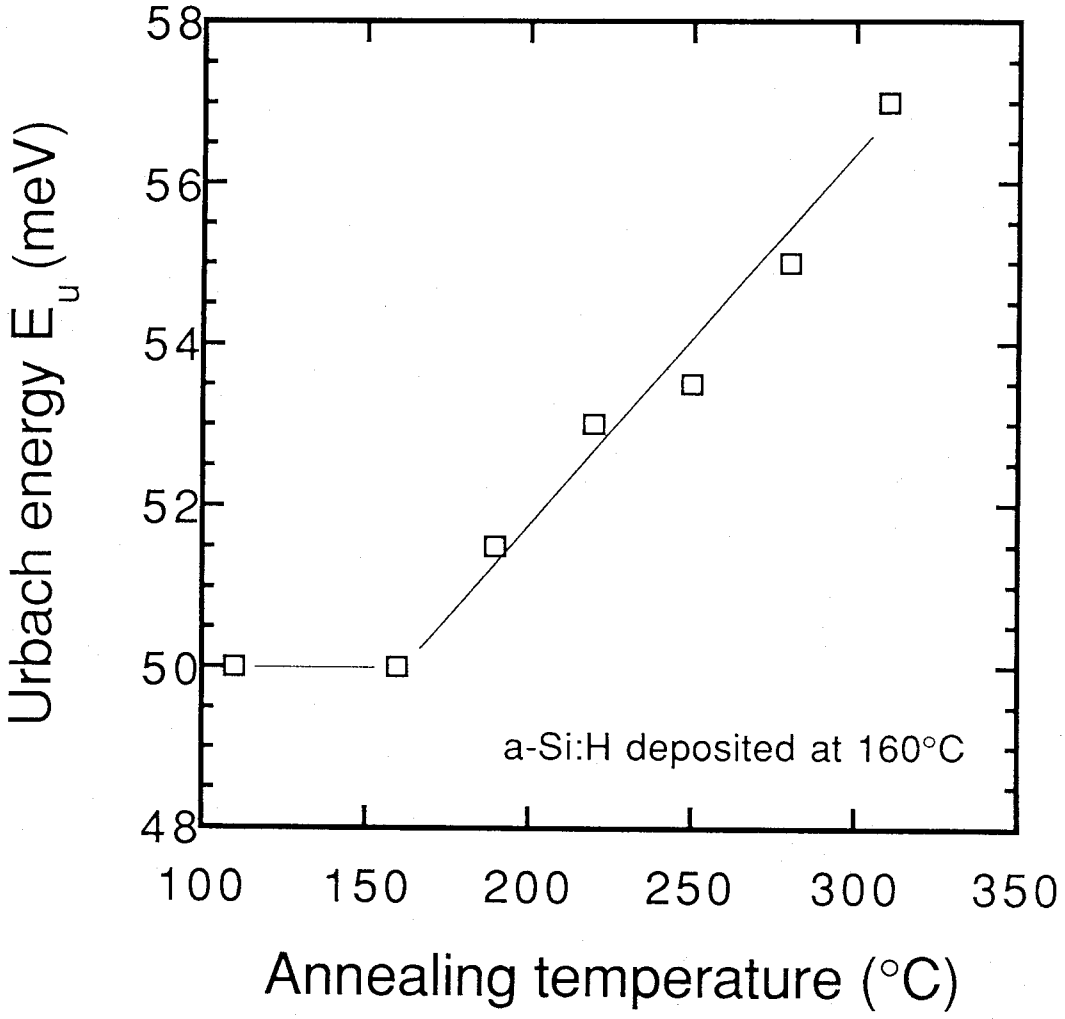

Fig. 2-22 Urbach energy (E_u) of the samples from the same substrate, annealed at temperatures between 160°C and 310°C.

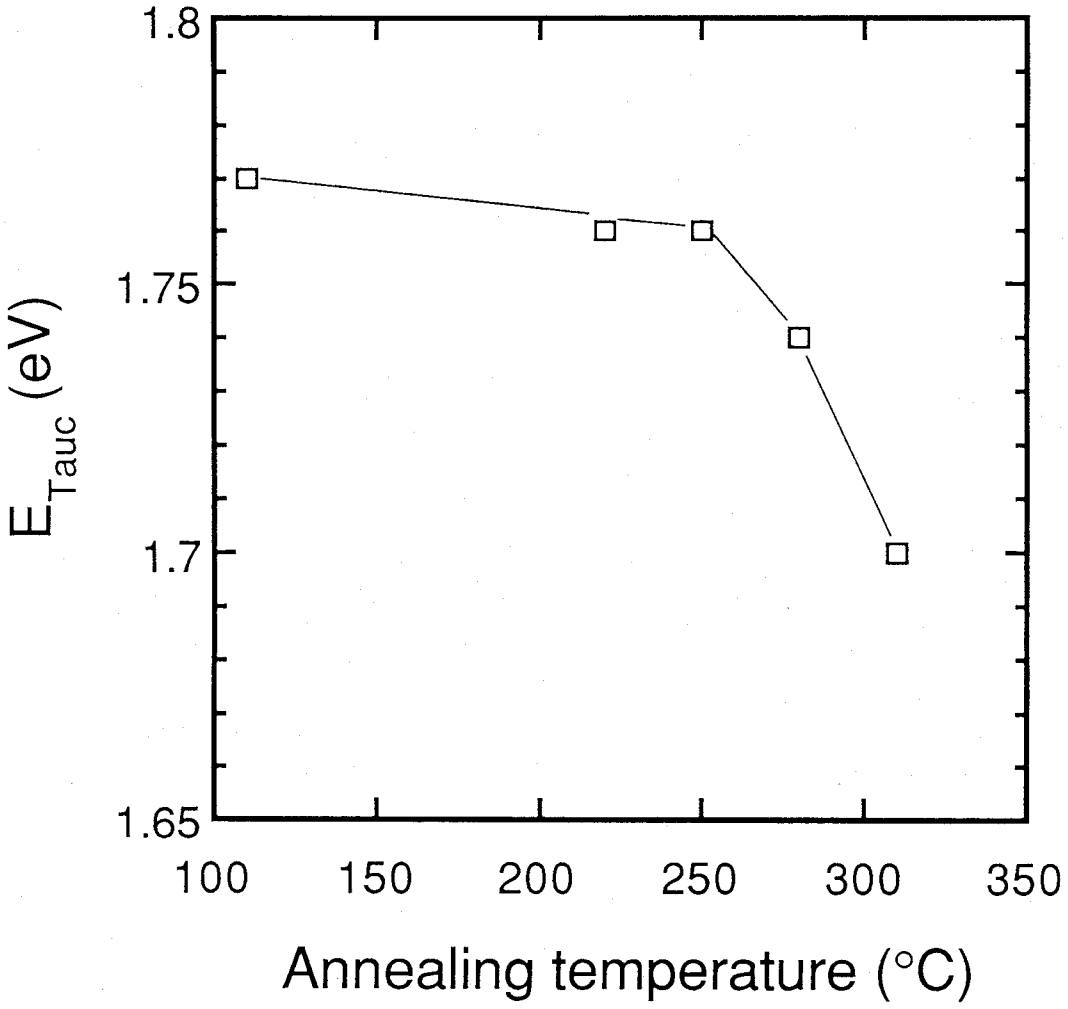

Fig. 2-23 Tauc gap (E_{Tauc}) of the samples from the same substrate, annealed at temperatures between 160°C and 310°C.

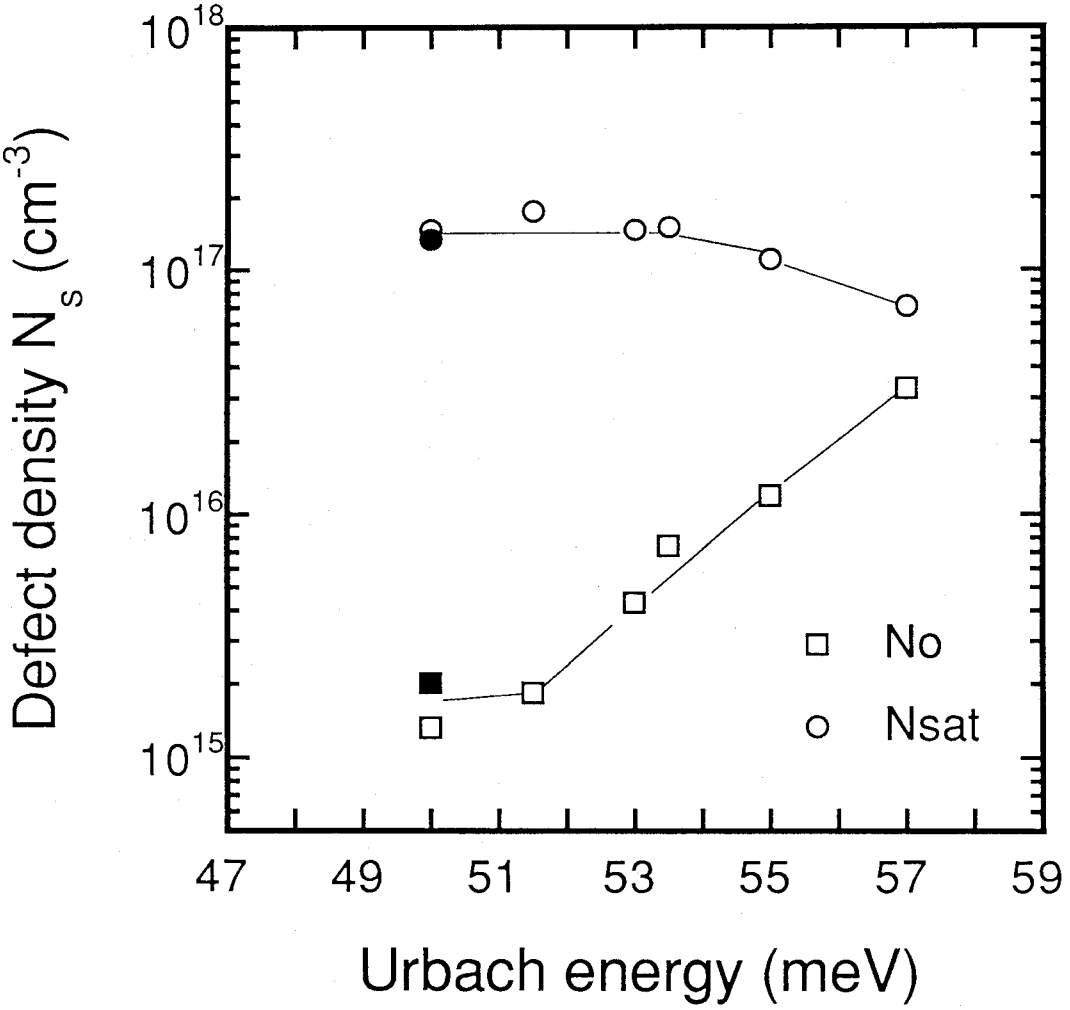

Fig. 2-24 Initial (N_o) and saturated (N_{sat}) defect densities, plotted vs the Urbach energy (E_u) for the samples from the same substrate, annealed at temperatures between 160°C and 310°C. Closed symbols for the initial sample.

are to be sorted out. Careful numerical modeling is indispensable for the evaluation of saturation data on complete cells.

It was shown in the above section that the rate of defect build-up during illumination is related to N_{sat}. These relations allow us to trace out N_S with illumination time. To predict the life time of solar cells from them, numerical device simulation was conducted with a model, which was developed by J.K. Arch [29]. The Poisson equation and the continuity equation for electrons and holes are solved to model the performance of solar cells. Table 2-3 lists the parameters used in the simulation. The defect buildup in the intrinsic layer is traced with the stretched exponential model [14]. Figure 2-25 shows the results of the calculation together with the experimental data of solar cell performance degraded in open circuit. Light-soaking was conducted with a high-intensity laser light (2.2 Wcm^{-2}). The model calculations trace the degradation data well, although V_{oc} and I_{sc} show a little deviation from the calculation results. The results suggest that the lifetime of solar cells can be estimated only by the measurement of N_{sat}. This evaluation method for the intrinsic layer materials will undoubtedly be helpful for studying the stability of solar cells.

In the calculation, the degradation is produced only by changing the defect density in the i-layer. FF is mainly determined by the bulk properties of the i-layer, so the degradation of FF can be fitted well. On the other hand, V_{oc} and I_{sc} are probably affected greatly by interface properties. In particular, carrier recombination in the p/i interface is speculated to reduce them because a large number of photogenerated carriers exist near the p/i interface. A better fitting can be expected by taking the properties of the p-layer and p/i interface into account.

2.5 Summary

The light-induced defect density in a-Si:H can be brought to saturation with only a few hours of intense illumination. Because the saturated defect density depends neither on the light intensity nor on temperatures below 90°C, it is much less sensitive to light-soaking conditions than the intermediate values of the defect density.

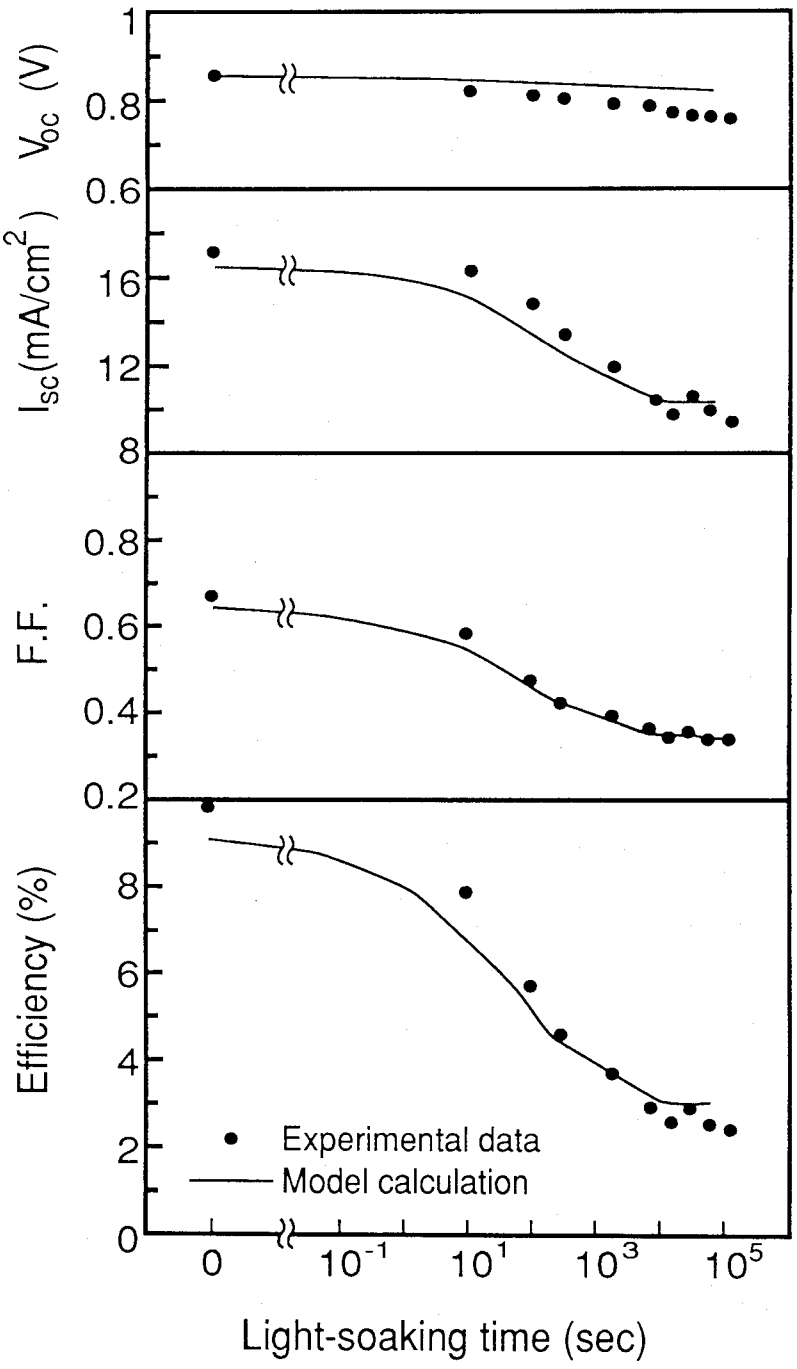

Fig. 2-25 Photovoltaic performance of a-Si:H solar cells as a function of high-intensity ($G=2.2\times10^{22}$ $cm^{-3}s^{-1}$) light-soaking time. Points represent experimental data. The solid line is the modeling results.

Table 2-3 Input parameters for modeling solar cells.

p-layer thickness	(Å)	100
i-layer thickness	(Å)	7000
n-layer thickness	(Å)	200
Electron mobility	($cm^2V^{-1}s^{-1}$)	20
Hole mobility	($cm^2V^{-1}s^{-1}$)	2
Optical gap	(eV)	1.74
Mobility gap	(eV)	1.92
Conduction and valence band effective densities of states	(cm^{-3})	$1x10^{20}$
Normalized valence band tail state density	($cm^{-3}eV^{-1}$)	$6x10^{21}$
Normalized conduction band tail state density	($cm^{-3}eV^{-1}$)	$2x10^{22}$
Characteristic energy of the valence band tail	(meV)	45
Characteristic energy of the conduction band tail	(meV)	27
"Switchover" energy for midgap states	(eV)	0.96
Midgap density of states in the i-layer	($cm^{-3}eV^{-1}$)	$2.8x10^{15} - 6x10^{17}$
Capture cross sections of neutral tail states	(cm^2)	$1x10^{-17}$
Capture cross sections of charged tail states	(cm^2)	$1x10^{-15}$
Capture cross sections of neutral midgap states	(cm^2)	$7.5x10^{-16}$
Capture cross sections of charged midgap states	(cm^2)	$7.5x10^{-15}$

The saturation value is correlated with the growth rate of the defect density. This correlation permits a reconstruction of the entire defect history of a sample of a-Si:H from its saturation value. Therefore, it is a robust criterion for predicting the "usable life" of a-Si:H materials and of solar cells.

The saturated light-induced defect density N_{sat} obtained by high-intensity Kr-ion laser light soaking is insensitive to temperatures below about 90°C. This behavior can be explained within the defect pool model by the limited number of defect sites in the tail states coupled with the concept of defect equilibrium. The results of two calculations for temperature and intensity dependence agree with the experimental data well, and suggest that an assumption in which the convertible defect sites are limited is reasonable.

Experimental data of N_{sat} versus Urbach energy E_u and hydrogen content c_H show that the tail states do not directly affect N_{sat} in device-quality a-Si:H and that c_H is more important for limiting the number of defects than the tail states.

References

1. B.W. Faughnan and R.S. Crandall, Appl. Phys. Lett. **44**, 537 (1984).
2. H. Ohagi, J. Nakata, A. Miyanishi, S. Imao, M. Jeong, J. Shirafuji, K. Fujibayashi and Y. Inuishi: Jpn. J. Appl. Phys. **27** 12 (1988) 2245.
3. M. Ohsawa, T. Hama, T. Akasaka, H. Sakai, S. Ishida and Y. Uchida: J. Non-Cryst. Solids **97&98** (1987) 91.
4. P.V. Santos, W.B. Jackson and R.A. Street: Am. Inst. Phys. Conf. Proc. **234** (1991) 51.
5. M. Stutzmann, J. Nunnenkamp, M.S. Brandt, A. Asano and M.C. Rossi: J. Non-Cryst. Solids **137&138** (1991) 211.
6. L. Yang, L. Chen and A. Catalano: Am. Inst. Phys. Conf. Proc. **234** (1991) 273.
7. H.R. Park, J.Z. Liu and S. Wagner: Appl. Phys. Lett. **55** (1989) 2658.
8. S. Tsuda, T. Takahama, M. Isomura, H. Tarui, Y. Nakashima, Y. Hishikawa, N. Nakamura, T. Matsuoka, H. Nishiwaki, S. Nakano, M. Ohnishi and Y. Kuwano: Jpn. J. Appl. Phys. **26** (1987) 33.
9. M. Vanecek, J. Kocka, J. Stuchlik, Z. Kosicek, O. Stika and A. Triska: Sol. Energy Mater. **8** (1983) 411.
10. Z E. Smith, V. Chu, K. Shepard, S. Aljishi, D. Slobodin, J. Kolodzey, S.Wagner and T.L. Chu: Appl. Phys. Lett. **50** (1987) 1521.
11. N.W. Wang, X. Xu and S. Wagner: Am. Inst. Phys. Conf. Proc. **234** (1991) 186.
12. N. Wyrsch, F. Finger, T.L. MacMahon and M. Vanecek: J. Non-Cryst. Solids **137&138** (1991) 347.
13. M. Brodsky, M. Cardona and J. Cuomo: Phys. Rev. B 16 (1977) 3556.
14. D. Redfield: Appl. Phys. Lett. **52** (1988) 492.
15. M.Stutzmann, W.B.Jackson and C.C.Tsai, Phys. Rev. B **32**, 23 (1985).
16. M. Stutzmann, Phil. Mag. B **60**, 531 (1989).
17. N. Nakamura, T. Takahama, M. Isomura, M. Nishikuni, K. Yoshida, S. Tsuda, S. Nakano, M. Ohnishi and Y. Kuwano: Jpn. J. Appl. Phys. **28** (1989) 1762.
18. N.Hata, S.Wagner, P.Roca i Cabarrocas and M.Favre: Appl. Phys. Lett. **56** (1990) 2448.

19. Z E. Smith and S. Wagner: *Amorphous Silicon and Related Materials*, ed. H. Fritzsche (World Scientific, Singapore, 1989) Advances in Disordered Semiconductors Vol.1, p.409.
20. N. Hata and S. Wagner: J. Appl. Phys. **72** (1992) 2857 .
21. Y.Bar-Yam, D. Adler and J.D. Joannopoulos: Phys. Rev. Lett. **57** (1986) 467.
22. Z E. Smith, S. Aljihi, D. Slobodin, V. Chu, S. Wagner, P.L. Lenahan, A.R. Arya and M.S. Bennett: Phys. Rev. Lett. **57** (1986) 2450.
23. R.A. Street, J. Kakalios and T.M. Hayes: Phys. Rev. B **34** (1986) 3030.
24. Z E. Smith and S. Wagner: Phys. Rev. Lett. **59** (1987) 688.
25. G. Schumm and G.H. Bauer: *Proc. 22nd IEEE Photovoltaic Specialists Conf., Las Vegas, Nevada, USA, 1991* (IEEE, New York, NY, 1991) p.1225.
26. J.G. Simmons and G.W. Taylor: Phys. Rev. B **4** (1971) 502.
27. R.H. Bube and D. Redfield: Appl. Phys. Lett. **57** (1990) 79.
28. D. Redfield and R.H. Bube: *Proc. 22nd IEEE Photovoltaic Specialists Conf., Las Vegas, Nevada, USA, 1991* (IEEE, New York, NY, 1991) p.1507.
29. J.K. Arch, F.A. Rubinelli, J.Y. Hou and S.J. Fonash: J. Appl. Phys. **69** (1991) 7057.

3 Light-induced degradation of the window p-layer

3.1 Background and motivation

Open circuit voltage (V_{oc}) is one of the most important factors in determining the performance of hydrogenated amorphous silicon (a-Si:H) solar cells. It depends primarily on the built-in potential within the pin junction [1], and therefore, wider bandgap materials usually have the ability to produce a higher V_{oc}. However, because wider bandgap materials show less optical absorption of solar light and thus cause a reduction in the short circuit current (I_{sc}), they are not suitable for use in the active layer (i-layer) of high-efficiency single-junction cells. Therefore, attention has been paid to doped layers and much effort has been made to attain higher conductivity and a wider bandgap in a window layer, using materials such as amorphous silicon-carbide (a-SiC) [2] and microcrystalline silicon [3]. The wide bandgap and high conductivity (low activation energy) result in a high built-in potential, allow more light to reach the i-layer and yield improvements in V_{oc} and I_{sc}. Since the a-SiC window layer was reported [2], several techniques have been developed to further improve a-SiC, such as high photosensitivity obtained by the hydrogen-diluted plasma method[4], effective doping of a-SiC with $B(CH_3)_3$ [5] and high-conductivity microcrystalline SiC [6].

Figure 3-1 shows the band profile of an a-Si:H solar cell and the motion of photoinduced excess carriers in the i-layer. V_{oc} is not determined only by the built-in potential but also by other factors such as the carrier recombination through defect sites [7]. In particular, the recombination near the p/i interface is probably significant, because the a-SiC p-layer has a high defect density compared with the i-layer, and thus photoinduced carriers generated at a high rate in this region easily recombine through the defects. Therefore, decreasing the recombination of excess carriers is another important concern for obtaining a high V_{oc}, and efforts have been made to do this by decreasing the defect density in the p-layer itself and by placing a buffer layer with a low defect density between the p- and i-layers [8]. In consideration of the characteristics of the p-layer, acceptor concentration is a significant factor. It determines the position of the quasi-Fermi level

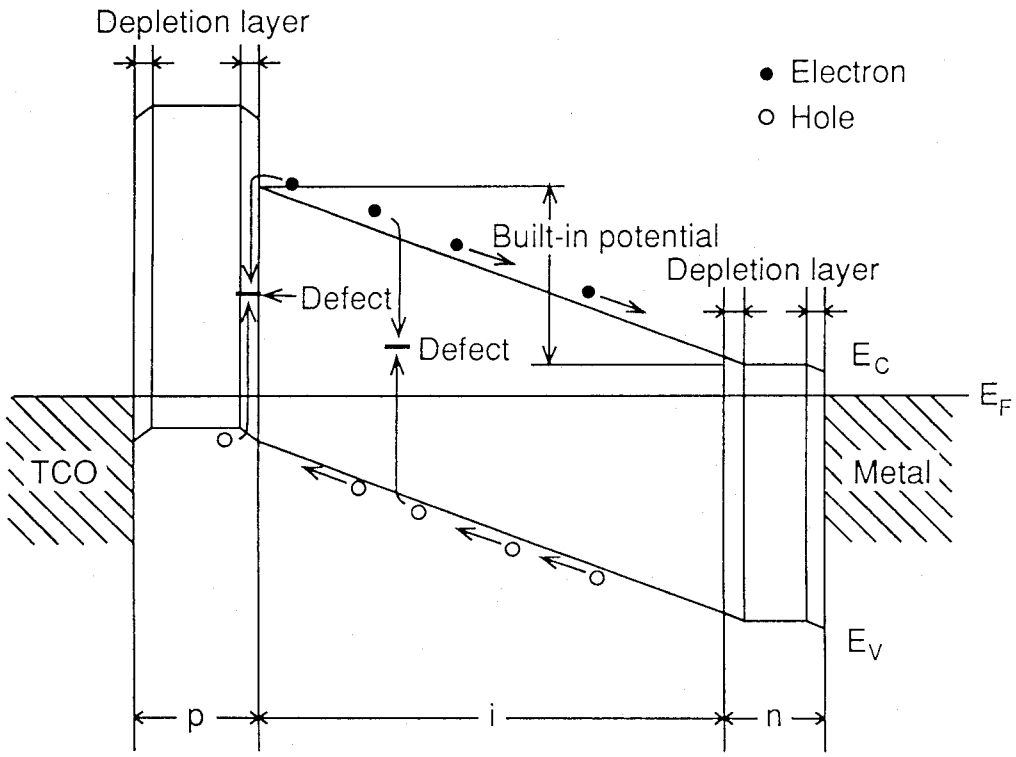

Fig. 3-1 Band profile of an a-Si:H solar cell and the motion of photoinduced excess carriers in the i-layer.

and corresponds to the space charge density in the p-layer. Both factors have a significant influence on the built-in potential. The difference in the the quasi-Fermi levels between the p- and n-layers basically produces the built-in potential, as shown in Fig 3-1. When the p-layer is too thin, however, the built-in potential is lower than the value that an enough thick p-layer produces, because the depletion layers at the interfaces with the TCO and i-layer spread to the entire p-layer thickness. In other words, a p-layer with a lower doping concentration has wider depletion layers because of the lower density of its acceptors, and should be thicker to obtain the highest possible built-in potential. In this sense, a high-doped p-layer seems to be suitable for use in a solar cell. However, because boron doping usually produces doping-induced defects [9], it is not easy to find the best conditions.

Light-induced degradation of V_{oc} is sometimes observed, but sometimes not. As described above, V_{oc} has a close relation with the p-layer properties. Hence, the light-induced effect in the p-layer must influence V_{oc}. But the V_{oc} degradation is not usually very large compared with the degradation of the fill factor (FF), which is a main cause of the degradation of a-Si solar cells [10,11]. Therefore, there have not been many reports on the V_{oc} degradation, and in particular, the defference in the degradation rates among several solar cells has not been investigated. Hence, the details of V_{oc} degradation are still unknown. This phenomenon is, however, very important for understanding the V_{oc} of a-Si solar cells, and a reduction in V_{oc} degradation is necessary to achieve stable operation. In this Chapter, the correlation between V_{oc} degradation and the light-induced effect in the p-layer material is studied to reveal the mechanism of the degradation and to attain a way to suppress it. The dependence of V_{oc} on the p-layer properties is investigated to understand the mechanism determing V_{oc} in Section 3.2, and the correlation between the light-induced effect in the p-layer and the V_{oc} degradation is discussed in Section 3.3.

3.2 Dependence of open circuit voltage on the p-layer

3.2.1 Experimental techniques

A-Si:H solar cells have a TCO/p:a-SiC/i:a-Si/n:a-Si/metal structure and p-, i- and n-layers were prepared from 13.56 MHz glow discharge in a separated ultra-high vacuum chamber system (the super chamber) [12]. The TCO layer was SnO_2 coated ITO with a flat surface. In the fabrication of the p-layer of the solar cells, SiH_4, C_2H_2 and $B(CH_3)_3$ were used as source gases. For obtaining the a-SiC:H film properties in regard to boron concentration, B_2H_6 was used as a doping gas to avoid the effect of carbon concentration caused by doping with $B(CH_3)_3$. The characteristics of the solar cells were measured under AM-1.5, 100 mW/cm^2 illumination at room temperature (~25°C). For an accelerated test of the light-induced degradation, light-soaking of 500 mW/cm^2 was conducted using a tungsten lamp with an infrared cut filter.

The built-in potential was monitored by measuring the response current to chopped monochromatic light (λ=550nm) [13]. The response current was measured while increasing the voltage applied to the solar cells under bias light of AM-1.5, 100 mW/cm^2, and the voltage was checked when the direction of the response current was changed to the same direction as the applied voltage, as shown in Fig. 3-2. This voltage, denoted as V_t, makes the electric field within the solar cells zero and corresponds to the built-in potential. The electric field, however, is not uniform, so the response current is changed by the wavelength of the chopped monochromatic light from the differences in penetration depth [14], and it may be affected also by the interface properties between the p- and i-layer. Therefore, the turning point of the response current may not exactly show the built-in potential, but is still a useful method for obtaining the relative change in the built-in potential. This method was adopted to evaluate the built-in potential.

3.2.2 Thickness and boron-doping of the p-layer

Two different doping concentrations in the p-layer were tested to obtain data on the thickness dependence. The properties of the a-SiC:H used for the p-layer in the experiments are shown in Table 3-1. Figure 3-3 shows the experimental results of the thickness dependence of

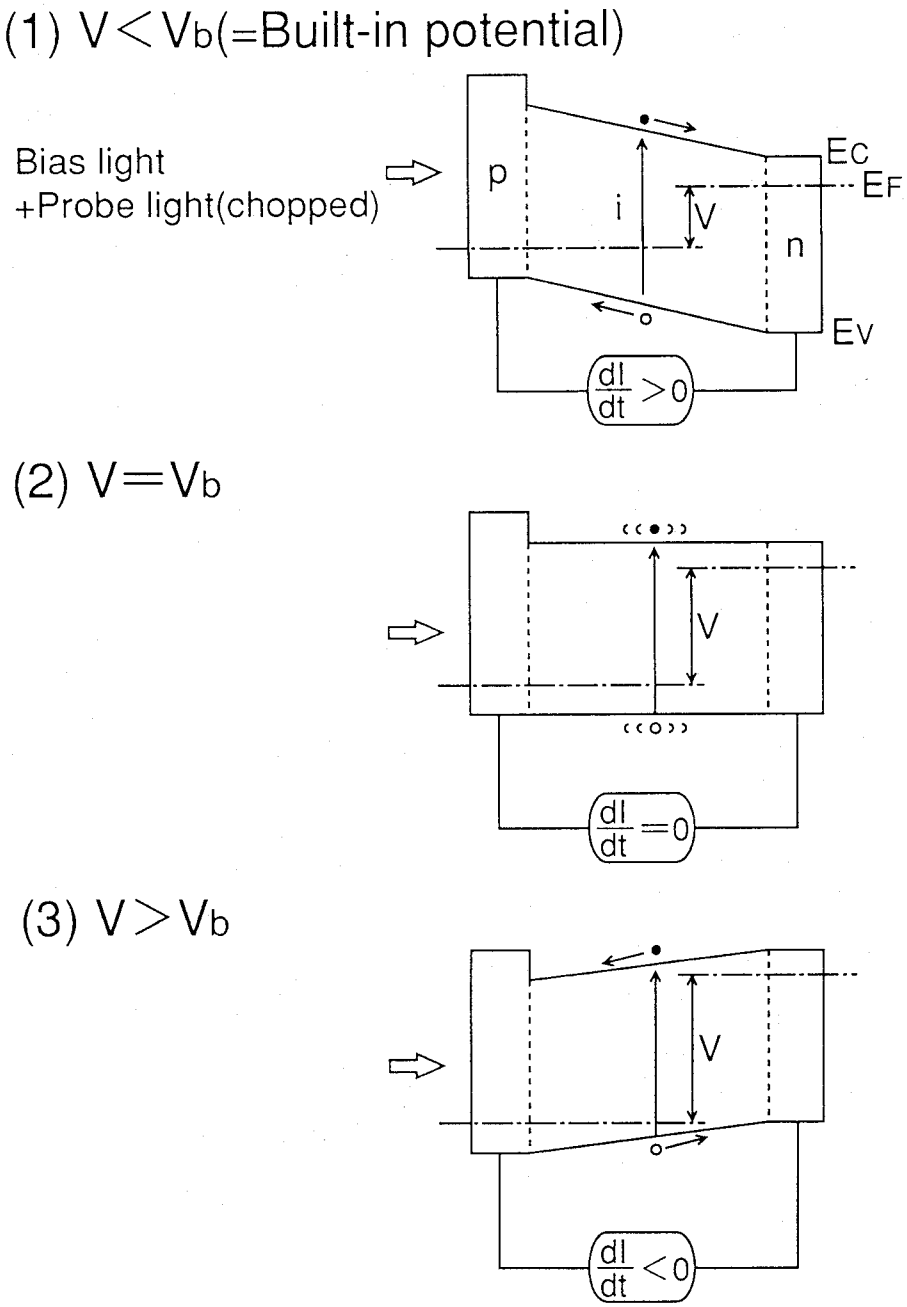

Fig. 3-2 Procedure to determine the built-in potential by measuring the response current to chopped monochromatic light.

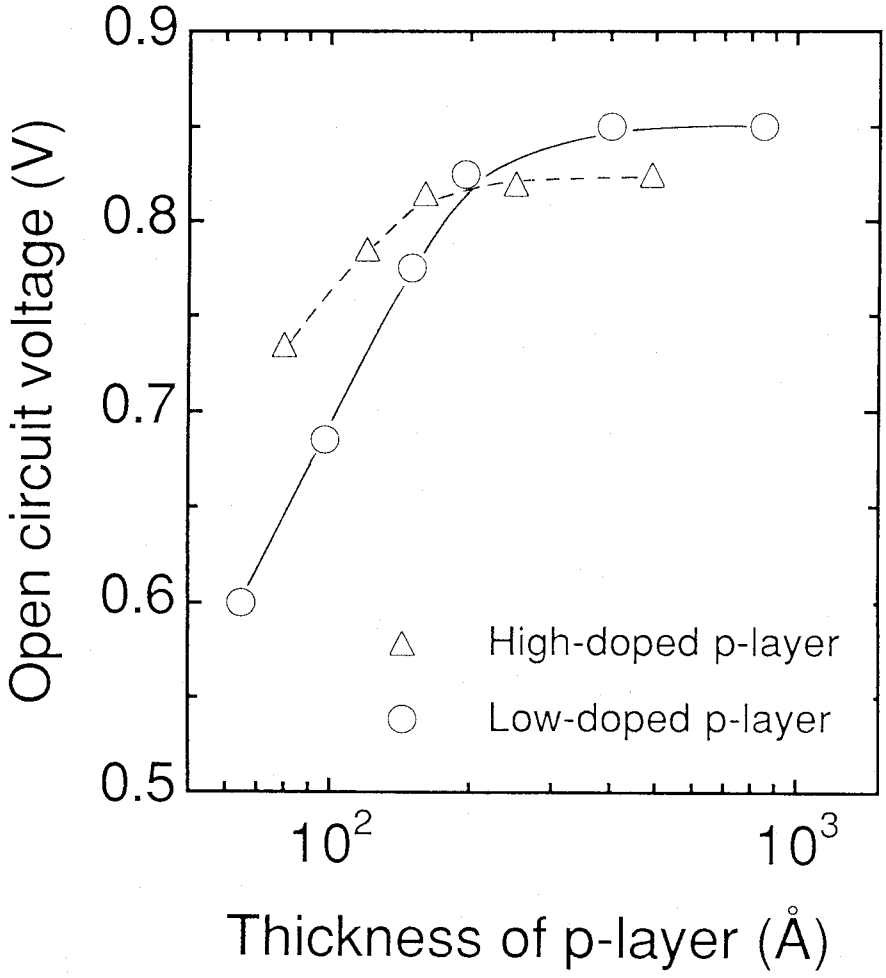

Fig. 3-3 Open-circuit voltage of solar cells with a low-doped p-layer and a high-doped p-layer as a function of p-layer thickness.

V_{oc}. When the p-layer is relatively thin (<200Å), the V_{oc}s of both p-layers increase with increasing p-layer thickness. The V_{oc}s of the high-doped p-layer ($B(CH_3)_3/SiH_4$=3.5%) are higher than those of the low-doped p-layer ($B(CH_3)_3/SiH_4$=0.45%), but the V_{oc}s of the low-doped p-layer increase more rapidly. At around 200Å the V_{oc}s of the low-doped p-layer catch up with those of the high-doped p-layer and then surpass them. In the thicker p-layer region (>300Å), the V_{oc}s of both the high-doped and low-doped p-layers saturate at 0.825V and 0.850V, respectively. It should be noted that the low-doped p-layer causes a lower V_{oc} than the high-doped p-layer when the p-layer is relatively thin, but can cause a higher V_{oc} when the p-layer is sufficiently thick. On the other hand, the voltage of the turning point of the response current for the chopped monochromatic light (V_t), which corresponds to the built-in potential, also increases with increasing p-layer thickness and begins to saturate (>500Å) as shown in Fig. 3-4. The V_ts of the high-doped p-layer are always higher than those of the low-doped p-layer, and the difference in V_t is about 0.1V, nearly equal to the difference in activation energy of both p-layers. This shows that the V_t represents the built-in potential.

Table 3-1 Properties of a-SiC:H used in the p-layer.

$B(CH_3)_3/SiH_4$	$\sigma_d(\Omega cm)^{-1}$	$\sigma_{ph}(\Omega cm)^{-1}$	Tauc Gap(eV)	B-value	$\alpha_{2100}/\alpha_{2000}$	c_H(%)	ΔE(eV)
0.035	$4\text{-}6\times10^{-8}$	$1\text{-}2\times10^{-7}$	1.96	760	6.6	25	0.54
0.0045	$0.4\text{-}1\times10^{-8}$	$3\text{-}4\times10^{-7}$	1.97	790	5.3	25	0.64

σ_d, σ_{ph}: dark and photoconductivity.

$\alpha_{2100}/\alpha_{2000}$, c_H: ratio of absorption coefficient at 2100 cm^{-1} to that at 2000 cm^{-1}, and hydrogen content measured by IR absorption.

ΔE: activation energy of dark conductivity.

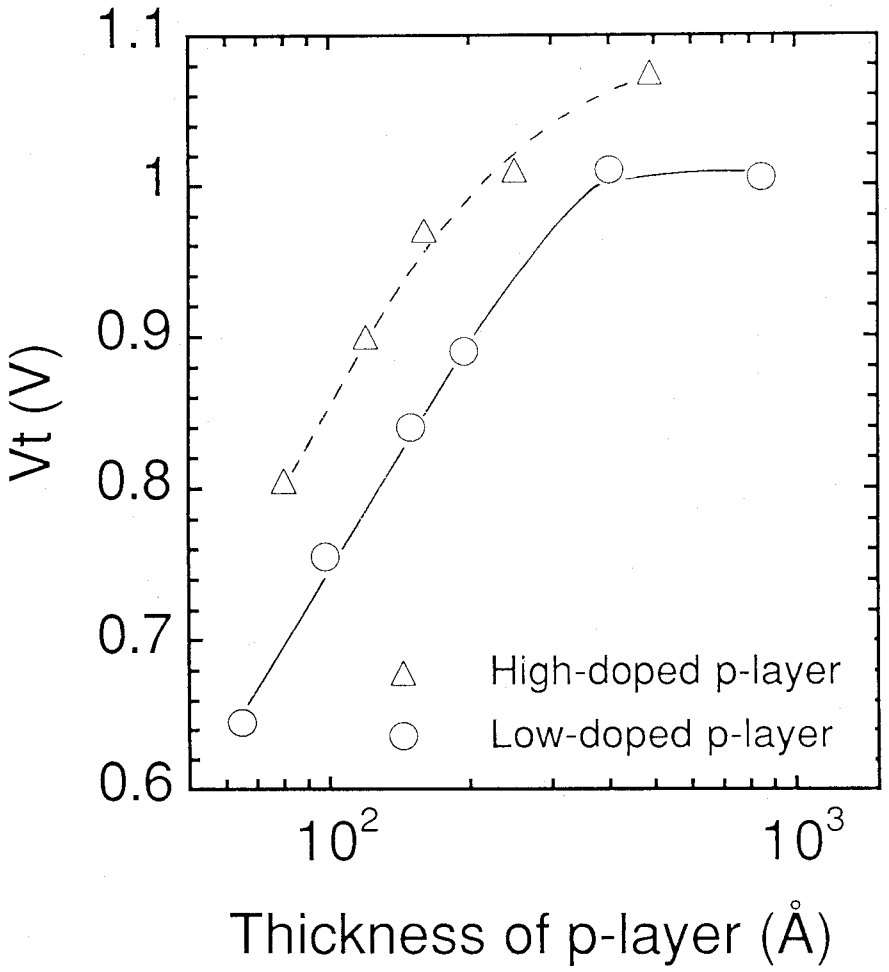

Fig. 3-4 The turning point of the response current for chopped light (V_t), for solar cells with a low-doped p-layer and a high-doped p-layer as a function of p-layer thickness.

The different tendencies of the V_{oc} and V_t data indicate that the high built-in potential of the high-doped p-layer does not effectively contribute to V_{oc}. The low-doped p-layer has a lower acceptor concentration and a larger activation energy, so a lower V_{oc} should be observed in the solar cells with a smaller built-in potential. However, the V_{oc}s of the low-doped p-layer are higher than those of the high-doped p-layer when the p-layer is sufficiently thick. V_{oc} does not always reflect the higher built-in potential caused by the high-doped p-layer. This suggests that a high-doped p-layer may cause more current leakage due to carrier recombination affecting V_{oc}, probably because of a high defect density.

On the other hand, when the p-layer is relatively thin, the V_{oc}s of the low-doped p-layer are lower than those of the high-doped p-layer. In this case, the shortage of space charge corresponding to the acceptor concentration is thought to influence V_{oc} more than the carrier recombination. Acceptor concentration dominates the quasi-Fermi level, which is the cause of the built-in potential. The acceptor concentration also affects the width of depletion layers at the TCO/p and p/i interfaces. The depletion layers decrease the effective p-layer thickness Therefore, the p-layer cannot keep its original properties without sufficient thickness [7,15]. The low-doped p-layer has higher activation energy and wider depletion layers because of the lower acceptor concentration. The large drop in the V_{oc}s of the thin low-doped p-layer, which is seen in Fig. 3-3, is probably caused by the wider depletion layer.

3.2.3 Doping-induced defects in a-SiC:H

Midgap defects induced by substitutional doping have been observed in several experiments [9]. Electronic models have shown that boron atoms in a silicon network break silicon bonds and cause dangling bonds [16]. The defect densities of a-SiC:H films with several boron doping ratios were measured by photothermal deflection spectroscopy (PDS) [17]. Figure 3-5 shows the results of the PDS measurements of undoped and two different doped samples. The absorption coefficient of the shoulder in the long wavelength region corresponding to the midgap defect density increases with an increasing boron doping ratio. The neutral dangling bond density

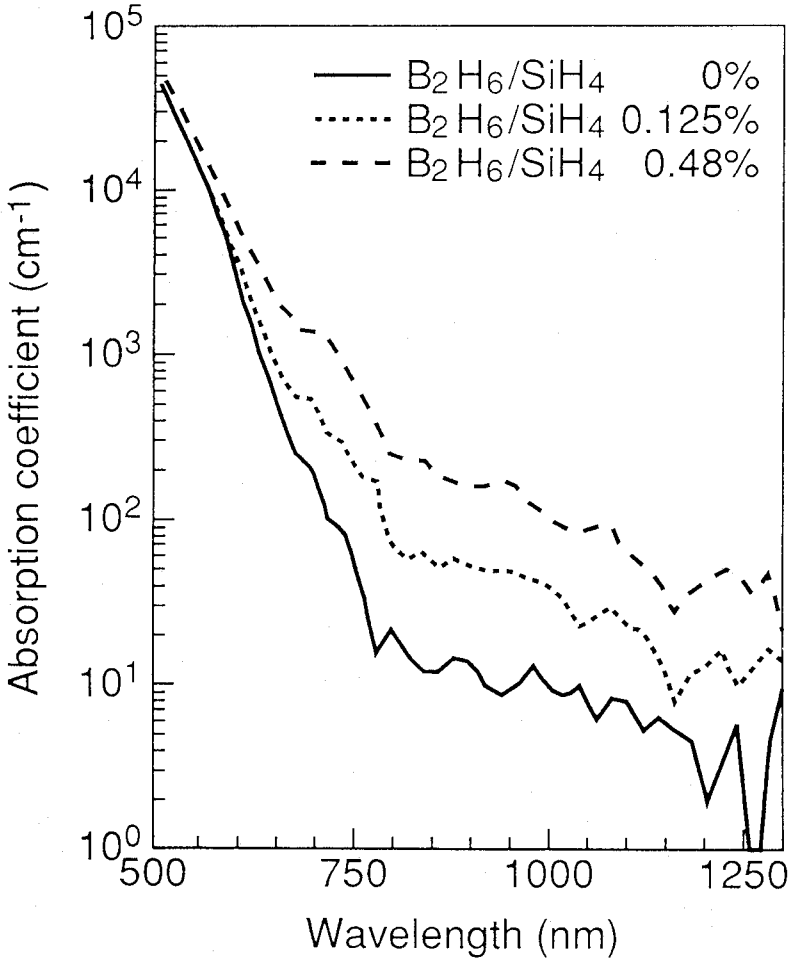

Fig. 3-5 Absorption coefficient of undoped and boron doped a-SiC:H films measured by the photothermal deflection spectroscopy.

of the undoped sample obtained in the ESR measurement is $2x10^{17}$ cm^{-3}. The defect densities of the two doped samples are roughly estimated by the parallel shift of the PDS spectra from the spectrum of the undoped sample, because their charged dangling bonds are not detectable using the ESR method. The estimated values are $8x10^{17}$ cm^{-3} and $3x10^{18}$ cm^{-3} for 0.125% and 0.48% B_2H_6 doping ratios, respectively. These increases in the defect densities must result in carrier recombination near the p/i interface, which cause the reduction in the V_{oc}s of the high-doped p-layer. The device simulation model proposed by Yamanaka et al [7] shows that the increase in defect density near the p/i interface decreases the V_{oc}, especially in the region from 10^{17} to 10^{19} cm^{-3}. This is consistent with the experimental results.

3.2.4 Open-circuit voltage versus built-in potential

How built-in potential relates to V_{oc} is of great interest for an understanding of the Voc mechanism [1]. The V_{oc}s of several samples are plotted against their V_t values in Fig. 3-6. In the lower V_t region, V_{oc} has a linear correlation with V_t and the built-in potential probably contributes directly to V_{oc}. However, in the higher V_t region (>0.80V), the V_{oc} values deviate from the line and seem to be limited by factors other than V_t. The V_{oc}s of the high-doped p-layer solar cells deviate from the line at about 0.80V of V_t and gradually increase to 0.825V. The V_{oc}s of the low-doped ones deviate at a higher V_t (~0.90V) and reach 0.85V. The V_{oc} seems to be limited by the doping concentration of the p-layers; the doping-induced defects must cause carrier recombination near the i-layer, as discussed above. To observe the effect of the doping-induced defects near the p/i interface on V_{oc}, the low-doped p-layer was placed between the high-doped p-layer and the i-layer as a buffer layer. The V_{oc}s of these cells reach 0.875V, which is about 0.05V higher than the original V_{oc} values of the high-doped p-layer cells at the same V_t. Moreover, the V_{oc}s of the solar cells with an undoped a-SiC:H buffer layer reach 0.90V. The reduction in the number of doping-induced defects near the p/i interface results in a higher V_{oc} from the same built-in potential. In the data plots of Fig. 3-6, the V_{oc} limitation can be seen to be correlated with the doping concentration near the p/i interface in the high-V_t region. It is evident that the defect density

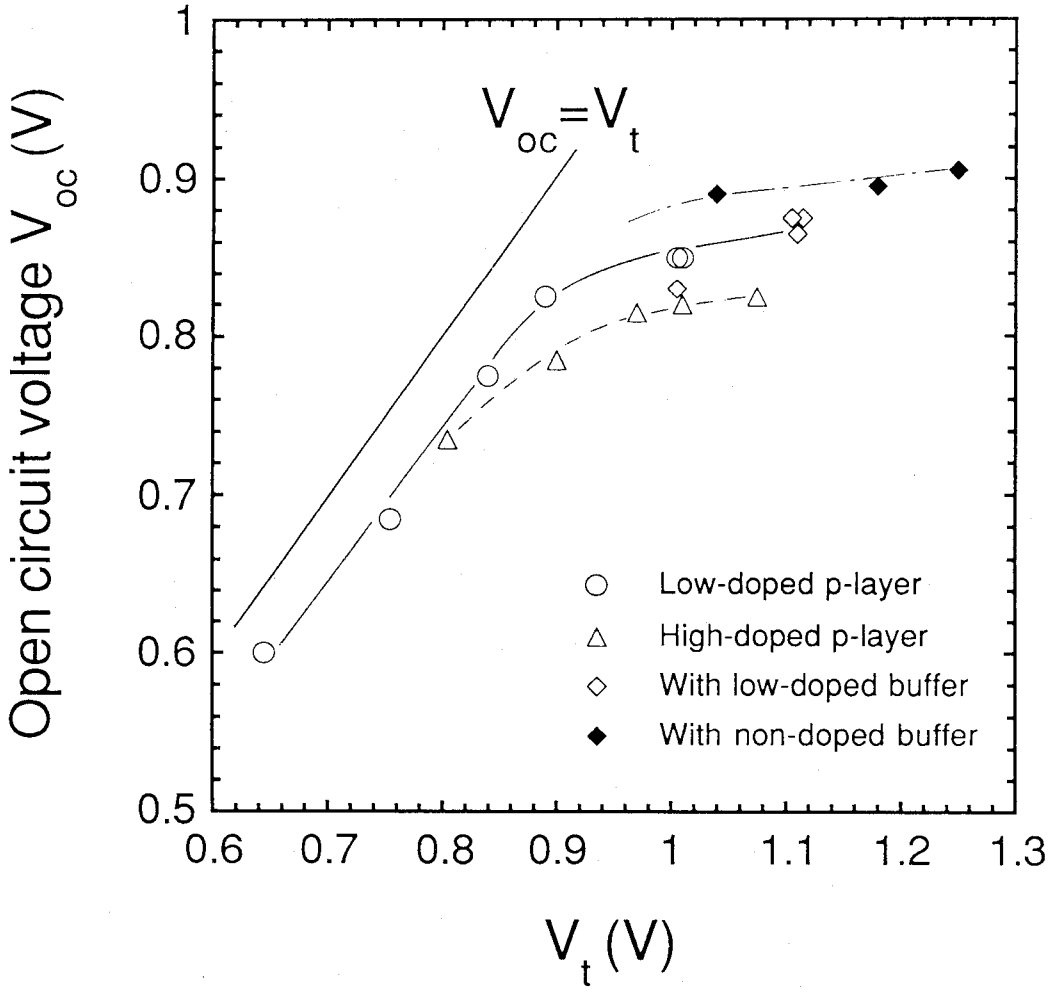

Fig. 3-6 Open circuit voltage versus turning point of the response current for chopped light (V_t) in solar cells with several kinds of p-layers.

near the p/i interface must be reduced in order to obtain a higher V_{oc} as well as a high built-in potential.

3.3 Light-induced effect in the p-layer

3.3.1 Light-induced defects in a-SiC:H

A-SiC:H is also expected to have a light-induced effect similar to that of a-Si:H. If so, it may affect solar cell performance. To pursue this question, measurements of the light-induced defect density were conducted. After light-soaking (500 mW/cm^2, 5 h), an undoped a-SiC:H film shows about 3/2 times larger absorption for long wavelength light in the PDS measurements, as shown in Fig. 3-7. The ESR measurement of the light-soaked film gives a value of $3x10^{17}$ cm^{-3}, which is 3/2 of the initial value, and this is consistent with the PDS result. For doped films, no significant change can be observed in the PDS measurements after the light-soaking. The increase in the midgap absorption due to the light-soaking is smaller than the initial values in the doped films. Therefore, it is difficult to see changes in the PDS spectra, especially in the high-doped sample even if the doped films show the same degradation. Here it can at least be said that it is possible for the defect densities of the doped films to increase by $1x10^{17}$ cm^{-3} with the light-soaking. The V_{oc} of the low-doped p-layer cells is probably influenced by the light-induced defects, because the light-induced defects are not small compared with the initial defect density in the low-doped p-layer: $8x10^{17}$ cm^{-3}.

3.3.2 Influence on the quasi-Fermi level position

Acceptor concentration dominates the properties of the p-layer. Free holes from the acceptors determine the quasi-Fermi level of the p-layer and the built-in potential within the pin junction. The position of the quasi-Fermi level is reflected by the activation energy of dark conductivity. The acceptor concentration influences the width of the depletion layers at the TCO/p and p/i interfaces, which decrease the effective p-layer thickness [7,15]. Therefore, the acceptor concentration is one of the most important factors for determining V_{oc}. In this sense, the higher

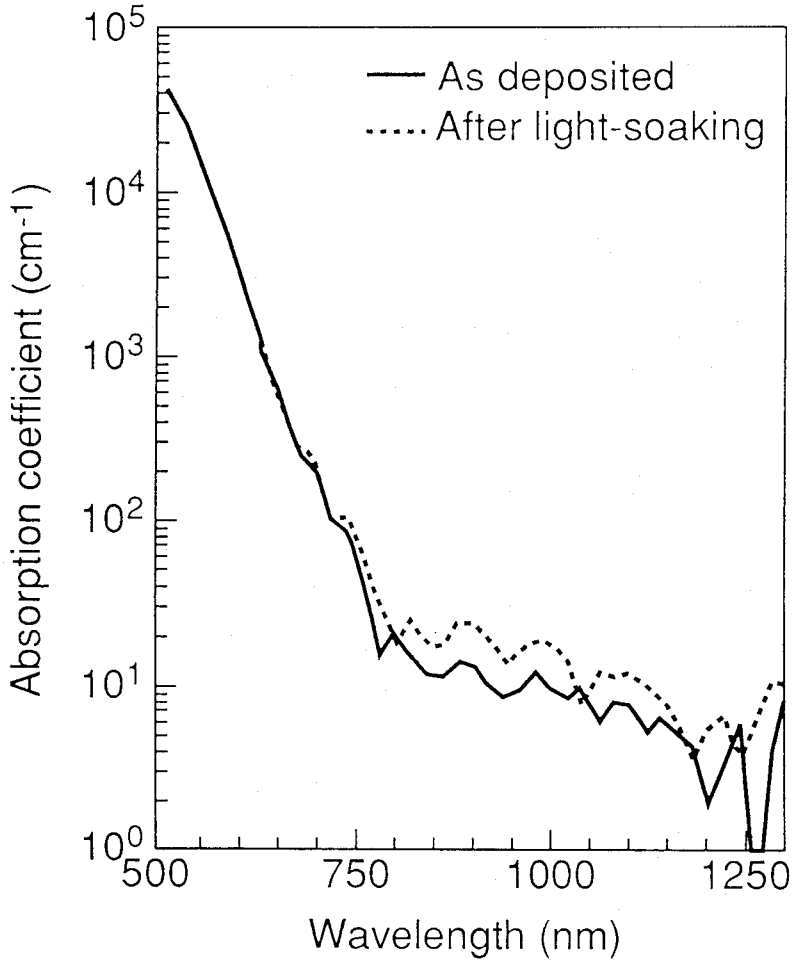

Fig. 3-7 Change in absorption coefficient of an undoped a-SiC:H film with light-soaking (500 mWcm^{-2}, 5 h), as measured by the photothermal deflection spectroscopy.

acceptor concentration created by high boron doping is preferable, although the doping-induced defects are troublesome as discussed above.

With respect to the light-induced degradation of V_{oc}, the effect of the light-induced defects on the acceptor concentration is of great interest. If the light-induced defects compensate the acceptors in the p-layer, the number of effective acceptors decreases and thus the activation energy of the dark conductivity becomes higher. In Fig. 3-8, the activation energies of doped a-SiC:H films before and after light-soaking are shown as a function of the doping ratio. It is observed that the low-doped films show a larger increase in the activation energy caused by the illumination. As expected, the low-doped films are influenced much more by the compensation via the light-induced defects than the high-doped films. The concentration of the effective dopants in p-type a-Si:H doped at the same gas-phase ratio as in the low-doped film (0.125%) is estimated to be around 10^{17} cm^{-3} in earlier works [18,19]. If a-SiC:H films have the same doping efficiency, light-induced defects of $1x10^{17}$ cm^{-3} can affect the acceptor concentration of the low-doped p-layer. Actually the dark conductivity of this film decreases by one order after light-soaking: approximately from 10^{-7} to 10^{-8} $(\Omega cm)^{-1}$. On the other hand, the activation energies of the high-doped films do not change with the light-soaking. The high-doped films (>0.5%) show a dark conductivity of more than 10^{-6} $(\Omega cm)^{-1}$ and the acceptor concentration can be expected to be more than 10^{18} cm^{-3} [18,19]. Therefore, the light-induced defects can no longer affect the acceptor concentration and the dark conductivity does not change due to the light-soaking. Therefore, the V_{oc}s of the low-doped p-layer solar cells are expected to show the V_{oc} degradation due to the increase in the activation energy and the width of the depletion layers in p-layers.

3.3.3 Degradation of the open circuit voltage

The degradation of V_{oc} is measured using the same samples as in the above section. In Figs. 3-9 and 3-10, the V_{oc}s of the high-doped and low-doped p-layers, respectively, after light-soaking (500 mW/cm^2, 5 h) are plotted with the initial V_{oc} values as a function of p-layer thickness. The high-doped p-layer shows little degradation for any thickness, as shown in Fig.

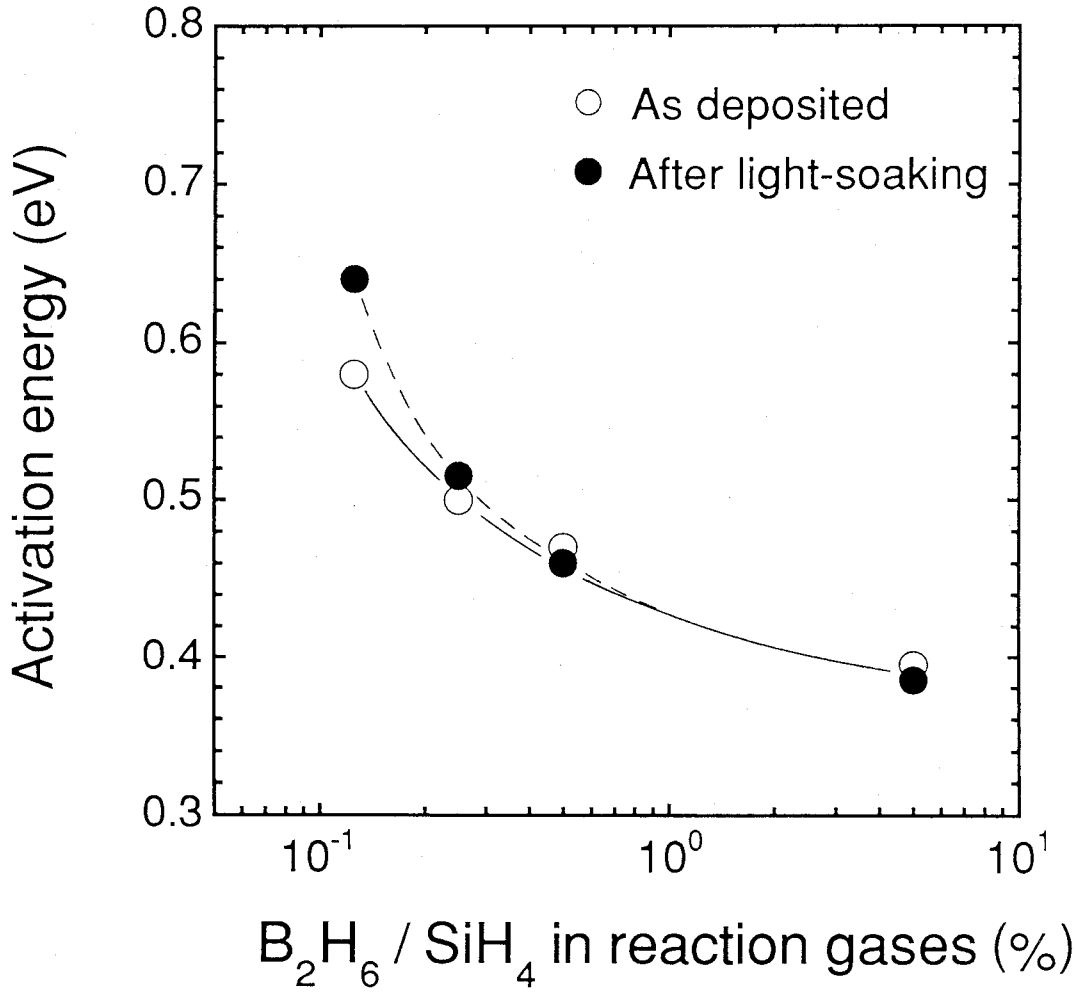

Fig. 3-8 Activation energy of a-SiC:H films before and after light-soaking (500 mWcm^{-2}, 5 h), as a function of boron doping ratio.

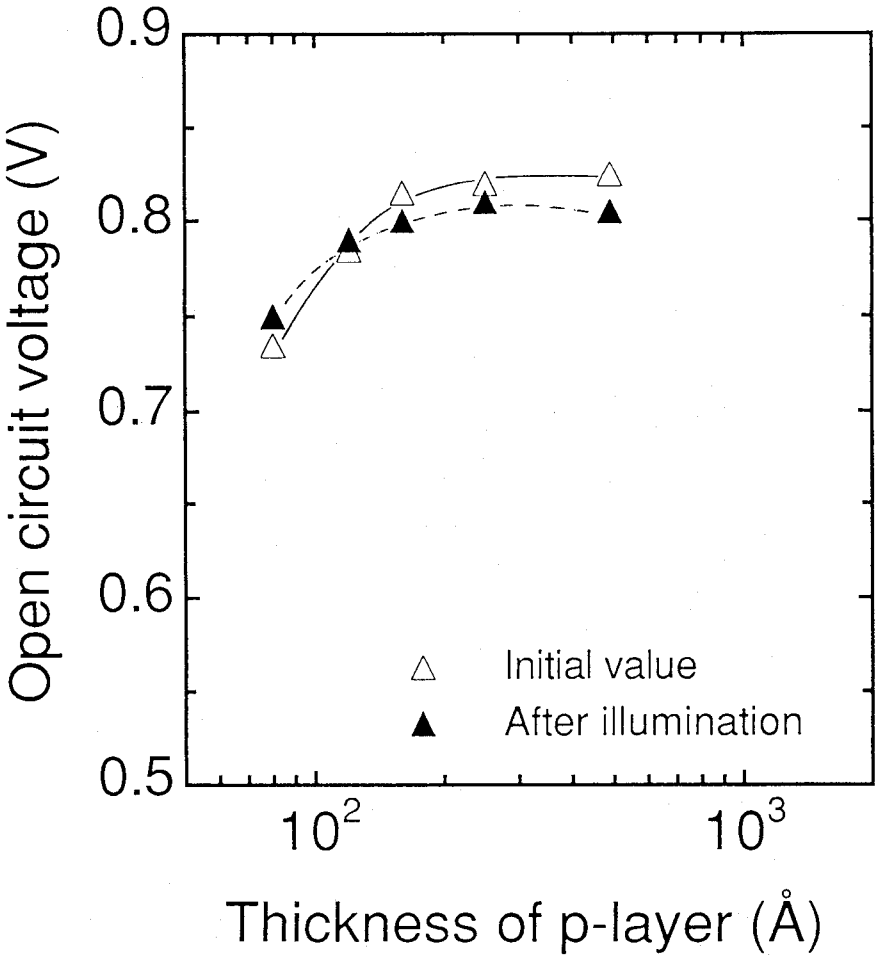

Fig. 3-9 Degradation of open circuit voltage in the solar cells of a high-doped p-layer after light-soaking (500 mWcm^{-2}, 5 h), as a function of p-layer thickness.

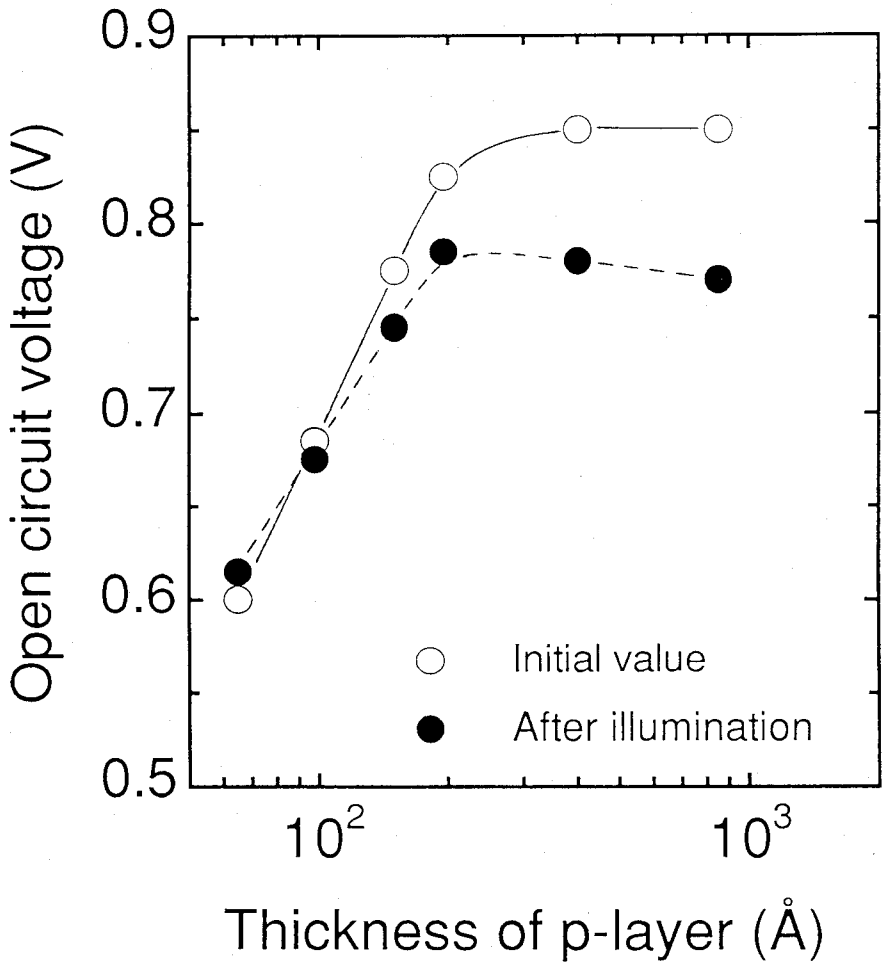

Fig. 3-10 Degradation of open circuit voltage in the solar cells of a low-doped p-layer after light-soaking (500 mWcm^{-2}, 5 h), as a function of p-layer thickness.

3-9. On the other hand, in Fig. 3-10, the low-doped p-layer shows much degradation especially in the thicker p-layer region. As a result, the V_{oc}s of the low-doped p-layer are lower than those of the high-doped p-layer in the entire thickness range after the light-soaking. The time dependence of the V_{oc} degradation was also measured for the two doped p-layers, as shown in Fig. 3-11. The thickness of the p-layers for both of the solar cells is relatively thick (400Å-500Å) to clarify the difference. The V_{oc}s of the high-doped p-layer show a small degradation rate from 0.830V to 0.800V after 40 hours of illumination. On the other hand, the V_{oc}s of the low-doped p-layer show fast degradation, decreasing from 0.85V to 0.735V within the same illumination period. The high-doped p-layer seems to maintain its properties after the light-soaking. The high-doped p-layer already has a high defect density before the light-soaking, and the light-induced defect density is relatively small compared with the initial defect density, so it is probable that the light-induced defects do not heavily influence the film properties corresponding to V_{oc}. By contrast, the light-induced defects produced in the low-doped p-layer deteriorate the high initial V_{oc}s. The low-doped p-layer initially has a relatively low defect density, so the light-induced defects cannot be ignored in the determination of the film properties. Besides, it is possible that the light-induced defects compensate the acceptors in the low-doped p-layer. This reduction in the acceptor concentration decreases the built-in potential and causes a significant reduction in V_{oc} compared with the high-doped p-layer. In the thin p-layer region (<100Å) no degradation of the low-doped p-layer cells is observed although the initial V_{oc}s are very low. In this case, the TCO (SnO_2) under the p-layer probably determines the electrical properties of the solar cells more than the p-layer because the number of acceptors in such a thin low-doped p-layer is too small to maintain sufficient properties of bulk, so the degradation of the p-layer does not cause a significant change in V_{oc}.

This behavior of V_{oc} degradation is consistent with observations of the material properties of a-SiC:H. It suggests that the p-layer can be designed to offer a stable V_{oc} with the correlation obtained in this Chapter, and this guiding principle gives us a great advantage in the design of stable solar cells.

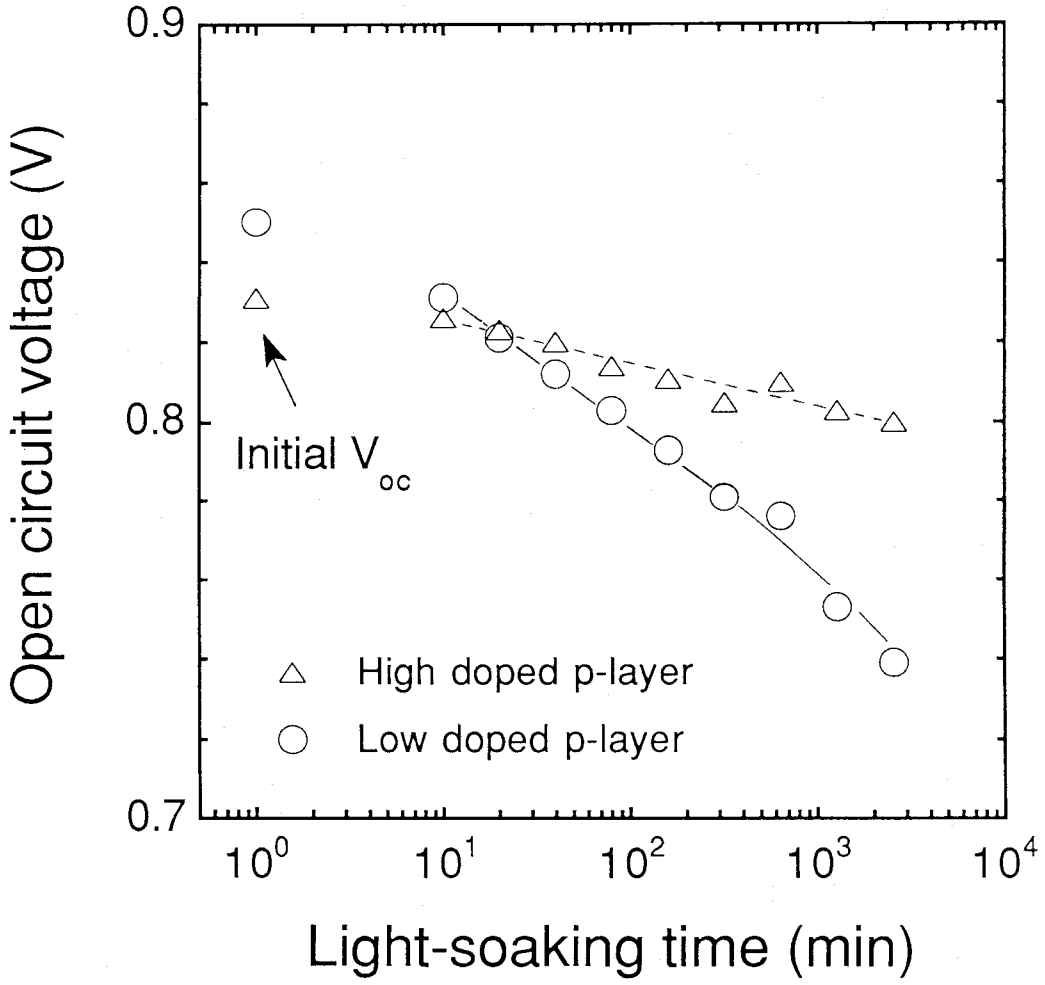

Fig.3-11 Open circuit voltage of solar cells with a low-doped p-layer and a high-doped p-layer as a function of light-soaking time of 500 $mWcm^{-2}$.

3.5 Summary

Experimental data of V_{oc} were analyzed in regard to the thickness and doping concentration of the p-layer. A high-doped p-layer results in a higher built-in potential because of its low activation energy, but its high defect density causes the recombination of excess carriers and imposes a limitation on V_{oc}. On the other hand, a low-doped p-layer results in a lower built-in potential. With insufficient p-layer thickness, lower V_{oc}s are observed due to the low acceptor concentration, but a higher V_{oc} can be obtained with sufficient thickness because of the low defect density. It is concluded that the midgap defect density of the p-layer near the p/i interface induced by the doping causes the V_{oc} limitation and it is necessary to simultaneously attain both high built-in potential and low defect density near the p/i interface in order to obtain a higher V_{oc}.

Light-induced degradation of V_{oc} occurs to a much greater extent in low-doped p-layer cells than in high-doped p-layer cells. The light-induced defect density in the low-doped p-layer is not negligible compared with the initial defect density, so the light-induced defects cause an increase in carrier recombination near the p/i interface. The low concentration of acceptors, which can be partially compensated by the light-induced defects, results in the shortage of acceptors, causing a reduction in the built-in potential. The high-doped p-layer initially has a relatively high defect density and acceptor concentration; thus, the light-induced defects do not affect the properties of the p-layer as much, and little degradation of V_{oc} occurs.

References

1. S. Nonomura, H. Okamoto and Y. Hamakawa: Appl. Phys. A **32** (1983) 101.
2. Y. Tawada, M. Kondo, H. Okamoto and Y. Hamakawa: Sol. Energy Mater. **6** (1982) 299.
3. H. Haruki, Y. Uchida, H. Sata, M. Nishimura and M. Komiyama: *Proc. 13th Conf. Solid State Devices*, Tokyo, 1981, p.53.
4. A. Matsuda and K. Tanaka: J. Non-Cryst. Solid **97&98** (1987) 1367.
5. H. Tarui, T. Matsuyama, S. Okamoto, H. Dohjoh, Y. Hishikawa, N. Nakamura, S. Tsuda, S. Nakano, M. Ohnishi and Y. Kuwano: Jpn. J. Appl. Phys. **28** (1989) 2436.
6. Y. Hattori, D. Krungam, T. Toyama, H. Okamoto and Y. Hamakawa: Appl. Surf. Sci. **33/34** (1988) 1276.
7. S. Yamanaka, M. Konagai and K. Takahashi: Jpn. J. Appl. Phys. **28** (1989) 1178.
8. H. Tarui, Y. Kishi, N. Nakamura, M. Nishikuni, M. Tanaka, H. Haku, T. Takahama and S. Tsuda: Sol. Energy. Mater. **23** (1991) 227.
9. R. A. Street and D. K. Biegelsen: Solid State Commun. **44** (1982) 501.
10. S. Tsuda, N. Nakamura, K. Watanabe, T. Takahama, M. Nishikuni, M. Ohnishi, and Y. Kuwano: Sol. Cell **9** (1983) 25.
11. Y. Uchida, M. Nishiura, H. Sakai and H. Haruki: Sol. Cell **9** (1983) 3.
12. S. Tsuda, T. Takahama, M. Isomura, H. Tarui, Y. Nakashima, Y. Hishikawa, N. Nakamura, T. Matsuoka, H. Nishiwaki, S. Nakano, M. Ohnishi and Y. Kuwano: Jpn. J. Appl. Phys. **26** (1987) 33.
13. H. Pfleiderer, W. Kusian, E. Gunzel and J. Grabmaier: *Proc. 20th IEEE Photovoltaic Specialists Conf.*, Las Vegas, Nevada, USA (IEEE, New York, NY, 1988) p.180.
14. M. Gorn, N. Kniffler and G. Winterling: *Proc. 7th EC Photovoltaic Solar Energy Conf.*, Sevilla, Spain (WIP, Munchen, Germany, 1986) p.412.
15. J. K. Arch, F. A. Rubinelli, J. Y. Hou and S. J. Fonash: *Proc. 21th IEEE Photovoltaic Specialists Conf.*., Kissimmee, Florida, USA (IEEE, New York, NY, 1990) p.1636.

16. R. A. Street, D.K. Biegelsen, W. B. Jackson, N. M. Johnson and M. Stutzmann: Philos. Mag. B **52** (1985) 235.

17. 15. W.B. Jackson, N.M. Amer, A.V. Boccara and D. Fournier: Appl. Opt. **38** (1981) 1333.

18. R. A. Street: J. Non-Cryst. Solid **77&78** (1985) 1.

19. M. Stutzmann, D.K. Biegelsen and R. A. Street: Phys. Rev. B **35** (1987) 5666.

4. Consideration of the defect formation process

4.1 Background and motivation

The characteristics of light-induced defects and their influence on device operation were discussed, and various aspects of their behavior were identified in Chapters 2 and 3. However, questions about the light-induced defects still remain: the mechanism of the saturated light-induced defects, the role of hydrogen, the driving force for defect creation, the defect removal mechanism, and so on. To answer these questions, it is necessary to take more precise and systematic data, not only about static behavior but also about the kinetics of defect creation and removal. Four processes are thought to exist in defect kinetics, as shown in Fig. 4-1 [1]: light-induced creation, C_1; light-induced annealing, A_1; thermal creation, C_2; and thermal annealing, A_2. The C_1 and A_2 processes are the main features of the S-W effect and are often observed. It is widely recognized that the C_1 process corresponds to G^2 (square of the photoinduced carrier generation rate) [2] and that the A_2 process has a thermal activation energy of about 1 eV [2]. The C_2 process can be seen when samples heated at relatively high temperature (>200°C) are rapidly cooled down. The defects thermally created in the C_2 process are frozen due to the rapid cooling rate [3]. But the C_2 process is not observed in the temperature range (<100°C) in which light-soaking generally proceeds. The A_1 process has not been identified although its existence has been suspected. For these four processes, the defect creation and removal rate is roughly expressed by Eq. 4-1.

$$dN_D/dt=C_1(N_A,G)+C_2(N_A,T)-A_1(N_D,G)-A_2(N_D,T). \qquad (4\text{-}1)$$

Here, N_D, N_A, G and T are the densities of the defect states (metastable defects), the annealed states (non-defect sites which can be converted to defects), the photoinduced carrier generation rate and temperature, respectively. The C_2 and A_2 processes are relatively simple because only thermal energy is counted to understand the mechanisms. The effects of light and thermal energy, however, always exist at same time in the C_1 and A_1 processes, and these processes are

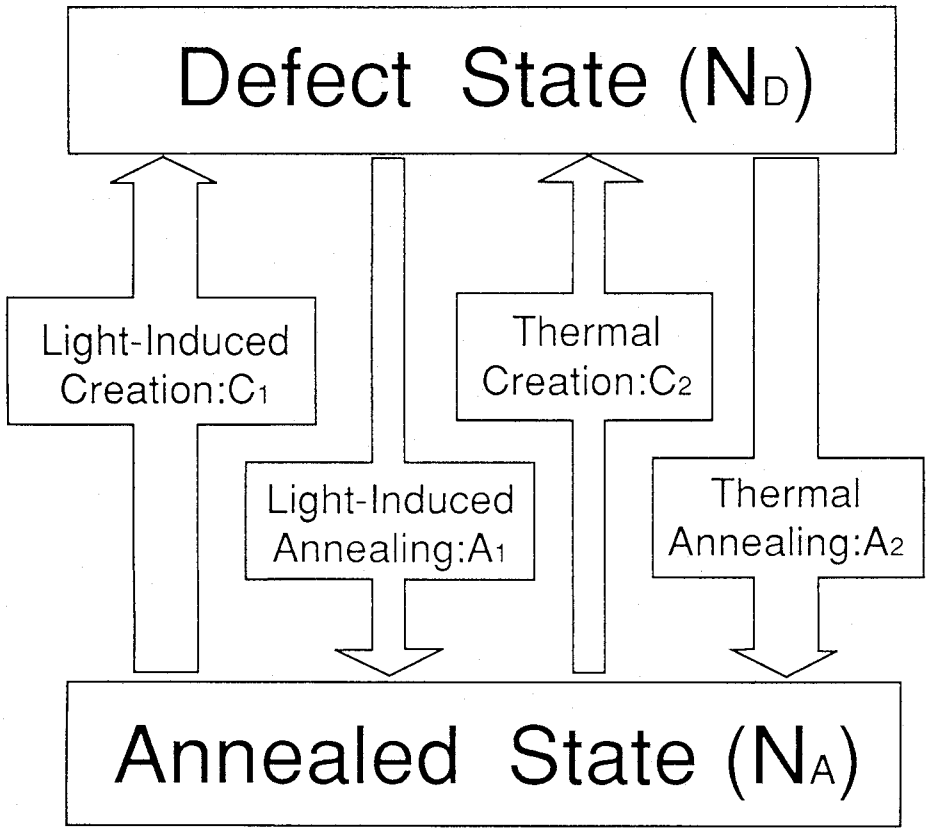

Fig. 4-1 Processes of defects creation and removal in metastable change in a-Si:H.

more difficult to understand. Besides, interdependence between the light and thermal effects may cause more difficulties.

Section 4.2 focuses on the C_1 and A_1 processes to investigate the effects of light on the creation and removal of defects, and the correlation with thermal effects. Section 4.3 presents a microscopic view of the network structure of a-Si:H with respect to the light-induced defects as considered from the overall results.

4.2 Kinetics in the creation and removal of light-induced defects

4.2.1 Effect of temperature on defect creation

The temperature dependence of the light-induced defect creation rate has been often observed [2]. The light-induced defect creation process, C_1, may have another parameter of T. In order to solve this question, the effects of temperature on defect creation is studied by measuring the photoconductivity σ_{ph} in Fig. 4-2 and the defect density Ns in Fig. 4-3. Figure 4-2 shows the effect of sample temperature on normalized photoconductivity, $\sigma_{ph}/\sigma_{ph}(0)$, as a function of illumination time under high-intensity (HI: 647 nm; 3 Wcm^{-2}, $G=3x10^{22}$ $cm^{-3}s^{-1}$) and low-intensity (LI: 650nm; 0.005 Wcm^{-2}, $G=5x10^{19}$ $cm^{-3}s^{-1}$) light-soaking. As usually observed, σ_{ph} decreases much faster at HI than LI. Attention should be drawn to the difference in temperature dependence between the HI and LI conditions. The spread in σ_{ph} caused by a comparable variation in temperature is much higher at high intensity than at low intensity. The defect densities under the HI condition are also plotted in Fig. 4-3 together with low-intensity data (λ=651, Intensity=0.2Wcm^{-2}) published earlier [2]. Again, the growth rate of the defect density is affected by temperature more strongly under high-intensity than under low-intensity light-soaking. The evidence from Figs. 4-2 and 4-3 is that the rate of growth of the defect density is more sensitive to temperature under high-intensity than under low-intensity light.

These experimental data show that the defect creation mechanism changes with the intensity of light-soaking. The temperature dependence of the creation associated with this thermal activation becomes more pronounced with increasing light intensity. The primary processes for defect generation are most likely carrier-driven. This finding suggests that these primary processes are coupled with other processes that are thermally activated. These thermally

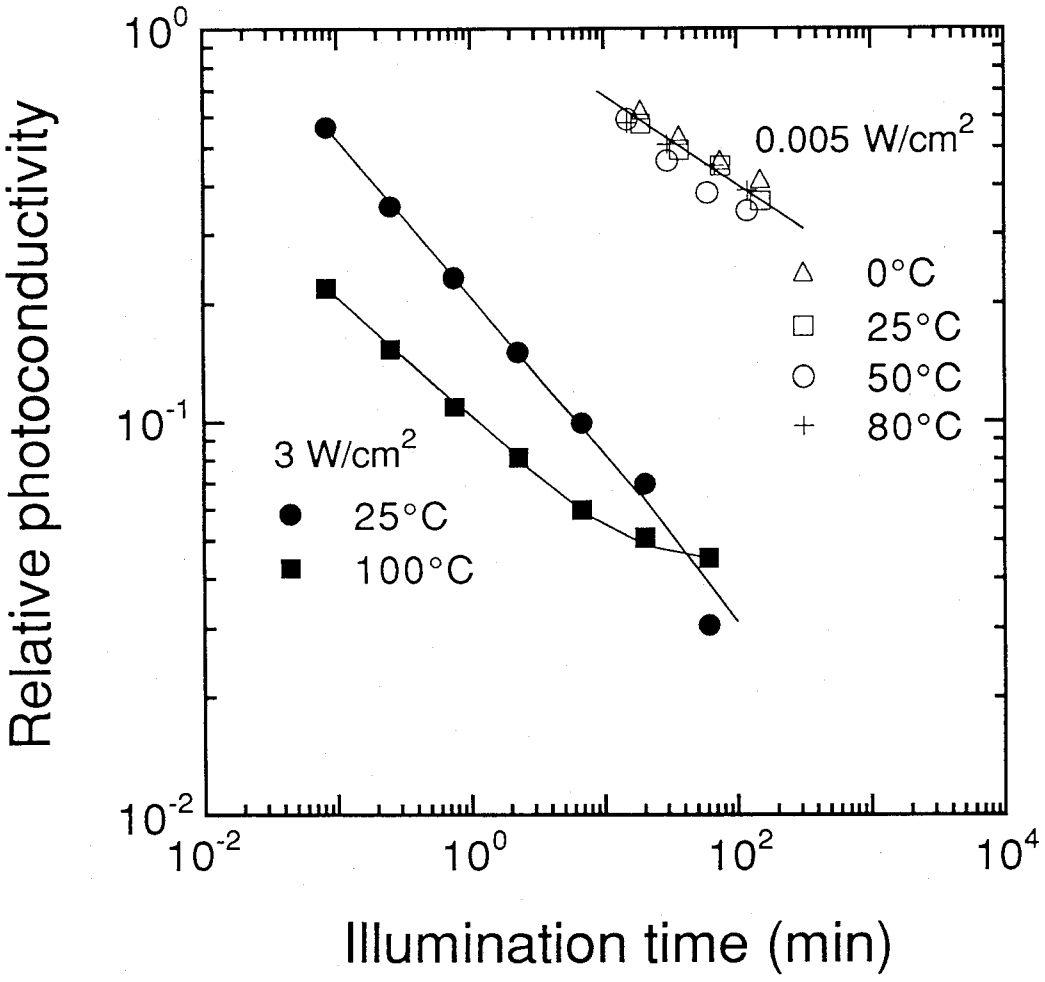

Fig. 4-2 Photoconductivity as a function of light-soaking time for a range of temperatures and two light intensities.

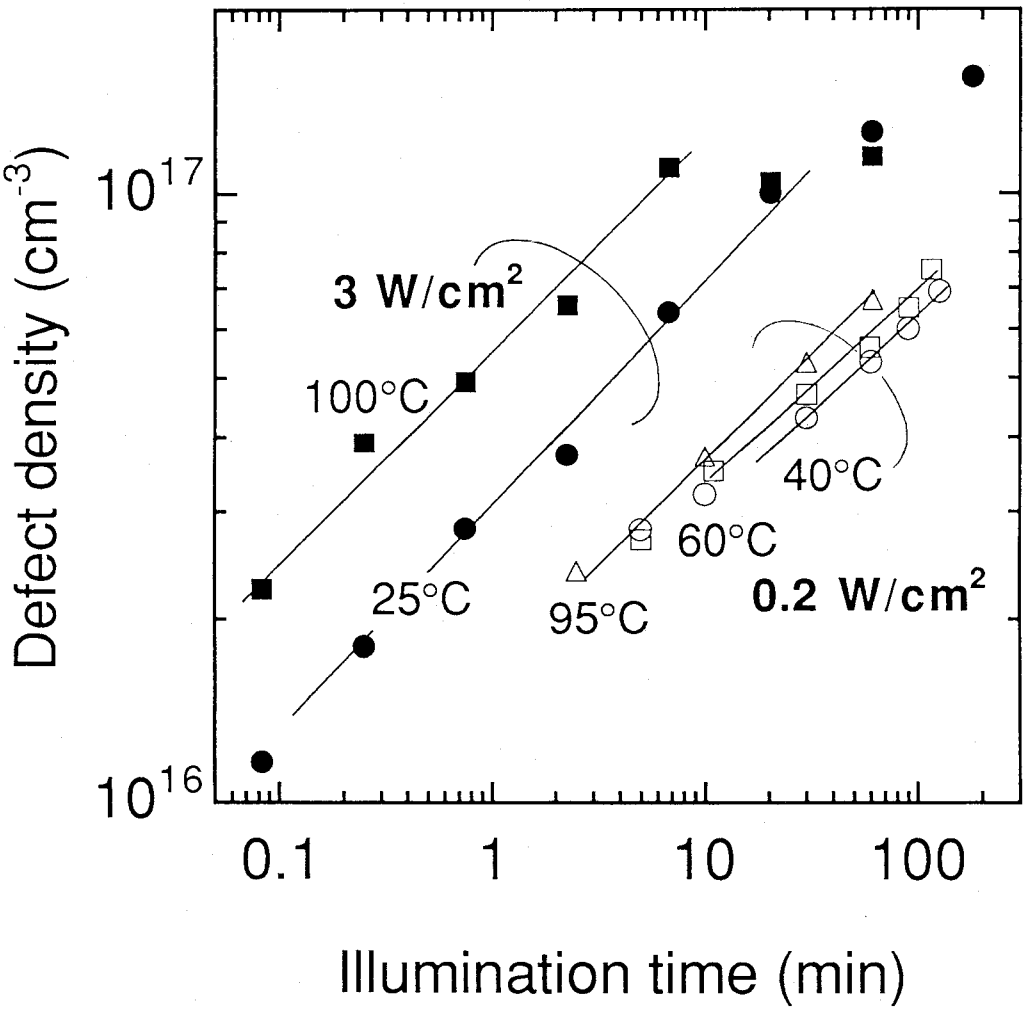

Fig. 4-3 The defect density as a function of light-soaking time for a range of temperatures and two light intensities.

activated steps control the overall rates of the creation more strongly when the primary processes are fast (at high carrier generation). One possible mechanism which fits the finding is an electron and hole process, for example the localization of an electron and a hole on the Si-Si bond, coupled with hydrogen motion. To pursue this consideration, the data in Figs. 4-2 and 4-3 are fitted with Eq. 2-4 of the recombination model [2] and a C_{sw} constant is calculated for each data. In this model, the band-to-band carrier recombination is assumed to be the driving force for the defect creation and the C_{sw} constant consequently contains the temperature effect. In the calculations, σ_{ph} is assumed to correspond to reciprocal defect density, $1/N_S$ [2]. The calculated C_{sw} are plotted as a function of reciprocal temperature in Fig. 4-4. Here, it can be seen more clearly that the light intensity enhances the temperature dependence. Activation energies of C_{sw} obtained from these Arrhenius plots are shown as a function of the light intensity in Fig. 4-5. The activation energy increases from 0.05 to 0.3 eV with increased light intensity from 0.005 to 3 Wcm^{-2}. W.B. Jackson calculated the light-induced defect creation based on dispersive hydrogen diffusion [4]. The large temperature dependence of the defect creation rate in his calculation results is similar to the temperature dependence observed under the HI condition, so the assumption of the carrier-driven process coupled with hydrogen motion is likely supported. Further details are discussed in a later section.

4.2.2 Light-induced annealing

The light-induced annealing process, A_1, is sometimes discussed, but the appearance of this phenomenon is still unknown. Measurements of the defect annealing rate under illumination were conducted to identify this process. The samples used in these experiments had initial (annealed state) defect densities of $3\text{-}5x10^{15}$ cm^{-3}. Their defect densities were first saturated around 50°C at a high-intensity condition (645 nm; 3 Wcm^{-2}, $G=3x10^{22}$ $cm^{-3}s^{-1}$). Then the samples were annealed at 130°C in the dark and at three light intensities between 0.005 and 0.5 Wcm^{-2} (estimated generation rates of $5x10^{19}$ $cm^{-3}s^{-1}$ to $5x10^{21}$ $cm^{-3}s^{-1}$). As shown in Fig. 4-6, the annealing proceeds much faster at high intensity than at low intensity and it is the slowest in the dark. Note that after 1 minute at 0.5 Wcm^{-2} the defect density already has reached its steady-state value. At 0.05 Wcm^{-2} illumination the defect density reaches its steady-state value after 15

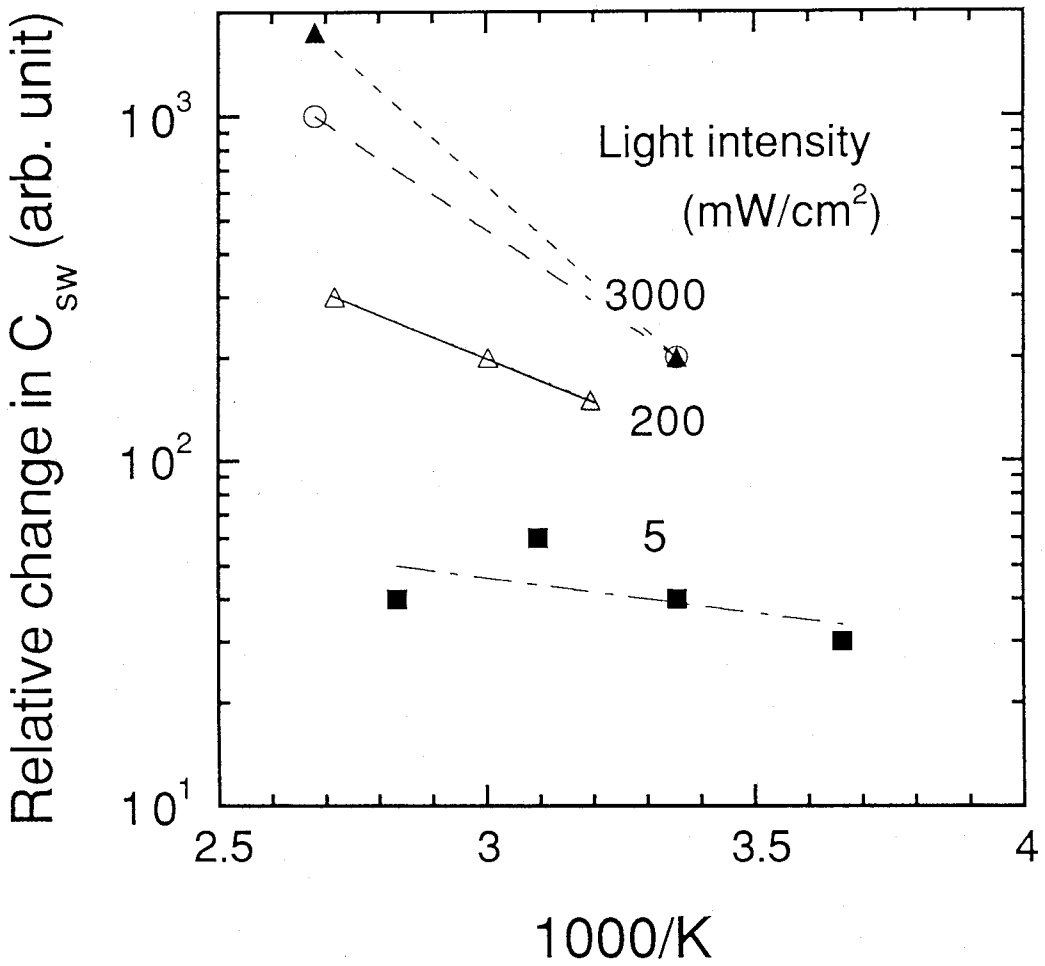

Fig. 4-4 Relative change in C_{sw} constant under several light intensities as a function of reciprocal temperature. Closed symbols are data from the photoconductivity measurements.

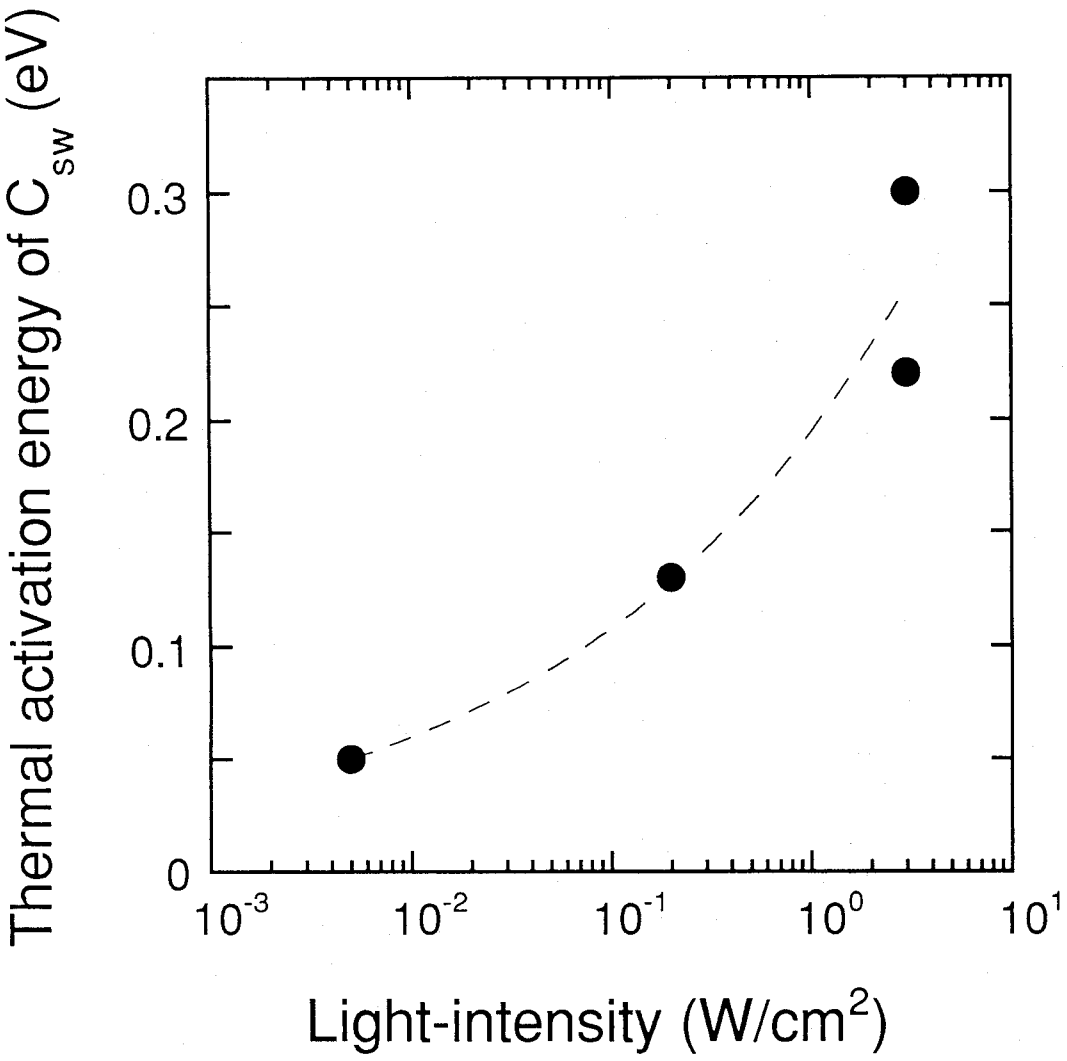

Fig. 4-5 Thermal activation energy of C_{sw} constant as a function of light intensity.

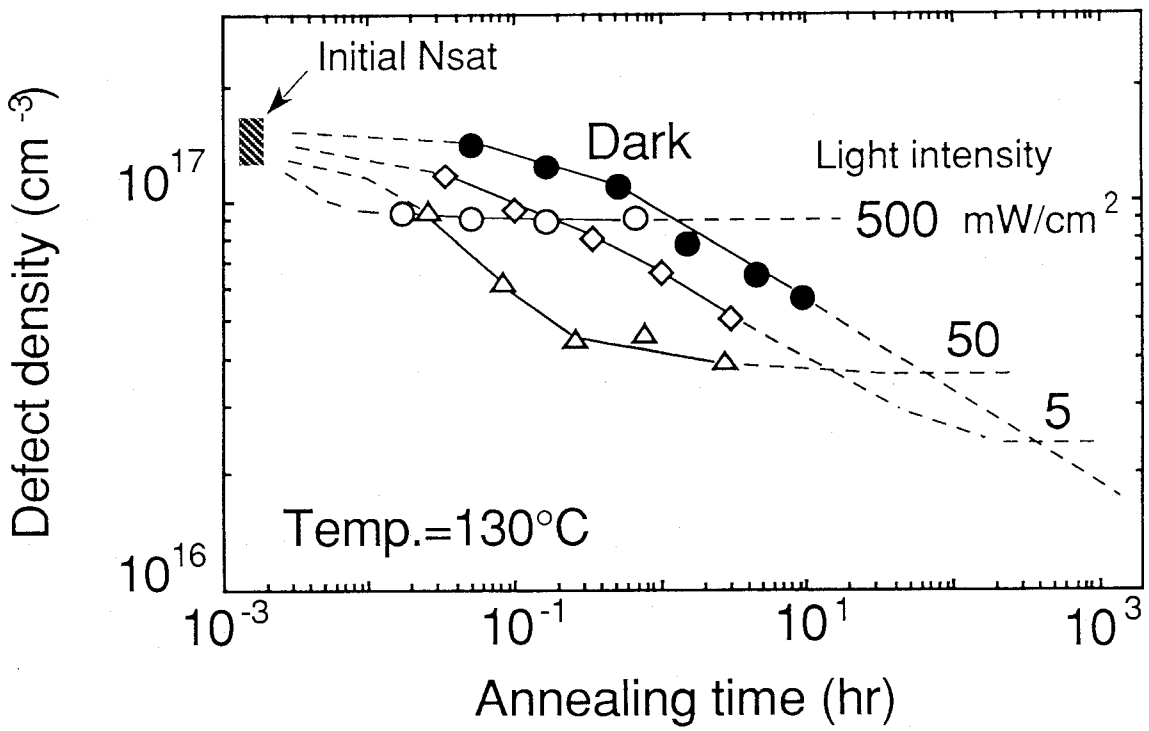

Fig. 4-6 Light-induced annealing of the defect density and annealing in the dark.

minutes of illumination. The defect density would probably reach its steady-state after a longer time at 0.005 Wcm^{-2}. These results mean that the rate of defect annealing is enhanced by illumination and that it rises with intensity.

The annealing is thought to be related to hydrogen motion [5,6]. Since the rate of hydrogen diffusion in a-Si:H depends on the position of the Fermi level [7,8], it will depend on the light intensity. Indeed, Santos et al. [9] detected by secondary ion mass spectroscopy (SIMS) that H-diffusion is accelerated by illumination. Therefore, the enhanced hydrogen diffusion under illumination may explain the intensity dependence of the annealing rate. To gain further understanding, the data fitting was conducted with the stretched-exponential relaxation modelled by Kakalios et al. [5]. The decay of the defect density Ns is described by

$$Ns=(N_{sat}-N_O)\exp[-(t/\tau)^{\beta}]+N_O, \qquad (4\text{-}2)$$

where N_{sat} and N_O are the saturated and annealed defect densities, respectively, and t, τ and β are time, characteristic time and dispersion parameter, respectively. The results of the fitting are shown in Fig. 4-7. In these calculations a β value of 0.35 was taken and τ values of 0.15, 1.8 and 8.0 for 0.05, 0.005 and 0 Wcm^{-2}, respectively. The defect creation rate, dN_S/dt, is assumed to correlate with the hydrogen diffusion coefficient, D_H, as Eq. 4-3 describes.

$$dN_S / dt \propto - D_H / a^2 \cdot N_S. \qquad (4\text{-}3)$$

Then, the value of τ reflects the diffusion coefficient of hydrogen as expressed by Eq. 4-4.

$$D_H \propto (1/\tau)^{\beta}. \qquad (4\text{-}4)$$

Thus, the relative value of D_H can be obtained from Eq. 4-4. The relative D_H normalized by D_H in the dark are plotted as a function of light intensity together with the data on the light-enhanced hydrogen diffusion in Fig. 4-8. Both data show a similar tendency and suggest that light-

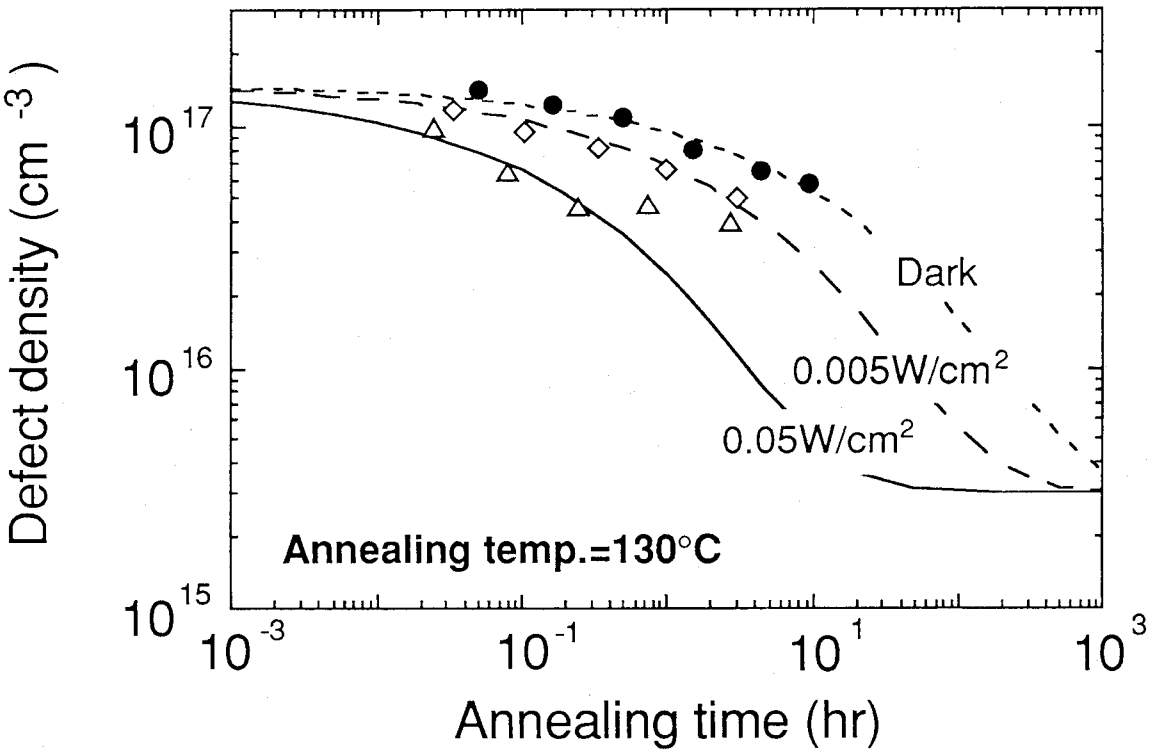

Fig. 4-7 Fit of the light-induced annealing data to a stretched exponential relaxation.

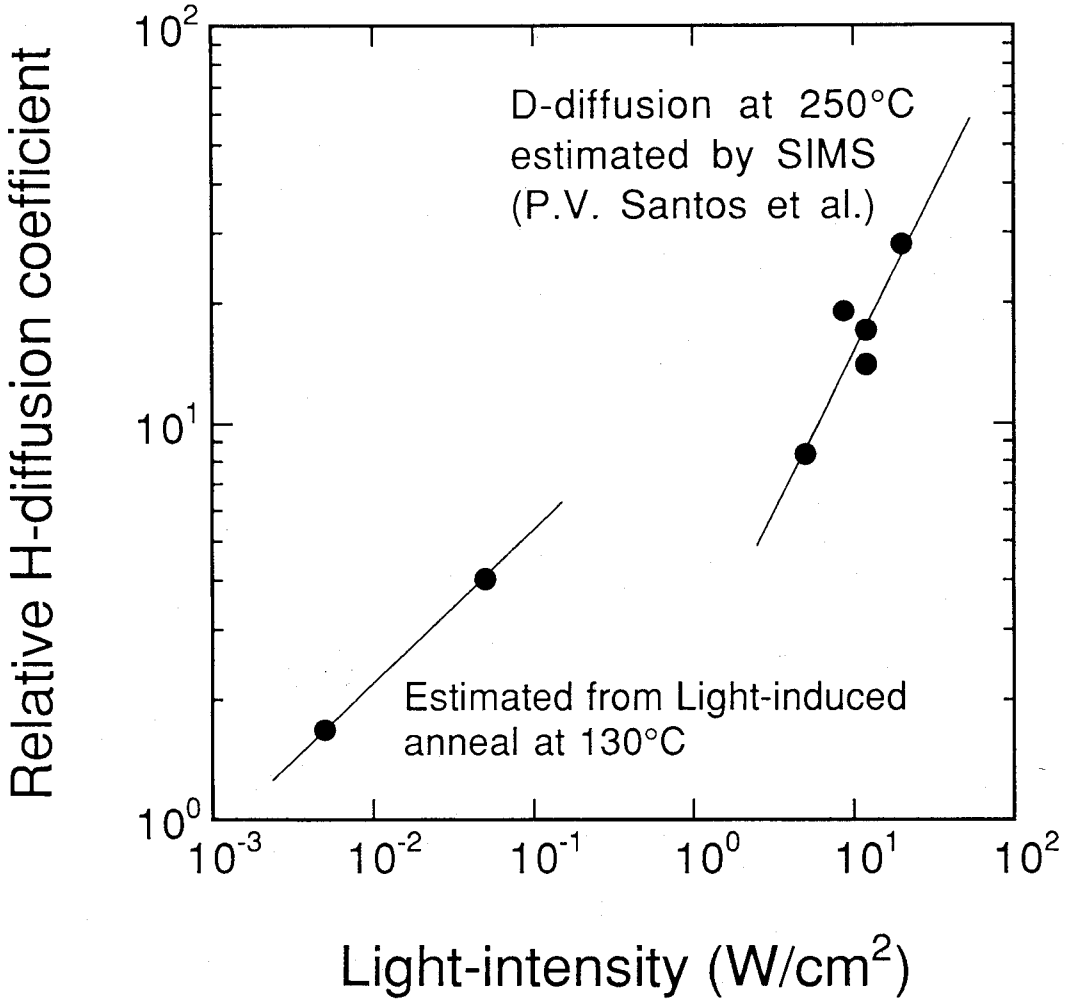

Fig. 4-8 Hydrogen diffusion coefficient extracted from the data on light-induced annealing, and from SIMS measurement.

enhanced hydrogen diffusion accelerates the annealing rate of light-induced defects. It is suggested again here that the hydrogen motion has an important role in removing the defects.

4.3 Microscopic view of the defect configuration

4.3.1 Effect of SiH_2 bonds on metastability

Several aspects were observed to show the relation between metastability and hydrogen in a-Si:H. In Chapter 2, the saturation value of the light-induced defects was found to correlate with the hydrogen content. The evidence given in this chapter shows that hydrogen motion affects the kinetics in the creation and removal of the defects. These results strongly suggest that hydrogen has an important role in the metastability of a-Si:H. However, a-Si:H films usually have the hydrogen concentration of 10^{21}-10^{22} cm^{-3}, which are much more than the saturated defect density of ~10^{17} cm^{-3}. Therefore, it is difficult to think that all the hydrogen atoms take part in the metastability, and some discrimination among the incorporated hydrogens is needed to explain the metastable effects.

Here, SiH_2 bonds detected by infrared absorption [10] are focused on for a more precise consideration. The SiH_2 and SiH bond densities of a-Si:H samples are plotted as a function of hydrogen content in Fig. 4-9. The SiH_2 bond density is seen to increase very rapidly with increased hydrogen content, though SiH bond density does not change so much. Therefore, the effects of the hydrogen content can be thought to go hand in hand with SiH_2 bond density. Besides, the SiH_2 configuration has two-fold coordination, so structural flexibility can be expected compared with a three-fold SiH configuration or four-fold ordinary silicons. Indeed, an irreversible effect is observed probably due to the flexibility of the SiH_2 bonds. Figure 4-10 shows the procedure of the light-soaking / thermal annealing repetition test and its result for samples with several SiH_2 bond densities. In this test, a set of light-soaking of 500 mW/cm^2 for 5 hours and thermal annealing at 180°C for 1 hour was repeated several times, and after each light-soaking, the dangling bond density was measured with the electron spin resonance (ESR) as shown by the flow chart of Fig. 4-10 (a). For the light-soaking a tungsten lamp was used with an infrared cut filter. Normalized spin density after each light-soaking is plotted as a function of repetition number in Fig. 4-10 (b). In the sample with SiH_2 bond density of 2.3%,

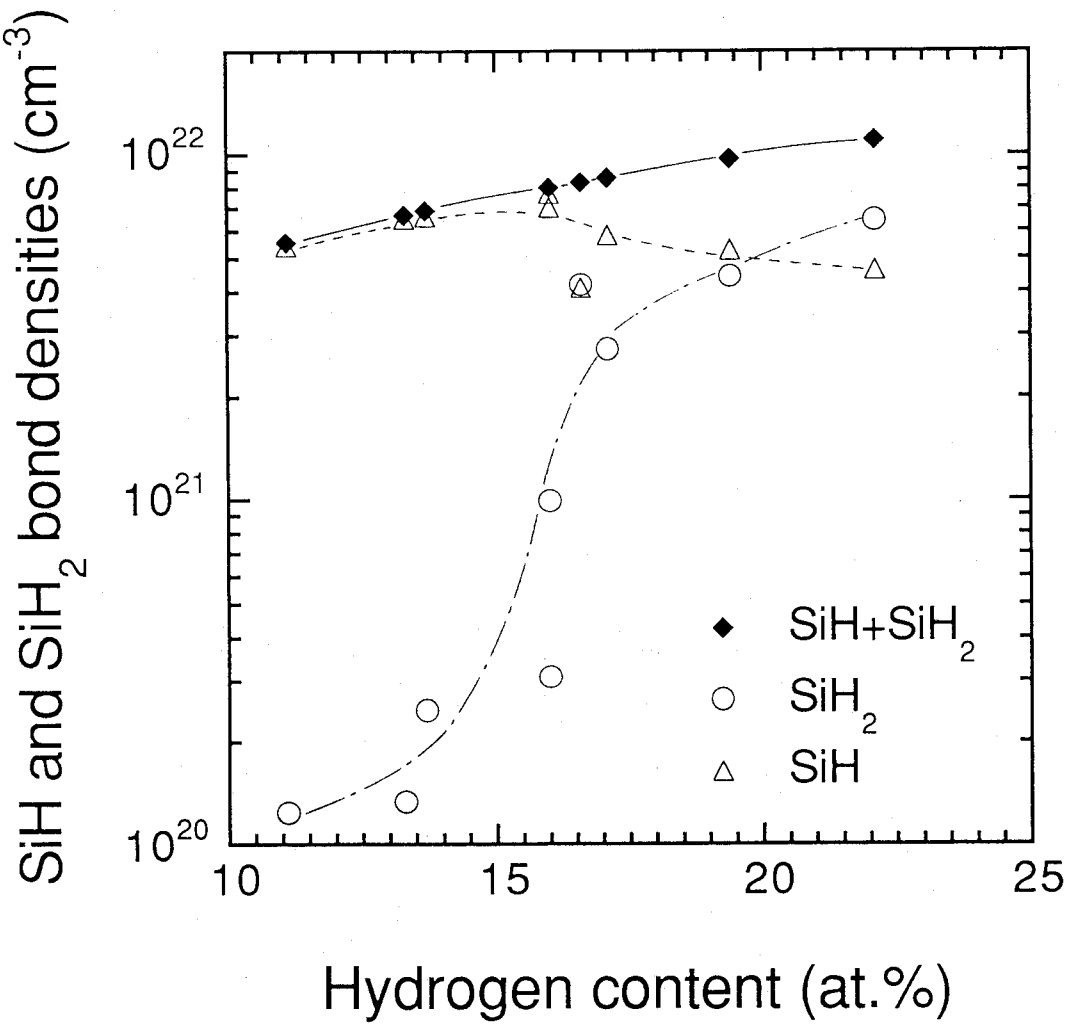

Fig. 4-9 SiH_2 and SiH bond densities estimated by infrared absorption as a function of hydrogen content in a-Si:H.

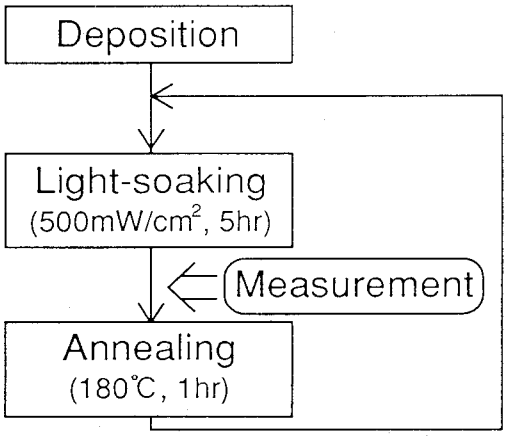

(a)

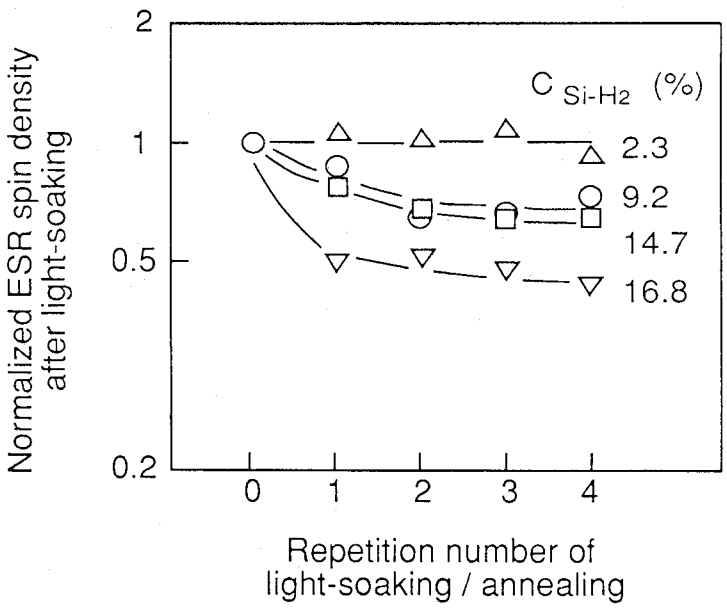

(b)

Fig. 4-10 (a) Procedure of the light-soaking / thermal annealing repetition test. (b) ESR spin densities of a-Si:H samples with several SiH_2 bond densities after light-soaking in each repetition as a function of repetition number.

the normalized spin density does not change due to the repetition. Its metastability is completely reversible. However, an irreversible change appears with increasing SiH_2 bond density. The normalized spin density is decreased by the repetition, and this trend is more pronounced in the sample with higher SiH_2 bond density. After four repetitions, the sample with SiH_2 bond density of 16.8% shows a half value of the spin density after the first light-soaking. This irreversible change can be explained by the flexibility of the SiH_2 bond. Amorphous networks always require more relaxation, so the two-fold SiH_2 configuration gives a more stable condition due to its structural flexibility while the hydrogen motion related to the metastable change occurs.

4.3.2 Model in the microscopic structure

Figure 4-11 (a) shows the microscopic structure model of metastable change in a-Si:H proposed by K. Morigaki [11]. Hydrogen has high electronegativity compared with silicon, so a Si-Si bond next to a SiH configuration is weakened due to the less probability of electron existence in the Si-Si bond. Such Si-Si bonds can be relatively easily broken by receiving extra energy, such as in carrier trapping, recombination and so on. After the bond is broken, one of the two dangling bonds is stabilized by placing a hydrogen atom on the other dangling bond, and then, the hydrogen atom moves to a stable position. Thus, two dangling bonds are consequently created as shown in Fig. 4-11 (a). Here, the SiH_2 configuration is newly taken into account in a model based on the sense of the Morigaki model, because Fig. 4-9 clearly shows that the change in hydrogen content goes hand in hand with SiH_2 bond density. The explanation for the phenomena observed in this thesis is thus conducted with a new SiH_2 model. The SiH_2 model is illustrated in Fig. 4-11 (b). A Si-Si bond next to a SiH_2 configuration can be thought to be weaker than one next to a SiH configuration, and the hydrogen placing on the broken bond likely occurs more frequently, due to the two hydrogen atoms. Moreover, the structural flexibility of the SiH_2 configuration helps the dangling bonds to be stabilized as illustrated in the righthand picture of Fig. 4-11 (b).

The SiH_2 bond density of 10^{20}-10^{22} cm^{-3} is still much larger than the saturated defect density of about 10^{17} cm^{-3}. Probably, the condition of the SiH_2 configurations is energetically

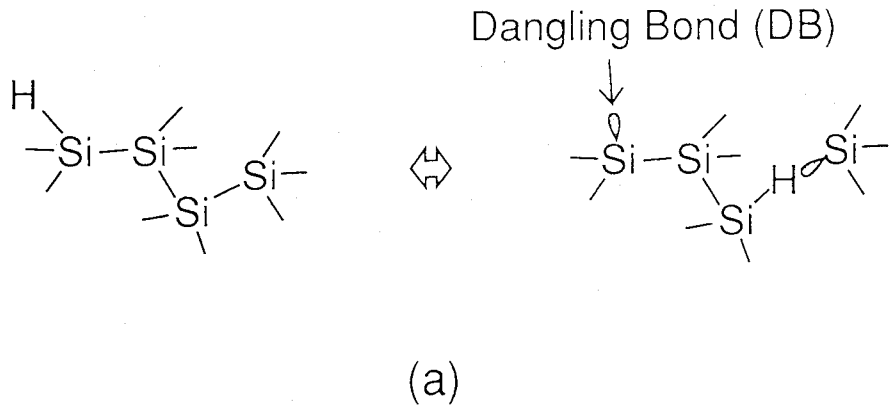

(a)

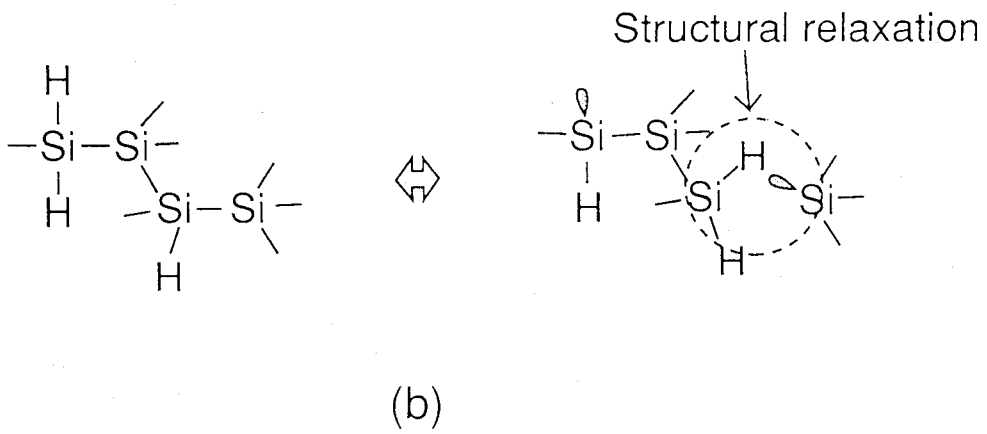

(b)

Fig. 4-11 Silicon network models in a-Si:H with respect to metastable change: (a) Morigaki model and (b) SiH_2 model.

distributed and not all of them contribute the bond breaking. Also, the structural circumstances are not always suited to defect stabilization. When both the energetic and structural conditions are suitable, defect creation can be completed. The temperature dependence of the defect creation can also be explained by the carrier-driven process coupled with hydrogen motion as mentioned above. In the present model, the carrier-driven process means the bond-breaking due to the trapping or recombination of the photoinduced carriers, and then the hydrogen motion around the SiH_2 configuration follows the bond-breaking for stabilizing the defects. Under high-intensity light-soaking the carrier-driven process is very fast. In other words, a large number of bond-breaking occur. Therefore, the following hydrogen motion is not fast enough compared with the carrier-driven process, and consequently limits the overall process. Because the hydrogen motion is activated by thermal energy, the temperature dependence of the defect creation rate appears under high-intensity light-soaking. The carrier-driven process, however, determines the rate of defect creation under low-intensity light-soaking because the hydrogen motion is fast enough to follow the carrier-driven process. Hence, the temperature dependence does not appear. In the defect removal (annealing) process, the hydrogen motion also has an important role. The dangling bonds are returned to Si-Si bonds by connecting other dangling bonds after removing hydrogen atoms from Si-H bonds nearby. This reaction is faster when the hydrogen motion is enhanced by thermal energy or light-soaking. Thus, the thermal and light-induced annealing can be explained.

4.4 Summary

The light-induced defect creation and annealing processes are focused on in order to investigate the effects of light on the creation and removal of the metastable defects. The experimental evidence shows that the rates of defect creation are more sensitive to temperature when the light intensity is higher. This increased sensitivity to temperature at high rates suggests that a temperature-activated process such as hydrogen motion controls the rates of creation more when they are high, and that the rate-limiting process changes with the intensity of soaking light. The rate of annealing under illumination at 130°C is strongly accelerated by illumination, and depends strongly on the light intensity. The hydrogen diffusion coefficient estimated from

the rate of annealing under illumination shows a trend similar to light-enhanced hydrogen diffusion as a function of light intensity. Therefore, this behavior of light-induced annealing can be explained by the diffusion of hydrogen, accelerated by excess carriers.

The SiH_2 bond density increases very rapidly with the increased hydrogen content, though the SiH bond density does not change so much. Therefore, the effects of the hydrogen content can be thought to go hand in hand with SiH_2 bond density. Besides, the SiH_2 configuration produces an irreversible effect as observed by ESR measurement. The defect density after light-soaking decreases by the light-soaking / thermal annealing repetition, due to the flexibility of the two-fold coordination. The SiH_2 configuration is newly taken into account in a model based on the hyrogen-motion model [11]. In the new model, the bond-breaking process followed by the hydrogen moton is assumed and the hydrogen motion accompanied by the structural relaxation with the two-fold SiH_2 configuration stabilizes the dangling bond states. The explanation for the phenomena observed in this thesis can be carried out with the new model.

References

1. D. Redfield: Appl. Phys. Lett. **52** (1988) 492.
2. M.Stutzmann, W.B.Jackson and C.C.Tsai, Phys. Rev. B **32**, 23 (1985).
3. Z E, Smith and S. Wagner: Phys. Rev. B **32** (1985) 5510.
4. W.B. Jackson, Phil. Mag. Lett. **59** (1989) 108.
5. J. Kakalios, R.A. Street and W.B. Jackson, Phys. Rev. Lett. **59** (1987) 1037.
6. W.B. Jackson and J. Kakalios, Phys. Rev. B **37** (1988) 1020.
7. R.A. Street, C.C. Tsai, J. Kakalios and W.B. Jackson, Phil. Mag. B **56** (1987) 305.
8. W. Beyer, J. Herion and H. Wagner, *Tech. Dig. 4th International PVSEC*, Sydney, Australia (1989) p.255.
9. P.V. Santos, C. Doland, N.M. Johnson and R.A. Street, Proc. J. Non-Cryst. Solids **137&138** (1991) 33.
10. M. Brodsky, M. Cardona and J. Cuomo: Phys. Rev. B **16** (1977) 3556.
11. K. Morigaki: Jpn. J. Appl. Phys. **27** (1988) L138.

5. Conclusions

In this thesis, a solution to light-induced degradation is sought by investigating light-induced degradation from the viewpoint of its effects on materials, and by considering the relation between material effects and device degradation. In Chapters 2 and 3, the light-induced effects of the intrinsic layer and the window p-layer are studied, respectively, and in Chapter 4 more details on the kinetics of the light-induced defects and the change in the microscopic structure are discussed. The results are summarized in the following.

Chapter 2 (the intrinsic layer)

(1) The light-induced defect density in a-Si:H can be brought to saturation with only a few hours of intense illumination. The saturation value is correlated with the growth rate of the defect density. This correlation permits a reconstruction of the entire defect history of a sample of a-Si:H from its saturation value. Therefore, it is a robust criterion for predicting the "usable life" of a-Si:H materials and of solar cells.

(2) The temperature and light-intensity dependences of the saturated light-induced defect density N_{sat} can be explained within the defect pool model by the limited number of defect sites in the tail states coupled with the concept of defect equilibrium. The results of the calculations suggest that an assumption in which the convertible defect sites are limited is reasonable.

(3) Experimental data of N_{sat} versus Urbach energy E_u and hydrogen content c_H show that the tail states do not directly affect N_{sat} in device-quality a-Si:H and that c_H is more important for limiting the number of defects than the tail states.

Chapter 3 (the window p-layer)

(4) The experimental data of V_{oc} show that a high-doped p-layer results in a higher built-in potential but the high defect density induced by the doping imposes a limitation on V_{oc}, and that a low-doped p-layer results in a lower built-in potential but a higher V_{oc} can be obtained

because of its low defect density. The defect density of the p-layer near the p/i interface causes the V_{oc} limitation, and it is necessary to attain both high built-in potential and low defect density near the p/i interface in order to obtain a higher V_{oc}.

(5) Light-induced degradation of V_{oc} occurs to a much greater extent in low-doped p-layer cells than in high-doped p-layer cells because the light-induced defect density in the low-doped p-layer is not negligible compared with the initial defect density. The high-doped p-layer initially has a relatively high defect density and acceptor concentration; thus, the light-induced defects do not affect the properties of the p-layer as much and little degradation of V_{oc} occurs.

Chapter 4 (consideration of the defect formation)

(6) The rates in the light-induced defect creation are more sensitive to temperature when the light intensity is higher. This increased sensitivity to temperature at high rates suggests that a temperature-activated process controls the rates of creation more when they are high. This can be explained by the carrier-driven process coupled with hydrogen motion.

(7) The rate of annealing under illumination at 130°C is strongly accelerated by illumination, and depends strongly on the light intensity. The hydrogen diffusion estimated from the rate of annealing under illumination is similar to the light-enhanced hydrogen diffusion. Therefore, this behavior of light-induced annealing can be explained by the diffusion of hydrogen, accelerated by excess carriers.

(8) The SiH_2 bond density increases very rapidly with increased hydrogen content, though the SiH bond density does not change so much. Therefore, the effects of the hydrogen content can be thought to go hand in hand with SiH_2 bond density. Besides, the SiH_2 configuration produces an irreversible effect, due to the flexibility of its two-fold coordination.

(9) The SiH_2 configuration is newly taken into account in a model based on the hydrogen-motion model. A bond-breaking process followed by hydrogen motion is assumed. The hydrogen motion is accompanied by structural relaxation, which stabilizes the dangling bond states, due

to the two-fold SiH_2 configuration. The explanation for the phenomena observed in this thesis can be carried out with the new model.

Acknowledgment

The author wishes to express his gratitude to Professor Takeshi Kobayashi of the Faculty of Engineering Science of Osaka University for his kind guidance and helpful suggestions for completing this thesis.

The author is also grateful to Professor Yoshihiro Hamakawa, Professor Kenji Gamo, and Associate Professor Hiroaki Okamoto of the Faculty of Engineering Science of Osaka University for their guidance and suggestions during the prepararion of this thesis.

Part of this work was carried out at the Department of Electrical Engineering of Princeton University, and supported by the Amorphous Thin Film Solar Cell Program of the Electric Power Research Institute of the United States of America.

The other part of this work was carried out at the Functional Materials Research Center of SANYO Electric Co., Ltd., and in part supported by the New Energy and Industrial Technology Development Organization as a part of the Sunshine Project under the Ministry of International Trade and Industry.

The author would especially like to acknowledge the helpful guidance and encouragement of Professor Sigurd Wagner of Princeton University.

The author also expresses special thanks to Dr. Seiji Ohara and Dr. Yukinori Kuwano, executive directors of the R&D headquaters of SANYO Electric Co., Ltd. for their immeasurable and valuable support.

Support was also provided by Dr. Shoichi Nakano, general manager of the Functional Materials Research Center, and Dr. Shinya Tsuda, manager of the Thin Film Laboratory, for which the author wishes to express his great appreciation.

The author gratefully thanks Dr. Nobuhiro Hata and Dr. Xixiang Xu for their helpful discussions and numerical simulations.

And the author thanks Ms. Ritsuyo Ohnishi and Ms. Yuko Ohtsu for preparing some of the figures.